Dynamics of Plasma Structures Interacting with External and Self-Generated Magnetic Fields

Thesis by

Gunsu Soonshin Yun

In Partial Fulfillment of the Requirements
for the Degree of
Doctor of Philosophy

California Institute of Technology
Pasadena, California

2008
(Defended July 12, 2007)

This thesis is dedicated in loving memory to my father,
who devoted his life to family.

Acknowledgements

My first encounter with Caltech was a pleasing scent surrounding the campus in a night of March, 2002. Although it aggravated my allergy in the next few years, my memories of Caltech are filled with gratefulness as pleasant as the scent thanks to the people who have been with me.

I am deeply grateful to my advisor, Prof. Paul M. Bellan. In classroom, laboratory, and office, his thoughtful mentorship for my academic progress and genuine interest in science always encouraged me to endeavor in research. I find it still amazing and grateful at the same time that, whenever I made a mistake in experiment, Paul always encouraged me by telling a story about himself or someone else making a similar mistake. I also enjoyed his many entertaining stories during lunch.

I am indebted to two post-docs, Setthivoine You and Shreekrishna Tripathi. Their mentorship, collaboration, and numerous efforts to improve the experiment have greatly benefited this thesis work. Working with and learning from Sett were as exciting as watching the 2006 World Cup soccer games on his projection screen. We were both allergic to our office and I thank Sett for sharing his allergy pills at the time when I was afraid of my wife's acupuncture. Collaborating with Shreekrishna was always as entertaining as listening to his amazing stories about his village in the northern India. I thank Shreekrishna and his wife Rashmi for inviting our group to their home with warmth and authentic Indian foods.

I enjoyed lively companionship with my fellow graduate students including Carlos Romero-Talamás, Steven Pracko, Eli Jorne, Rory Perkins, Auna Moser, Eve Stenson, and Deepak Kumar. Carlos saved me from my first mishap in the lab by removing a broken vacuum bolt stuck in a thread using a vise-grip, which became my favorite

tool afterwards. Steve always provided me a helping hand for finding anything in the lab. Steve's humorous anecdotes about predecessors, lab equipments, and past accidents made the lab a lively workplace. Eli entertained us with his witty songs, often intended to mock one of us, and has continued to do so even after leaving Caltech to pursue his talent at the film industry. Rory entertained us in a very different way with his electric guitar and his choice heavy-metallic music. He must have found a beauty in the often disturbing music, considering his thorough understanding of physics. Auna amazed me by her agility to move around a maze of probes inside the vacuum chamber. I enjoyed playing Tak-zi with Auna although her Tak-zi skill is not as good as her agility in the chamber. Eve invigorated our workplace with her plants and her acrobatic stunt in the hallway. I thank Eve for tolerating my golf swing practice in the office. Deepak collaborated with me in numerous experiments and inspired me to enjoy the life at Caltech beyond academia. Deepak almost transformed me into an Indian who loves Bollywood more than Hollywood.

I owe my safety to Mr. Dave Felt in the machine room since he taught me to use machine tools properly. Dave single-handedly built numerous gadgets for the experiment and fixed the power supplies we often blew up. I thank Mses. Connie Rodriguez, Eleonora Vorobieff, Irene Loera, Mary Metz, and Cierina Marks for helping me order lab supplies and organize paperworks. I appreciate Connie's enthusiasm evidenced by her omnipresence in the Watson building.

I am deeply indebted to Dr. Seung-soon Jang for his brotherly love and words of wisdom that strengthened my inner being and to my friends Chihoon Ahn and Byung-joon Yoon for their friendship and numerous help throughout the years. I'd also like to thank John Choi, Frederick Balagadde, and many others for their prayers during the difficult time of the loss of my father Jong-wook.

Finally, my wife Hyun-woo, my mother Ki-jeon, my sisters Young-mi and Young-sun, and my parents-in-law Pil-soo and Myung-in deserve my sincere gratitude for their tremendous support and sacrifice. I am breathing the pleasing scent again thanks to my wife's cure of my allergy and will breath the pleasing memories of Caltech throughout my entire life.

Abstract

Plasmas interacting with external and self-generated magnetic fields often develop a long tubular structure of nearly uniform cross section. Such long collimated plasma tubes have been observed in a variety of contexts ranging from astrophysical plasma jets (10^{15}–10^{22} m) to solar coronal loops (10^7–10^8 m). Remarkably, much smaller-sized plasmas (0.1–1 m) produced by the Caltech planar spheromak gun develop collimated structures bearing a striking resemblance to these natural plasma tubes. This thesis presents experimental observations of gun-produced plasma tubes that support a recently-proposed magnetohydrodynamic (MHD) pumping model as a universal collimation mechanism. For any flared flux tube carrying a finite axial current, the model predicts (i) magnetic pumping of plasma particles from a constricted region into a bulged region and (ii) tube collimation if the flow slows down at the bulged region, leading to accumulation of mass and thus concentrating the azimuthal magnetic flux frozen in the mass flow (i.e., increasing the pinch force). Time- and space-resolved spectroscopic measurements of gun-produced plasmas show (i) suprathermal Alfvénic flow (30–50 km/s), (ii) large density amplification from $\sim 10^{17}$ to $\sim 10^{22}$ m^{-3} in an Alfvénic time scale (5–10 μs), and (iii) flow slowing down and mass accumulation at the flow front, the place where the tube collimation occurs according to high-speed camera imaging. These observations are consistent with the predictions of the MHD pumping model, and thus the model offers valuable insight into the formation mechanism of laboratory, solar, and astrophysical plasma structures.

Contents

List of Figures

Chapter 1

Background

This chapter provides background information on the spheromak formation experiment and the laboratory simulation of astrophysical jets at the Caltech Bellan plasma group. In section 1, the concept of magnetic confinement of plasmas for thermonuclear fusion is introduced and the concept of spheromaks is reviewed as a natural magnetic confinement scheme. In section 2, a novel planar plasma gun used in the spheromak formation experiment is introduced. In section 3, the observation of collimated plasma structures produced by the plasma gun, which has led to the laboratory simulation of astrophysical jets, is described. In the following section, a universal MHD pumping model which explains the collimation process of plasma-filled magnetic flux tubes is summarized. In the last section, an overview of the following chapters is given.

1.1 Spheromaks

1.1.1 Magnetic confinement fusion

Nuclear fusion is the merging of two atomic nuclei to form a heavier nucleus. Sustained nuclear fusion can release a huge amount of energy as in the Sun. The fusion reaction rate f per volume is

$$f = n_1 n_2 \langle \sigma v \rangle, \tag{1.1}$$

where n_1, n_2 are the number densities of the reactant nuclei, σ is the fusion cross section, and v is the thermal velocity of the reactants. The term $\langle\sigma v\rangle$ becomes significant only at very high temperatures of 10–100 keV. Sustainable fusion reaction requires confinement of the reactant particles at these high temperatures and thus necessarily occurs in a plasma state. Furthermore, a net power production can be achieved only if the total fusion power P_{fusion} exceeds the total power loss P_{loss}, yielding the Lawson criterion:

$$P_{\text{fusion}} = fE_fV \sim n_e^2\langle\sigma v\rangle E_fV, \quad \geq \quad P_{\text{loss}} \sim E_{\text{system}}/\tau_E = Vn_ekT/\tau_E \tag{1.2}$$

$$\Longrightarrow n_e\tau_E \gtrsim \frac{kT}{\langle\sigma v\rangle E_f}, \tag{1.3}$$

where τ_E is the confinement time of the high temperature plasma, E_{system} is the total energy content of the system of volume V, E_f is the energy released by a single fusion reaction, n_e is the electron density, and kT is the average thermal energy of the particles. The critical $n_e\tau_E$ is $\sim 1.5 \times 10^{20}$ sec·m^{-3} for the deuterium–tritium reaction.

In the Sun, the gravitational force provides enough confinement time τ_E to satisfy the Lawson criterion. However, in terrestrial environment, gravitational confinement is impossible and other confinement mechanisms are required. Since plasmas are a good electrical conductor, plasmas can be confined in a magnetic field. A variety of magnetic confinement devices such as tokamaks, stellarators, and magnetic mirrors have been constructed since 1950s and much effort has been devoted to solve many engineering challenges such as construction of large magnetic coils. Relatively simple designs which require less engineering have been developed later as alternatives. Examples are reverse field pinches, field reversed configurations, and spheromaks [1]. These are collectively called compact toroids [2] because of their compact dimensions compared to tokamaks.

Spheromaks [1] are a naturally occurring plasma confinement structure such as solar prominences [3]. Spheromaks are defined as a plasma structure confined in a magnetic field configuration characterized by toroidal magnetic flux surfaces bounded by a spherical separatix surface as illustrated in figure 1.1. The bounding surface is simply connected and has no toroidal magnetic field. In contrast to tokamaks and other magnetic confinement configurations that require large external coils, spheromaks are sustained entirely by the magnetic field produced by the internal currents. In particular, the toroidal magnetic field of spheromaks necessary for particle confinement is produced by the large axial current flowing through the axis of symmetry.

1.1.2 Relaxed state of magnetized plasma

Magnetic helicity [1, chap. 3] is a most important quantity in the theory of magnetic confinement because the plasma decays into a self-organized relaxed state after undergoing complex instabilities while approximately preserving the total helicity content. The total magnetic helicity K is defined as

$$K = \int_V \boldsymbol{A} \cdot \boldsymbol{B} d^3 r, \tag{1.4}$$

where $\boldsymbol{B}$ is the magnetic field strength, $\boldsymbol{A}$ is the magnetic vector potential, and the integration is over the system volume V.

For an open system linked to the environment by two bounding surfaces, the helicity can be injected into the system by applying an electrical potential $\Delta\varphi$ across the surfaces:

$$\frac{dK}{dt} = 2\psi\Delta\varphi - 2\int_V \eta \boldsymbol{J} \cdot \boldsymbol{B} d^3 r, \tag{1.5}$$

where ψ is the magnetic flux intercepting the surfaces, η is the electrical resistivity of the plasma, and J is the current density. The term $2\psi\Delta\varphi$ describes the rate of helicity injection and the volume integral describes the resistive decay of helicity.

The resistive helicity decay rate is small compared to the magnetic energy decay rate [1, chap. 4]. Thus, the system will evolve into a minimum energy state while preserving the injected helicity. Using the method of Lagrange multipliers, the minimum energy state is obtained by minimizing $W - \lambda K$, where $W = \int d^3 r B^2 / 2\mu_0$ is the magnetic energy and λ is the Lagrange multiplier [1, chap. 4]:

$$\begin{aligned}0 = \delta W - \lambda \delta K &= \int d^3r \boldsymbol{B} \cdot \delta \boldsymbol{B} - \lambda \int d^3r (\boldsymbol{A} \cdot \delta \boldsymbol{B} + \boldsymbol{B} \cdot \delta \boldsymbol{A}) \\ &= \int d^3r \boldsymbol{B} \cdot \nabla \times \delta \boldsymbol{A} - \lambda \int d^3r (\boldsymbol{A} \cdot \nabla \times \delta \boldsymbol{A} + \boldsymbol{B} \cdot \delta \boldsymbol{A}). \end{aligned} \tag{1.6}$$

Using the vector identities

$$\begin{aligned}&\boldsymbol{B} \cdot \nabla \times \delta \boldsymbol{A} = \nabla \cdot (\delta \boldsymbol{A} \times \boldsymbol{B}) + \delta \boldsymbol{A} \cdot \nabla \times \boldsymbol{B}, \\ &\boldsymbol{A} \cdot \nabla \times \delta \boldsymbol{A} = \nabla \cdot (\delta \boldsymbol{A} \times \boldsymbol{A}) + \delta \boldsymbol{A} \cdot \nabla \times \boldsymbol{A} = \nabla \cdot (\delta \boldsymbol{A} \times \boldsymbol{A}) + \delta \boldsymbol{A} \cdot \boldsymbol{B},\end{aligned}$$

and then integrating by parts yields

$$0 = \int dr^3 \delta \boldsymbol{A} \cdot (\nabla \times \boldsymbol{B} - 2\lambda \boldsymbol{B}), \tag{1.7}$$

where the surface integral terms ($\oint (\delta \boldsymbol{A} \times \boldsymbol{B}) \cdot d\boldsymbol{s}$ and $\oint (\delta \boldsymbol{A} \times \boldsymbol{A}) \cdot d\boldsymbol{s}$) vanish due to the boundary condition. Thus, after redefining λ, the problem reduces to

$$\nabla \times \boldsymbol{B} = \lambda \boldsymbol{B}. \tag{1.8}$$

The minimum energy states satisfying this condition are called Taylor states. Since the current density $\boldsymbol{J} = \nabla \times \boldsymbol{B}/\mu_0 \parallel \boldsymbol{B}$, the $\boldsymbol{J} \times \boldsymbol{B}$ force vanishes and so the Taylor states are force-free.

For axis-symmetric systems, the solution of equation (1.8) can be expressed in terms of the poloidal flux ψ as [1, chap. 4]

$$\boldsymbol{B} = \frac{1}{2\pi} (\nabla \psi \times \nabla \phi + \lambda \psi \nabla \phi), \tag{1.9}$$

where ϕ indicates the azimuthal (toroidal) angle. If the system is confined in a conducting spherical volume of radius a, the poloidal flux function is

$$\psi(r, \theta) = 2\pi a B_0 \, r j_1(\lambda r) \sin^2 \theta, \tag{1.10}$$

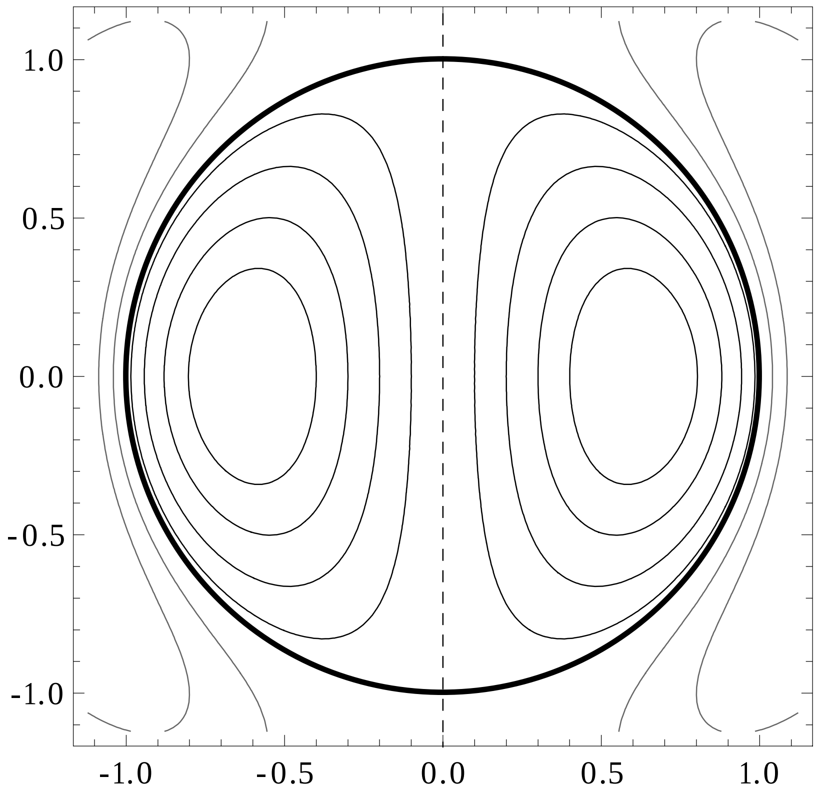

Figure 1.1: Flux surfaces of an ideal spheromak. Thick solid circle represents the boundary of the conducting spherical wall which corresponds to the bounding separatix surface $\psi = 0$. Vertical dashed line is the axis of symmetry. Length scales are normalized by the radius a of the sphere.

where r is the distance from the origin, θ is the angle from the axis of symmetry, and j_1 is the first-order spherical Bessel function ($j_1(x) = x^{-2} \sin x - x^{-1} \cos x$).

Spheromaks are represented by equations (1.9) and (1.10) in its most idealized form (i.e., spherical shape) and are one of the force-free Taylor states. The flux surfaces of an idealized spheromak are illustrated in figure 1.1.

1.1.3 Formation schemes and role of flux conserver

Helicity must be injected into the plasma before it can become a spheromak. A variety of injection schemes have been successful in producing spheromak plasmas such as magnetized coaxial gun, z-θ pinch, conical θ pinch, and flux core [4]. The success of these many injection methods implies that spheromaks are one of the most natural plasma structures. All the injection methods share a common feature and can be summarized in figure 1.2. In the figure, each electrode intercepts vacuum magnetic field lines and thus has a finite magnetic flux ψ. The vacuum magnetic field is generated by external coils. When an electric potential $\Delta\varphi$ is applied across the electrodes, helicity will be injected according to equation (1.5), $dK/dt = 2\psi\Delta\varphi$. Since the plasma is conducting, the helicity injection induces a current flowing along the field lines. After the helicity injection, the plasma dissipates its magnetic energy via various instabilities and relaxes into the force-free spheromak state.

In practice, most spheromak formation schemes also include a conducting surface called flux conserver to stabilize spheromaks against instabilities such as tilt and shift modes [5] [1, chap. 10]. The wall image currents of the flux conserver interact with the spheromak and confine it within the flux conserver volume.

The eigenvalue λ in the force-free equation (1.8) is determined by the geometrical shape of the wall confining the spheromak, typically the flux conserver. For example,

$$\lambda = y_{11}/a, \quad \text{for a spherical volume of radius } a, \tag{1.11}$$

$$\lambda = \sqrt{(x_{11}/a)^2 + (\pi/h)^2}, \quad \text{for a cylinder of radius } a \text{ and height } h, \tag{1.12}$$

where y_{11} is the first zero of the spherical Bessel function j_1, x_{11} is the first zero of the Bessel function J_1, and the aspect ratio of the cylinder $h/a < 1.7$.

1.2 Coplanar coaxial plasma gun – spheromak formation without flux conserver

The most common and least complex method to generate spheromaks is to use the magnetized coaxial gun [6]. The device is composed of a pair of concentric cylindrical electrodes (inner and outer) linked by a vacuum magnetic field produced by an external coil as shown schematically in figure 1.3a. The eigenvalue λ of the spheromak produced by the coaxial gun is related to the total gun current I_{gun} and the total

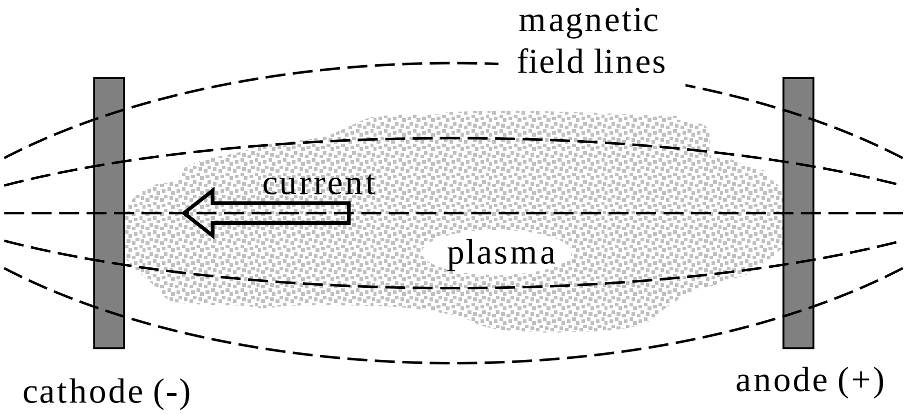

Figure 1.2: Generic spheromak formation scheme (adapted from [1, chap. 7]). The externally generated vacuum magnetic field lines are indicated by dashed lines. An electric potential applied along the field injects helicity according to equation (1.5). Since the plasma is conducting, a field-aligned current is also generated.

magnetic flux intercepting the inner electrode as

$$\lambda = \frac{\|\nabla \times \boldsymbol{B}\|}{B} = \frac{\mu_0 J}{B} = \frac{\mu_0 J S_{\text{gun}}}{B S_{\text{gun}}} \sim \frac{\mu_0 I_{\text{gun}}}{\psi_{\text{gun}}}, \tag{1.13}$$

where S_{gun} is the surface area of the gun. Thus, it is convenient to define this gun source property as

$$\lambda_{gun} \equiv \frac{\mu_0 I_{\text{gun}}}{\psi_{\text{gun}}}. \tag{1.14}$$

For clarification, the spheromak λ will be denoted as λ_{sph}.

A modified coaxial gun design composed of planar electrodes instead of cylindrical electrodes has been proposed by Bellan and constructed by Hsu and Bellan [7] [8] [9] (see figure 2.2). The planar configuration has three main advantages.

(1) The planar gun has larger area and thus requires smaller magnetic field to provide the same ψ_{gun}.

(2) Improved λ-matching [1, chap. 8 and 12]: The eigenvalue λ is an intensive property of the plasma like the temperature in thermodynamics. The eigenvalue λ comes about by minimizing the magnetic energy under a constant helicity and the temperature by maximizing the entropy under a constant internal energy. Helicity flows along λ gradients to minimize the magnetic energy much like

heat (energy) flows along temperature gradients to maximize the entropy. Conventional coaxial guns are much smaller in volume than the spheromaks they produce, and so λ_{gun} poorly matches λ_{sph} since λ is a geometrical property of a volume. The larger planar gun has a better matching λ_{gun}, resulting in less λ gradient and thus less plasma instability.

(3) Absence of a flux conserver and the planar geometry of the electrodes provide better diagnostic access to the entire plasma evolution including the source gun region. In particular, direct imaging of the gun-produced plasmas became possible and has revealed the unique dynamics of the plasma structures (see figure 4.1 for example).

Spheromaks have been successfully produced by the planar gun and the spheromak formation mechanism has been studied in detail [9]. The kink instability [10, chap. 10] of the gun-produced plasma jets has been identified as a poloidal flux amplification mechanism, which is necessary for spheromak formation. Onset of the kink instability observed experimentally was shown to agree with the Kruskal-Shafranov limit, i.e., the plasma becomes kink-unstable when its axial length becomes greater than $1/\lambda_{\text{gun}}$.

1.3 Collimated plasma structures

In addition to spheromak applications of the planar gun, images of the gun-produced plasmas showed remarkable similarities with naturally occurring plasmas such as solar prominences and astrophysical jets [8]. In particular, the collimated tube-like structure (i.e., long tube with a constant area cross-section) is the most conspicuous common feature. The laboratory plasmas produced by the planar gun are compared with the naturally occurring plasmas in figures 1.4a and 1.4b.

Solar prominences are arch-shaped magnetized plasma structures protruding from the surface of the Sun [11]. Typical prominences extend over many thousands of kilometers and are stable in general lasting for days or even months. The sub-category called coronal loops are especially known for the highly collimated and elongated

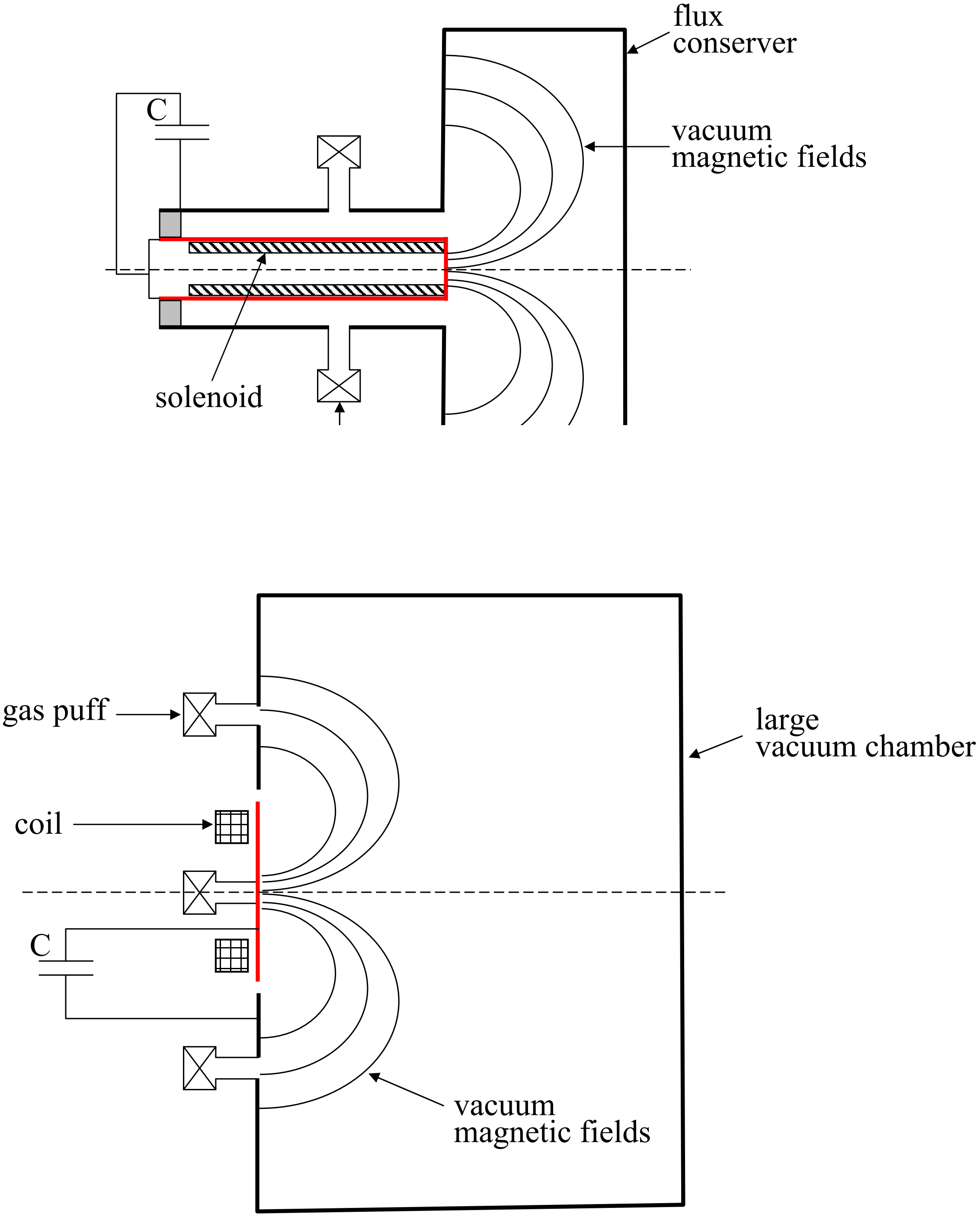

(b) Planar coaxial gun

Figure 1.3: Schematic drawings of (a) conventional cylindrical coaxial magnetized gun and (b) the planar coaxial magnetized gun.

magnetic flux tubes. Plasma particles are localized inside the collimated solar prominences, and so there exists a large density gradient across their boundaries. The stability of the solar prominences despite the large density gradient has not been understood yet.

Astrophysical jets are also highly collimated and emanate from massive astronomical objects such as active galactic nuclei, young stellar objects, and high-mass X-ray binaries. The axial extent of the jets (10^{15}–10^{22} m) are many orders of magnitude greater than the source objects and the jet velocities can be relativistic. Magnetic fields observed in some astrophysical jets suggest that magnetohydrodynamics (MHD) plays an important role governing jet formation and collimation [12].

1.4 MHD pumping mechanism

Motivated by the observations of collimated plasma structures both in nature and laboratory, Bellan proposed a universal MHD pumping process [13] which explains why the collimated plasma-filled magnetic flux tubes are ubiquitous. The model is based on the concept of frozen-in magnetic flux and is summarized below.

1.4.1 Frozen-in flux – magnetic Reynolds number

Dynamics of magnetized plasmas is described by the Maxwell's equations and the Ohm's law,

$$\nabla \times \boldsymbol{B} = \mu_0 \boldsymbol{J}, \tag{1.15}$$

$$\nabla \cdot \boldsymbol{B} = 0, \tag{1.16}$$

$$\nabla \times \boldsymbol{E} = -\frac{\partial \boldsymbol{B}}{\partial t}, \tag{1.17}$$

$$\boldsymbol{J} = \sigma(\boldsymbol{E} + \boldsymbol{U} \times \boldsymbol{B}), \tag{1.18}$$

where σ is the electrical conductivity and $\boldsymbol{U}$ is the plasma flow velocity. The displacement current term is ignored in the $\nabla \times \boldsymbol{B}$ equation provided that the characteristic

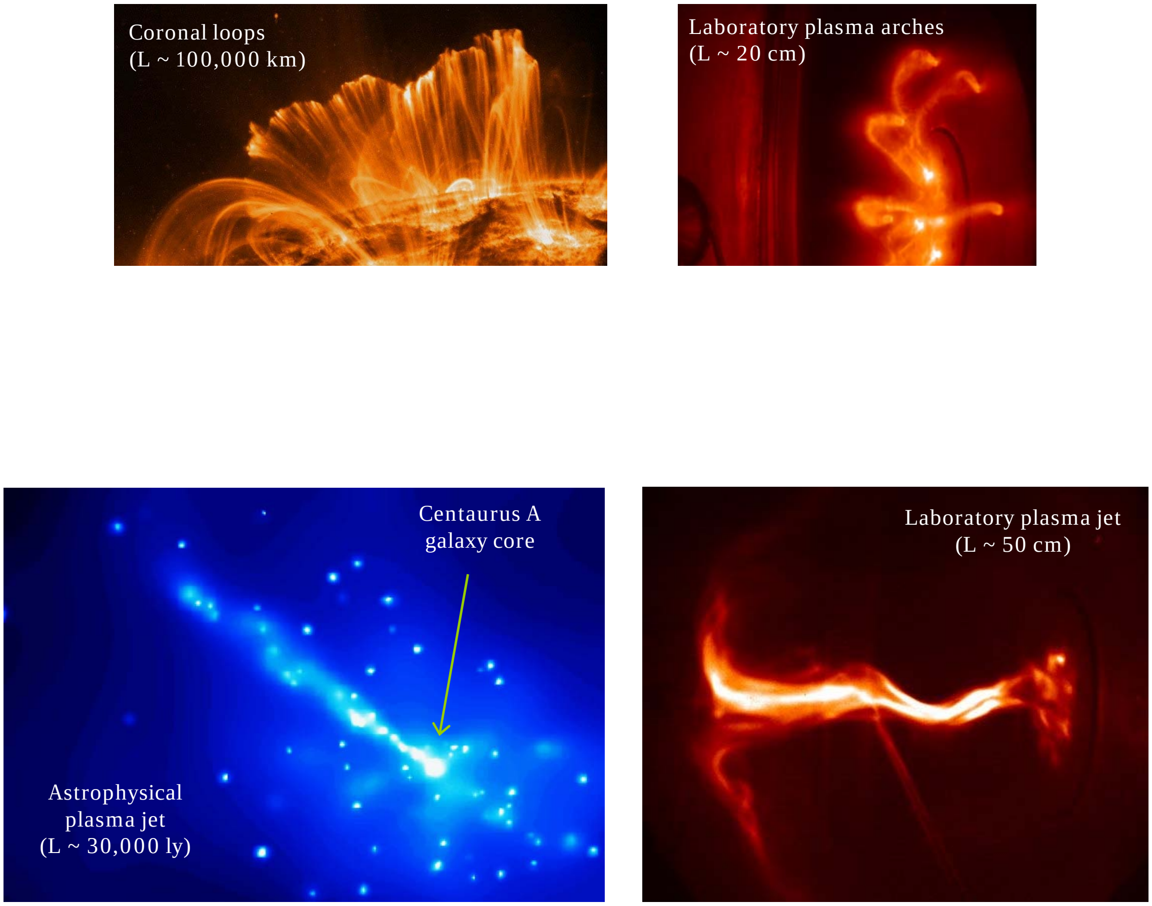

(b) Astrophysical jet

Figure 1.4: (a) Solar coronal loops (image from the Transition Region and Coronal Explorer) compared with the laboratory plasma arches. (b) Astrophysical jet (Centaurus A galaxy; Chandra X-ray/Radio image) compared with the laboratory plasma jet. The laboratory plasmas are produced by the planar coaxial magnetized gun.

speed is much less than the speed of light. From these equations, the rate of growth of magnetic field strength can be derived:

$$\begin{aligned}\frac{\partial \boldsymbol{B}}{\partial t} &= -\nabla \times (\boldsymbol{J}/\sigma) - \boldsymbol{U} \times \boldsymbol{B} = \frac{-1}{\mu_0 \sigma} \nabla \times \nabla \times \mathbf{B} + \nabla \times (\mathbf{U} \times \mathbf{B}) \\ &= \frac{1}{\mu_0 \sigma} \nabla^2 \mathbf{B} + \nabla \times (\mathbf{U} \times \mathbf{B}). \end{aligned} \tag{1.19}$$

The first term (diffusion term) on the right-hand side represents the rate of diffusion of magnetic fields through plasma due to the finite electrical resistivity $\eta = 1/\sigma$. The second term (convection term) represents the rate of change of the magnetic field strength due to the plasma flow. In ideal MHD ($\boldsymbol{E} + \boldsymbol{U} \times \boldsymbol{B} = 0$), the diffusion term vanishes and the magnetic flux is completely frozen into the plasma flow. In order to see this, consider the magnetic flux $\Phi(t)$ enclosed by a closed surface $S(t)$ in the plasma at time t,

$$\Phi(t) = \int_{S(t)} \boldsymbol{B} \cdot d\boldsymbol{s}. \tag{1.20}$$

Taking the convective derivative of the flux $\Phi(t)$ using the Leibniz integral rule yields,

$$\begin{aligned}\frac{D\Phi(t)}{Dt} &= \oint_{\partial S(t)} \boldsymbol{B} \boldsymbol{\cdot} \boldsymbol{U} \times d\boldsymbol{l} + \int_{S(t)} \frac{\partial \boldsymbol{B}}{\partial t} \cdot d\boldsymbol{s} \\ &= \oint_{\partial S(t)} \boldsymbol{B} \times \boldsymbol{U} \cdot d\boldsymbol{l} + \int_{S(t)} \frac{\partial \boldsymbol{B}}{\partial t} \cdot d\boldsymbol{s} \\ &= \int_{S(t)} \nabla \times (\boldsymbol{B} \times \boldsymbol{U}) \cdot d\boldsymbol{s} + \int_{S(t)} \frac{\partial \boldsymbol{B}}{\partial t} \cdot d\boldsymbol{s} \\ &= \int_{S(t)} \left[\nabla \times (\boldsymbol{B} \times \boldsymbol{U}) + \frac{\partial \boldsymbol{B}}{\partial t} \right] \cdot d\boldsymbol{s} \\ &= \int_{S(t)} [\nabla \times (\boldsymbol{B} \times \boldsymbol{U}) - \nabla \times \boldsymbol{E}] \cdot d\boldsymbol{s} \\ &= \int_{S(t)} -\nabla \times (\boldsymbol{E} + \boldsymbol{U} \times \boldsymbol{B}) \cdot d\boldsymbol{s} = 0. \end{aligned}$$

Thus, the flux $\Phi(t)$ is invariant in the frame of the moving plasma, i.e., the magnetic flux is frozen into the plasma.

The magnitude of the convection term relative to the diffusion term determines whether the magnetic field at a point in the fluid may build up fast enough before it diffuses into the surroundings. The condition for magnetic field building up by fluid motion is that the frozen-in flux term is much greater than the diffusion term:

$$\|\nabla \times (\boldsymbol{U} \times \boldsymbol{B})\| \sim \frac{UB}{L} \gg \left\| \frac{1}{\mu_0 \sigma} \nabla^2 \mathbf{B} \right\| \sim \frac{B}{\mu_0 \sigma L^2}$$

$$\mu_0 \sigma U L \gg 1, \tag{1.21}$$

where L is the characteristic length over which magnetic field varies.

Hence, the quantity $\mu_0 \sigma U L$, called the magnetic Reynolds number (R_m) or Lundquist number, is of fundamental importance in magnetized plasma. For plasmas with a small magnetic Reynolds number, there is no large gradient of magnetic fields in the plasma and the action of magnetic fields can be considered like a viscous drag on the fluid due to induced eddy currents. For plasmas with a large magnetic Reynolds number, the magnetic flux is carried by the fluid. The action of magnetic fields can now be thought as if a lateral pressure $B^2/2\mu_0$ is applied normal to the lines of force and a longitudinal tension $B^2/2\mu_0$ is applied along the lines of force. The magnetic Reynolds number is often obtained from the ratio of two characteristic time scales:

$$R_m = \tau_r / \tau_A, \tag{1.22}$$

where the resistive diffusion time scale $\tau_r = \mu_0 \sigma L^2$ and the Alfvén time scale $\tau_A = L/U$. The diffusion time scale is obtained by considering

$$\left(\frac{\partial \boldsymbol{B}}{\partial t} \right)_{\text{diffusion}} = \frac{1}{\mu_0 \sigma} \nabla^2 \boldsymbol{B},$$

$$B/\tau_r \sim \frac{B}{\mu_0 \sigma L^2} \Longrightarrow \tau_r \sim \mu_0 \sigma L^2. \tag{1.23}$$

$R_m \gg 1$ for our plasmas and so the magnetic flux is frozen into the plasma motion.

1.4.2 MHD pumping and collimation model

Consider a cylindrical magnetic flux tube as illustrated in figure 1.5. Initially, the flux tube is flared in the middle and has no current, and the plasma particles are

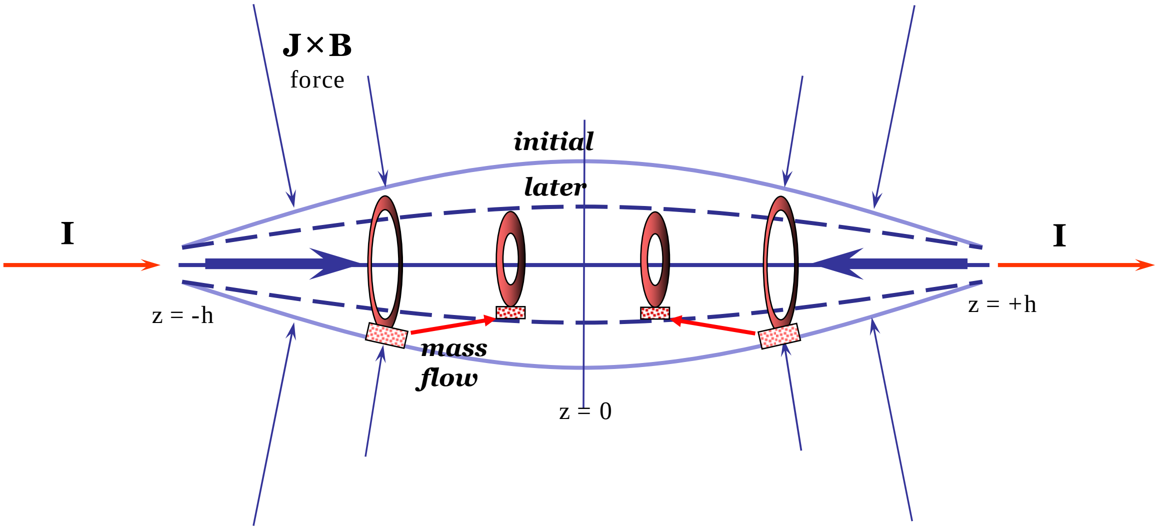

Figure 1.5: Collimation of initially flared flux tube (adapted from [13]). Solid lines are initial magnetic flux surfaces and dashed lines are the same flux surfaces at a later time.

concentrated near the foot points. An electric potential is applied along the field lines and subsequently an axial current starts to ramp up. Note that this situation coincides with the generic configuration for helicity injection discussed in section 1.2.

The $\boldsymbol{J} \times \boldsymbol{B}$ force has a net axial component due to the flared geometry and creates axial flows.

$$\begin{aligned} \rho \frac{dU_z}{dt} &= (\boldsymbol{J} \times \boldsymbol{B})_z - \frac{\partial P}{\partial z} = J_r B_\phi - J_\phi B_r - \frac{\partial P}{\partial z} \\ &= -\frac{\partial}{\partial z}\left(\frac{B_\phi^2}{2\mu_0}\right) - \frac{\partial P}{\partial z} - J_\phi B_r = -\frac{\partial}{\partial z}\left(\frac{B_\phi^2}{2\mu_0} + P\right) - J_\phi B_r \\ &\left(\because \mu_0 J_r = -\frac{\partial B_\phi}{\partial z} \quad \text{due to the cylindrical symmetry}\right), \end{aligned} \tag{1.24}$$

where U_z is the z-directed flow velocity, ρ is the mass density, and B, J, and P are the magnetic field strength, current density, and pressure, respectively.

The radial component of the $\boldsymbol{J} \times \boldsymbol{B}$ describes the pinch force. The pinch force is greater near the foot points since both the current density $\boldsymbol{J}$ and the magnetic field strength are greater there than in the middle. Thus, without a radial force balance, the plasma will become more constricted at the foot points and eventually disrupt (sausage instability [10, chap. 10]). To exclude this unstable situation from consideration, assume that the pressure buildup due to the pinching quickly balances the pinch force:

$$\frac{\partial P}{\partial r} = -J_z B_\phi. \tag{1.25}$$

Also, assume that the current density J_z is uniform inside a cross section of the flux tube, i.e., $J_z(z,r) = J_z(z) = I_0/\pi a(z)^2$, where I_0 is the total current flowing in the flux tube and the local tube radius $a(z)$ describes the flaring of the flux tube. Then,

$$\begin{align}
B_\phi &= \frac{\mu_0(J_z \pi r^2)}{2\pi r} = \frac{\mu_0 J_z r}{2}, \tag{1.26}\\
\frac{\partial P}{\partial r} &= -J_z B_\phi = -\frac{\mu_0 J_z^2 r}{2}, \tag{1.27}\\
P &= -\frac{\mu_0 J_z^2}{4}(r^2 - a^2) = \frac{B_\phi^2}{\mu_0}\left(\frac{a^2}{r^2} - 1\right). \tag{1.28}
\end{align}$$

Thus, equation (1.24) becomes

$$\begin{align}
\rho \frac{dU_z}{dt} &= -\frac{\partial}{\partial z}\left[\frac{B_\phi^2}{\mu_0}\left(\frac{a^2}{r^2} - \frac{1}{2}\right)\right] - J_\phi B_r \nonumber\\
&= -\frac{\partial}{\partial z}\left[\frac{B_{\phi,a}^2}{\mu_0}\left(1 - \frac{r^2}{2a^2}\right)\right] - J_\phi B_r, \tag{1.29}
\end{align}$$

where $B_{\phi,a} = \mu_0 I_0/2\pi a$ is the azimuthal magnetic field at the flux tube radius a. Near the axis, $J_\phi B_r$ and r^2/a^2 are very small, yielding an approximate expression

$$\rho \frac{dU_z}{dt} \approx -\frac{\partial}{\partial z}\left[\frac{B_{\phi,a}^2}{\mu_0}\right]. \tag{1.30}$$

Thus, the magnetic energy density term $B_{\phi,a}^2/\mu_0$ acts like an effective potential and so the plasma particles will move axially falling down this potential. Equation (1.30) can also be expressed in terms of the flux tube flaring ($\partial a/\partial z$):

$$\rho \frac{dU_z}{dt} \approx -\frac{\partial}{\partial z}\left[\frac{\mu_0 I_0^2}{4\pi^2 a^2}\right] = \frac{\mu_0 I^2}{2\pi^2 a^3}\frac{\partial a}{\partial z}. \tag{1.31}$$

The potential $B_{\phi,a}^2/\mu_0$ has the minimum at the middle of the flux tube due to the flared geometry of the flux tube. Therefore, counter-streaming axial flows will be generated from both foot points toward the middle. The counter-streaming flows collide with each other and so stagnate in the middle, resulting in accumulation of plasma particles there. By the frozen-in flux condition, the azimuthal magnetic flux carried by the flows also accumulates in the middle, which increases the azimuthal magnetic field strength B_ϕ. As a result, the pinch force $J_z B_\phi$ increases and squeezes the magnetic flux tube in the middle. Thus, the magnetic flux radius becomes uniform axially, i.e., the magnetic flux tube becomes collimated.

1.5 Overview of the following chapters

The present thesis work addresses the experimental verification of the MHD pumping model as a universal collimation mechanism. The experimental setup to produce collimated plasma tubes is described in chapter 2 and the diagnostic devices to measure the plasma properties are described in chapter 3. In particular, construction of a high-resolution spectroscopic system for the plasma density and flow velocity measurements is described in detail. In chapter 4, experimental results are presented and discussed in detail, showing that the observations are consistent with the MHD pumping model. A theoretical background for the plasma density diagnostics is provided in chapter 5 and a simple method for obtaining the plasma density from spectral line profiles is explained in chapter 6. A summary of this thesis work is given in the final chapter.

Chapter 2

Experimental setup – boundary conditions

The experimental setup used in this work provides the physical boundary conditions on the evolution of plasma structures. The experimental setup has been developed and improved over a decade and will be summarized in this chapter. Knowledge of the experimental setup and hence the boundary conditions of the experiment is necessary to comprehend the motivations behind the experiment as well as to properly interpret experimental observations.

The experimental setup comprises five major components: vacuum chamber, spheromak plasma gun, gas injection system, timing system, and diagnostics. The vacuum chamber provides a free space into which plasma can evolve. The spheromak plasma gun produces magnetized plasma structures. The plasma gun is mounted on the north end dome of the chamber as shown in figure 2.1. The plasma gun comprises cathode and anode electrodes, gun capacitor bank, stuffing flux system, and gas feed lines. The gas injection system delivers high pressure gas into the vacuum on a msec time scale. The timing system consists of two independent sub-timing modules: main timing and diagnostic timing. The main timing module triggers various power supplies for the plasma gun and the gas injection. The diagnostic timing module triggers diagnostic devices in sync with plasma breakdown. The diagnostic devices will be discussed in the next chapter.

2.1 Vacuum chamber

The vacuum chamber is shown schematically in figure 2.1. The vacuum chamber provides a free boundary condition for plasmas produced in the present experiment; the plasma structures evolve without much interaction with the chamber wall because the plasma dimensions (1–10 cm in diameter and 10–50 cm in length) are much smaller than the chamber dimensions. This is in contrast to other spheromak experiments where the plasma geometry and the magnetic field configuration are essentially constrained by the chamber wall.

The vacuum is maintained at a background pressure $P_{\mathrm{bkg}} = 1\text{–}2 \times 10^{-7}$ torr (corresponding to a particle density $\sim 5 \times 10^{15}$ m^{-3} at room temperature) by the cryopump (APD-12S; ∼1000 liters/sec pumping speed for air). The pressure is monitored by a Bayart-Alpert-type ionization gauge. Maintaining a good vacuum is important since it is observed that the plasma evolution is hampered in a poor vacuum condition $P_{\mathrm{bkg}} \gtrsim 10^{-5}$ torr. The vacuum quality is compromised primarily by two factors; (1) desorption of gas molecules (especially water) absorbed by the chamber wall when exposed to atmosphere and (2) leaks through O-rings and gaskets. These two factors are indistinguishable in practice and observed as a single effective leak. The effective leak of the chamber can be estimated by a simple procedure described in appendix A. In case of a large leak, this procedure can be applied to quantify the leak and thus facilitate the location of the leak.

2.2 Spheromak plasma gun

2.2.1 Coplanar coaxial electrodes

The electrodes of the plasma gun are planar (figure 2.2a) in contrast to cylindrical electrodes used in other spheromak experiments. The planar configuration permits direct observation of the entire plasma formation process. The inner electrode (cathode) is a disc copper plate and has eight gas orifices evenly spaced in a circle. The outer electrode (anode) is an annular copper plate and is coaxial and coplanar with

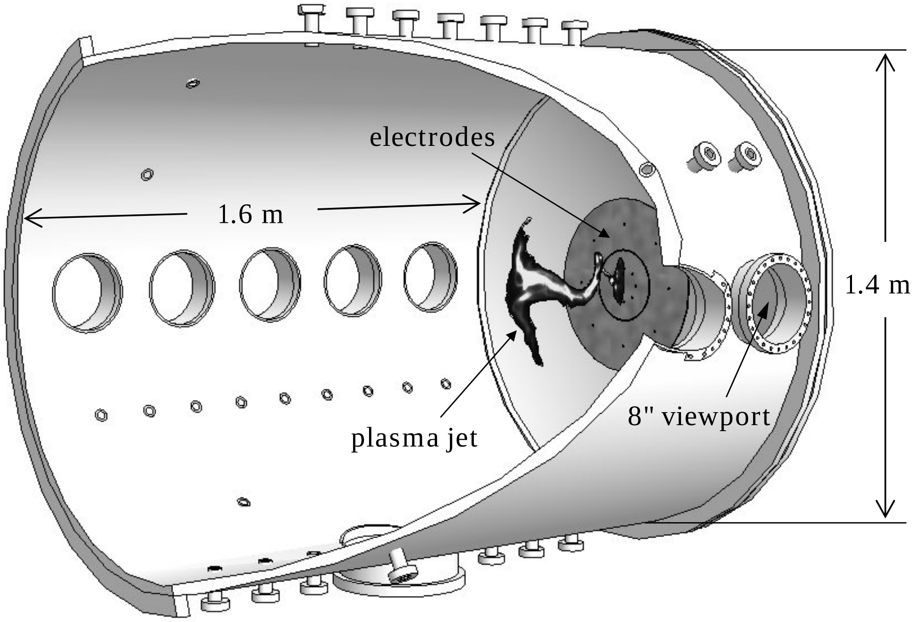

Figure 2.1: Vacuum chamber. Total volume is $\sim$2.4 m^3 and the base pressure is 1–2 $\times$ 10^{-7} torr. The chamber dimensions are much greater than plasma. An image of a kinked plasma jet is inset for size comparison. The plasma expands freely without interaction with the chamber wall.

the cathode. The anode also has eight orifices at locations corresponding to the cathode orifices. The gas orifices are channeled to the gas injection system explained in the section 2.3. The small annular gap between the two electrodes is 6 mm wide.

The condition for gas breakdown by the electrodes can be qualitatively understood by the empirical law known as Paschen's law [14]; the breakdown voltage V_s is a function of pd, gas pressure(p) times discharge path length(d). The breakdown voltage V_s has a minimum at some $pd = (pd)_{\rm min}$ called Paschen minimum, increases slowly for $pd > (pd)_{\rm min}$, and increases rapidly for $pd < (pd)_{\rm min}$. The Paschen minimum $(pd)_{\rm min}$ for common gases such as N_2, H_2, and Ar used in this work is $\sim$1 cm·torr. A path connecting an inner gas orifice and an outer gas orifice gives $pd \sim (pd)_{\rm min}$ since $p \sim 0.5$ torr near the orifices (cf. section 2.3) and the path length d is a few cm. Hence, a sufficiently high voltage applied to the electrodes will break down the gas along such paths. However, $pd \ll (pd)_{\rm min}$ in the small gap between the electrodes because of low $p \sim 10^{-7}$ torr and small $d = 0.6$ cm, and so there will be no gas breakdown across the gap. No breakdown will occur in the tight space (figure 2.2b) between the re-entrant port (at high voltage) and the chamber wall (at ground) for the same reason.

High voltage (3–8 kV) is applied across the electrodes using a 120 μF capacitor bank (high voltage (HV) gun bank) switched by an ignitron. The gun bank supplies a current of the order of 60–150 kA flowing through the plasma.

2.2.2 Stuffing flux system

The bias coil is mounted at the end-plate of the re-entrant port flush against the inner electrode. It produces an axisymmetric bias poloidal field as illustrated in figure 2.2b. The coil current is supplied by a 14.4 mF power supply and peaks at ~6.5 msec after the power supply is triggered as traced by a current monitor. The time scale of the coil current is much greater than the ~20 μsec plasma lifetime so that the bias poloidal field is constant over the duration of the plasma.

The poloidal flux is attenuated by the skin effect (eddy current) of both the copper electrode (3.2 mm thick) and the stainless steel end-plate (9.5 mm thick). The skin depth is the distance δ through which the amplitude of a plane wave decreases by a factor e^{-1} and is given by

$$\delta = \sqrt{\tau/\pi\sigma\mu} \approx \begin{cases} 9.3 \text{ mm} & \text{for copper} \\ 62 \text{ mm} & \text{for stainless steel,} \end{cases} \tag{2.1}$$

where $\tau \approx 20$ msec is the pulse length of the coil current, σ is the electrical conductivity, and μ is the permeability ($\approx \mu_0$ for non-magnetic materials). Hence, the magnetic field strength is attenuated by a factor of $e^{-3.2/9.3} \times e^{-9.5/62} \approx 0.6$ and so is the poloidal flux. The peak timing of the poloidal flux is also delayed by the skin effect and is different from the peak timing of the coil current. The measured poloidal flux peaks at ~10 msec with the peak flux of 1.4 mWb per 100 V, linear with the power supply voltage.

The nominal LCR parameters of the stuffing flux system are 2.8 mH coil inductance, 14.4 mF power supply capacitance, and 0.4 Ω DC resistance. However, the

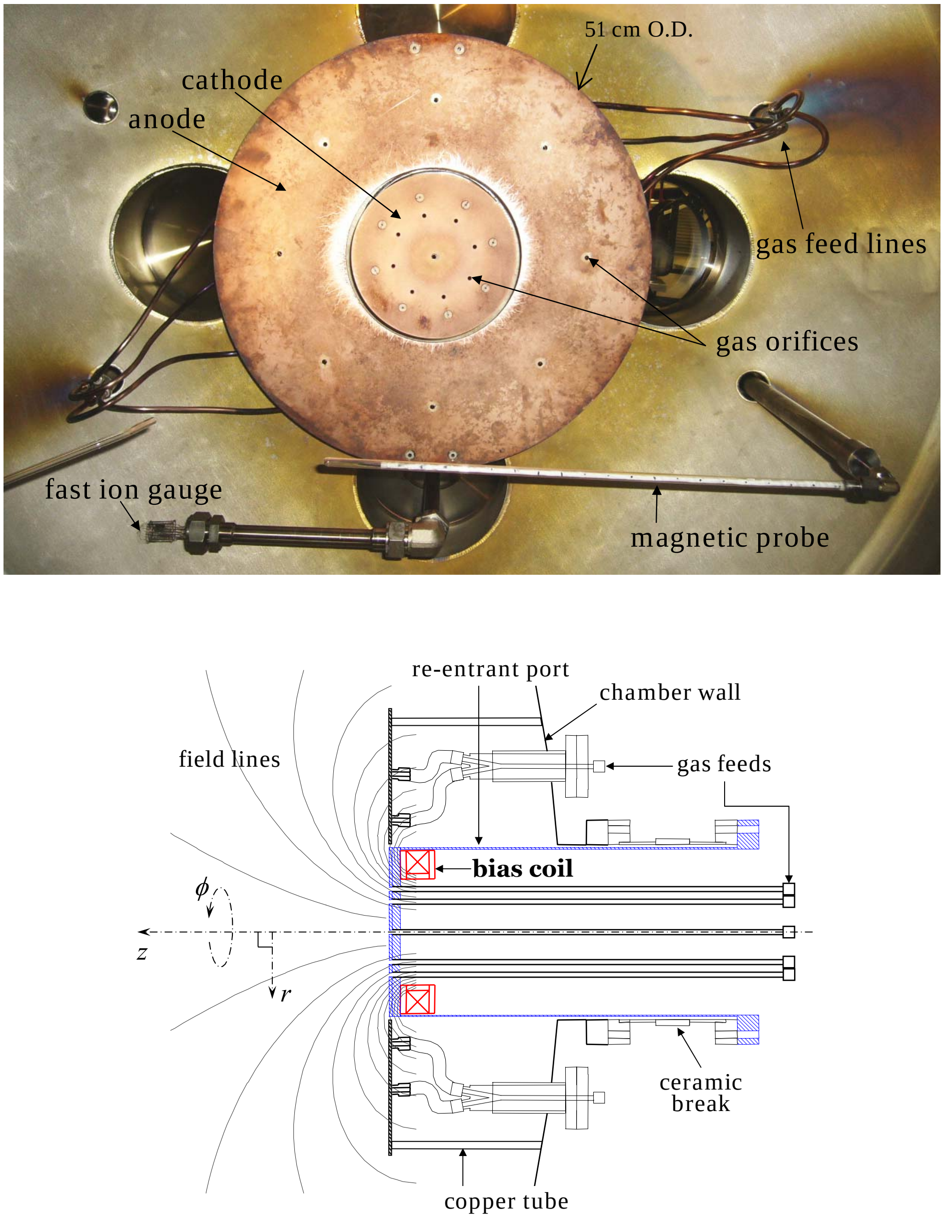

(b) side view (schematic)

Figure 2.2: Spheromak plasma gun (designed by S. C. Hsu [7]). Inner electrode is an oxygen-free high-conductivity (OFHC) copper disc plate of 19.1 cm (7.5″) diameter. Outer electrode is an OFHC copper annulus plate of 50.8 cm (20″) outer diameter and 20.3 cm (8″) inner diameter. The electrodes are 3.2 mm (1/8″) thick. The inner electrode is mounted on the re-entrant port, which is insulated from the chamber by a ceramic break. The outer electrode is mounted on four hollow copper tubes (two at the bottom and the other two at the top of the electrode), each of which is anchored to the chamber wall by a stainless steel threaded rod. Axisymmetric poloidal field is produced by the bias coil of 110 turns located behind the inner electrode.

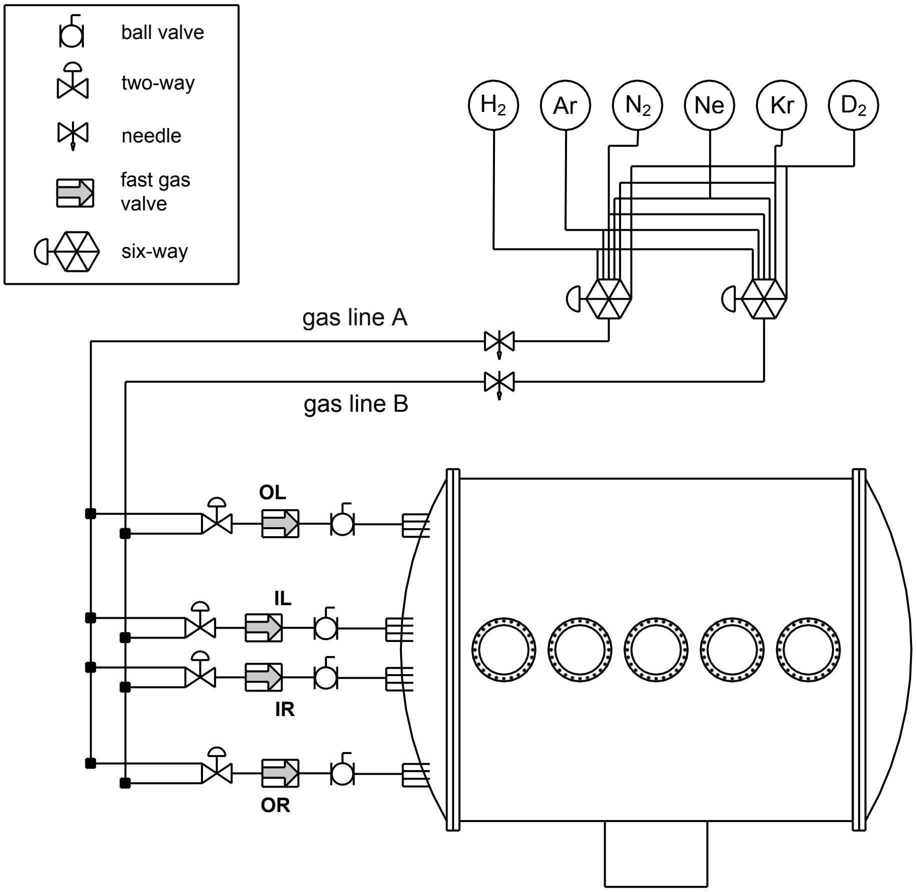

Figure 2.3: Gas line plumbing (designed by Setthivoine You). There are two independent gas lines labeled by gas line A and B. Each gas line has a six-way valve connected to six high-purity gas cylinders. The six-way valve selects a gas to feed the gas line. Each of the four fast gas valves can be connected to either the gas line A or B by a two-way valve.

effective inductance (∼1.6 mH) as estimated from current traces is smaller than the nominal inductance due to the eddy currents induced on the inner electrode [15]. The eddy currents exert a large repulsive force on the bias coil. The measured effective capacitance (∼19 mF) is somewhat larger than the nominal capacitance.

2.3 Gas injection system

2.3.1 Flexible plumbing

A flexible plumbing system shown schematically in figure 2.3 has been developed by S. You to make possible a variety of gas injection scenarios. The plumbing system was later reconfigured to the current setup by S. You and G. S. Yun and extended to the solar prominence simulation experiment [11] by S. K. P. Tripathi and E. V. Stenson. In each experiment, a single gas species can be injected into the chamber or two gas species can be injected in eight different ways.

The plumbing system is divided into two independent gas lines (labeled as A and B in the figure). A single gas species is selected among six gas species and fed into each gas line. The gas is injected into the vacuum chamber by four fast gas valves. Each fast gas valve is connected to a manifold, which splits the gas flow into four gas feed lines. The fast valves are labeled as inner left (IL), inner right (IR), outer left (OL), and outer right (OR) according to their locations. The IL valve injects gas through the four orifices on the left half plane of the inner electrode and the IR valve injects gas through the other four orifices on the right. The OL and OR valves inject gas through orifices on the outer electrode in the same manner.

2.3.2 Fast gas valve

A pressurized gas (60–100 psi) fills the 2.7 cm^3 plenum of the fast gas valve (figure 2.4). The diaphragm loaded by a spring presses an O-ring against the gas line, sealing off the plenum from vacuum. A coil is wound underneath the diaphragm. When a pulsed current flows in the coil, a current of the opposite sense (i.e., eddy current) is induced on the diaphragm and the diaphragm is pushed up against the spring and the back pressure. This action temporarily relieves the O-ring seal, allowing the gas to flow from the plenum into the vacuum by a large pressure gradient.

The total throughput of the fast gas valve depends on the back pressure and the coil current. The throughput can be measured by the average pressure rise per puff.

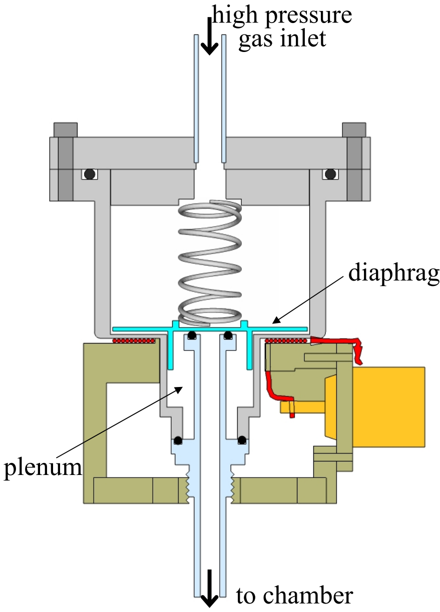

Figure 2.4: Fast gas valve (designed by P. M. Bellan). A high pressure gas fills the valve body including the small plenum (2.3 cm^3) underneath the diaphragm. When a current pulse flows through the coil, an eddy current is induced on the diaphragm. The repulsive force between the coil current and the eddy current opens the diaphragm for a few msecs against the spring force (spring constant = 1600 N/m) and the back pressure force (1–10 N). About 20% of the gas in the plenum is injected into the chamber during the opening. The total gas throughput is controlled by the coil current and the back pressure.

For a typical operation of 70 psi nitrogen in the gas line, a single fast valve gives a pressure rise $\Delta P \sim 0.8$ mtorr ≈ 0.1 Pa per puff in the vacuum chamber. Since the chamber volume V is 2.4 m^3, the total number of puffed particles is

$$N_{\mathrm{T}} = \Delta P \cdot V/kT = 5 \times 10^{19}, \tag{2.2}$$

which is about 20% of the total number of particles available in the plenum. It will be shown later that about 20% of the puffed particles are used in making a plasma jet (see section 4.4). Most of the gas particles are pumped into the chamber within ~5 msec (cf. appendix B), giving the average particle flux rate

$$dN_{\mathrm{T}}/dt \approx 10^{19}\ \mathrm{msec}^{-1}. \tag{2.3}$$

Since there are four gas lines connected to each fast gas valve, the flux rate for a single gas line is

$$\frac{dN_1}{dt} = \frac{1}{4}\frac{dN_{\mathrm{T}}}{dt} \approx 2 \times 10^{18}\ \mathrm{msec}^{-1}. \tag{2.4}$$

It is interesting to note that this flux rate is comparable to the theoretical flux rate for steady-state flow of rarefied gases through tubes [16],

$$K = W \cdot S \cdot \frac{n_1 u_1}{4} = (8a/3L) \cdot \pi a^2 \cdot \frac{n_1}{4}\sqrt{\frac{8kT}{\pi m}}, \tag{2.5}$$

where W is transmission probability (also known as Clausing factor), S, a, and L are the cross-sectional area, radius, and length of the tube, respectively, n_1 is the upstream particle density, u_1 is the upstream average particle speed, and m is the particle mass. Upstream properties are denoted by the subscript 1 and downstream properties by the subscript 2. It is assumed that $n_1 \gg n_2$ and the gas temperature T is constant. Using $a \approx 2$ mm and $L \approx 1$ m for our gas lines, the flux rate for $P_1 = 70$ psi nitrogen gas puffing ($n_1 = 1.2 \times 10^{26}\ \mathrm{m}^{-3}$ and $u_1 = 470$ m/sec at $T = 300$ K) is

$$K \approx 10^{18}\ \mathrm{msec}^{-1}. \tag{2.6}$$

The downstream density n_2 at the orifice may be estimated by assuming $u_1 = u_2$ and using the continuity of the flux rate K:

$$\begin{aligned} & K = (8a/3L) \cdot \pi a^2 \cdot \frac{n_1 u_1}{4} = \pi a^2 \cdot n_2 u_2 \\ \Longrightarrow \quad & n_2 = (2a/3L) n_1 \sim 10^{23}\ \mathrm{m}^{-3} \qquad (2.7) \\ & (P_2 \approx (2a/3L) P_1 \sim 0.1\ \mathrm{torr}). \end{aligned}$$

The gas expands freely after leaving the orifice so the density n will decrease as $n \sim 1/z^2$, where z is the axial distance from the orifice:

$$n(z) \sim n_2 \times (a/z)^2 \quad \sim 10^{19}\ \mathrm{m}^{-3} \text{ at } z = 100\ \mathrm{mm}. \qquad (2.8)$$

The plasma density measured at the same location 5–10 μsec after breakdown is $\sim 10^{22-23}$ m^{-3}, showing that the measured density is not a result of ionization of the neutral gas cloud but due to an active pumping of plasma particles from the source region. The MHD pumping mechanism described in section 1.4 drives plasma particles out of the orifice.

2.4 Main timing – gas breakdown sequence

The main timing system triggers various power supplies for the stuffing flux coil, the fast gas valves, and the HV gun bank. The timing system is optically isolated from the power supplies to break ground loops [17] as well as to protect it from accidental electrical shocks. All the power supplies are designed to be optically triggered. The timings are configured such that the HV gun bank is switched at the maximum of the bias poloidal flux and the optimal density (i.e., Paschen minimum) of the gas cloud. Referenced to the HV gun bank trigger timing (0 μsec), the stuffing flux coil is energized at -10 msec and then the fast gas valves are triggered at between -6 and -1 msec depending on the injected gas species. An example configuration of timings is illustrated in figure 2.5.

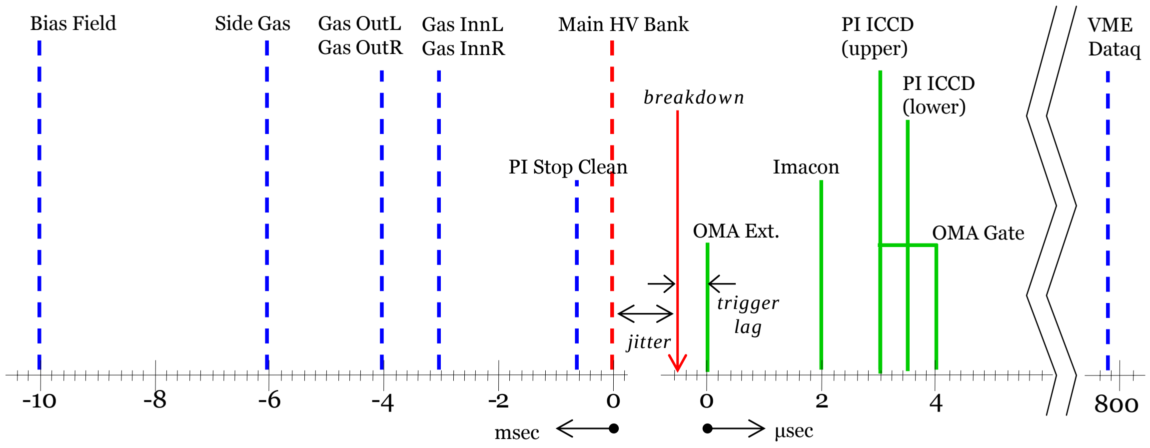

Figure 2.5: An example of timing configuration. The main timing system controls trigger pulses indicated by dashed lines (left to the main HV bank, except the VME data acquisition) in msec time scale. The breakdown jitter is 0–10 μsec. The diagnostic timing system controls trigger pulses indicated by solid lines (right to the main HV bank) in μsec time scale. The trigger lag is about 0.45 μsec (see section 3.5). The legends are self-explanatory except PI ICCD – triggers Princeton Instruments ICCD camera, PI Stop Clean – stops the continuous flushing of the PI ICCD pixels, OMA Ext. – triggers the timing module of the Andor ICCD detector of the spectroscopic system, and OMA Gate – gates the Andor ICCD.

The timings are uploaded into an 8-channel delay generator (Berkeley Nucleonics, Model 565) using a LabView program. The delay generator initiates generation of output pulses upon an external trigger. The output pulses are fed into a home-built 8-channel electro-optical pulse doubler (built by D. Felt). The pulse doubler generates two optical trigger signals, one at the rising edge and the other at the falling edge of each delay generator pulse, making total of 16 optical trigger signals.

The gas breaks down within 10 μsec but at random after a high voltage is applied across the electrodes. This randomness or jitter of the breakdown timing is greater than the time scale of plasma evolution ($\sim$1 μsec), so the HV gun bank timing cannot be used to synchronize diagnostics. A separate timing scheme for diagnostics has been developed to trigger diagnostics at the actual gas breakdown. The diagnostic timing system is described in section 3.5.

2.5 Plasma formation

A distinctive plasma structure forms as the gas breaks down by triggering the stuffing flux system, the gas injection system, and the HV gun bank in sequence as described in the previous section. Figure 2.6 illustrates a typical profile of gas cloud and bias field at the instant of the breakdown. The initial plasma structure is defined by eight flux tubes indicated by red solid field lines in the figure. Each flux tube spans a gas orifice on the cathode and the corresponding orifice on the anode. The breakdown condition is optimal along the flux tubes where gas density is highest. The ionized gas particles are pumped into the flux tubes from the source gas orifices by MHD force, forming a distinctive structure reminiscent of spider legs as shown in figure 2.7. The eight plasma-filled current-carrying flux tubes will be referred to as spider legs. Subsequent evolution of the spider legs is characterized by MHD force and will be discussed in chapter 4.

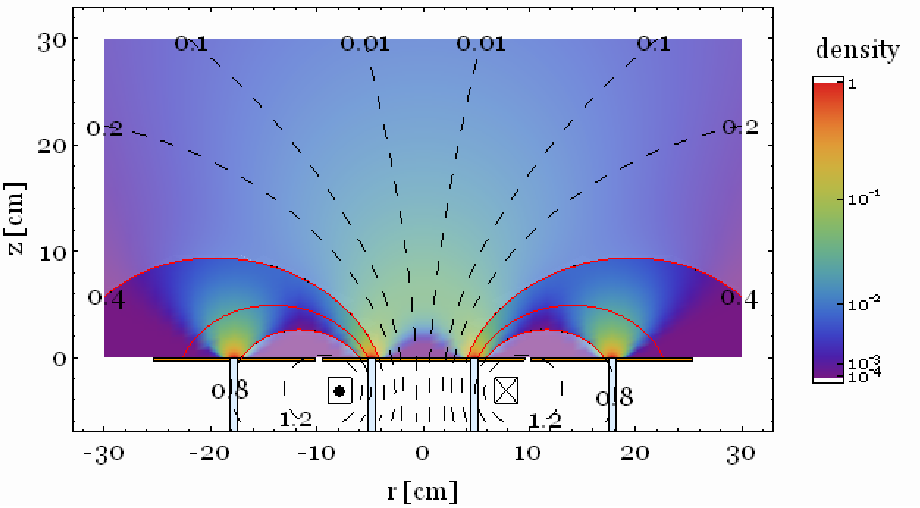

Figure 2.6: Neutral gas density profile and bias field lines (dashed lines) at the gas breakdown. Each field line is labeled by the amount of the poloidal flux (in mWb) enclosed by the circle whose radius is from the axis of symmetry to the field line. Colors represent the normalized density in a logarithmic scale as shown in the scale bar. Red solid lines define the flux tubes where inside the gas will break down. The density profile in the flux tubes are highlighted.

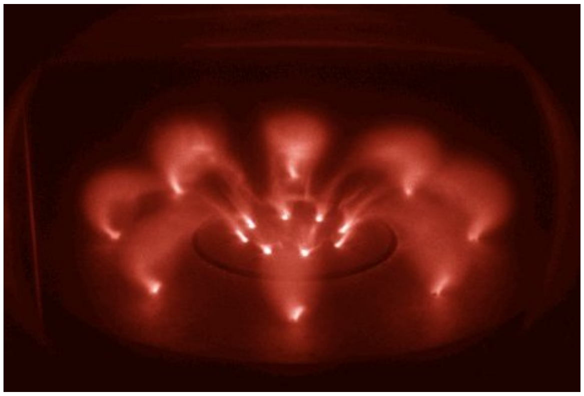

Figure 2.7: Eight plasma-filled current-carrying flux tubes (shot# 6529: N_2 inner + Ne outer). This distinctive plasma structure reminiscent of spider legs is formed by breaking down the gas cloud shown in figure 2.6.

Chapter 3

Diagnostics

The spheromak experiment has a set of diagnostics to measure plasma properties such as current, magnetic field, density, flow velocity, and geometry of plasma structures. Each diagnostic corresponds to an observable quantity of the plasma. An observable quantity may be a result of complex underlying physics and can give a valuable information about the plasma once the underlying physics is known. For example, electron density can be obtained if the Stark broadening of spectral lines due to charged particles is understood (ref. chapter 5).

Plasma properties are time-varying on the scale of μsec, and so every diagnostic must be recorded and synchronized to each other within an uncertainty much less than this plasma time scale.

3.1 VME digitizer system

Many diagnostic signals are recorded by a multichannel fast digitizer system and such signals are automatically synchronized with each other. The digitizer system comprises twelve data acquisition (DAQ) boards (SiS GmbH SIS3300; 8-channel 100 MHz 12-bit, 50 Ω input impedance, 256K samples/channel memory) and one counter board (SIS3820; 32-channel 50 MHz) installed on a VME crate. Initiated by an IDL computer code, each DAQ board continuously samples until it receives a stop signal from the counter board. The counter board is triggered by the main timing system (ref. section 2.4), typically somewhere between 0.5 and 2 msec after the HV gun bank discharge. The IDL computer code retrieves the sampled data from the DAQ boards later on.

The VME digitizer system records the voltage and current traces of the plasma gun, magnetic probe signals, etc. There are diagnostic data not recorded by the VME system such as camera images and spectroscopic signals. Those diagnostics are synchronized with the VME-recorded data by a timing scheme described in section 3.5.

3.2 High-voltage probe

The plasma gun voltage (V_{gun}) is measured by a 1000:1 high-voltage probe (Tektronix P6015; 20 kV Max, 75 MHz). The V_{gun} signal goes through a line driver to match the VME system's 50 Ω input impedance. A typical V_{gun} trace is characterized by four distinctive stages (figure 3.1a): (1) constant V_{gun} held at the applied voltage for less than 1 μsec up to 10 μsec before gas breakdown. (2) sudden voltage drop at the moment of gas breakdown. (3) a plateau at about half the applied gun voltage. The plateau is sustained as long as the plasma carries the gun current. (4) sinusoidal decay phase as the plasma is detached from the electrodes and the gun current flows through dump resistors.

The duration of the first stage is purely random and so the delay of gas breakdown cannot be controlled precisely, making it difficult to synchronize diagnostic signals (see also discussions in section 2.4 and section 3.5). The breakdown delay is longer for heavier gases in general.

3.3 High current transducer – Rogowski coil

The gun current is of the order of 100 kA and approximately sinusoidal (figure 3.1b). A home-made Rogowski coil is wrapped around the 7.5″ diameter re-entrant port of the plasma gun (figure 2.2b) to measure the time-varying gun current (dI_{gun}/dt). The Rogowski coil signal is integrated by a passive integrator circuit (figure 3.2). The current I_{gun} measured by the Rogowski coil is calibrated using a current monitor as

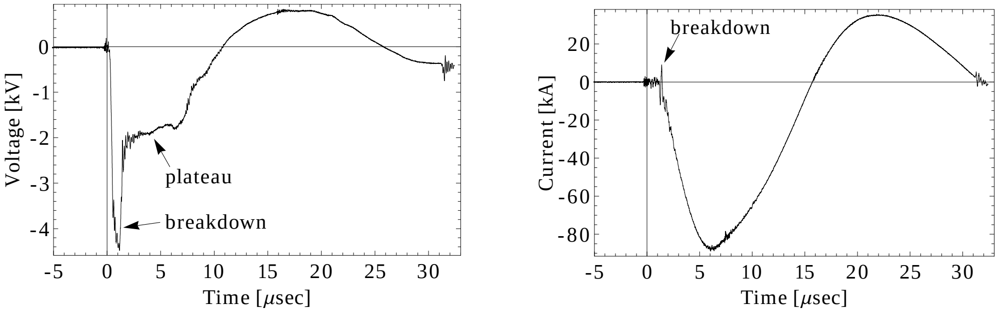

(a) Voltage trace (b) Current trace

Figure 3.1: Typical voltage and current traces of the plasma gun (shot# 7220: N_2 70 psi, $V_{\text{gun}} = 5$ kV).

explained in figure 3.3.

3.4 Multichannel magnetic probe

A 20-unit magnetic probe array constructed by Romero-Talamás [18] has been used to investigate the magnetic field structure of the plasma. Each unit is a cluster of three mutually orthogonal miniature commercial chip inductors. The probe array measures three-dimensional magnetic field at twenty locations, 20 mm apart. It is mounted on a right-angle arm so that both its axial and radial locations can be adjusted as shown in figure 2.2a. A measured magnetic field structure is shown in figure 3.4a. A method known as Single Shot Propagation Inference method [19] can be used to obtain a qualitative picture of the spatial configuration ($B(r, z)$) of magnetic field from a single magnetic probe measurement ($B(r, t)$). The method assumes that the magnetic field structure embedded in the plasma merely translates along the axial (z) direction:

$$B(r, z, t) = B(r, z_{\text{probe}}, t - (z - z_{\text{probe}})/v), \tag{3.1}$$

where z_{probe} is the location of the probe and v is the translation velocity. A plasma image is overlaid with the corresponding magnetic field structure drawn by this method in figure 3.4b.

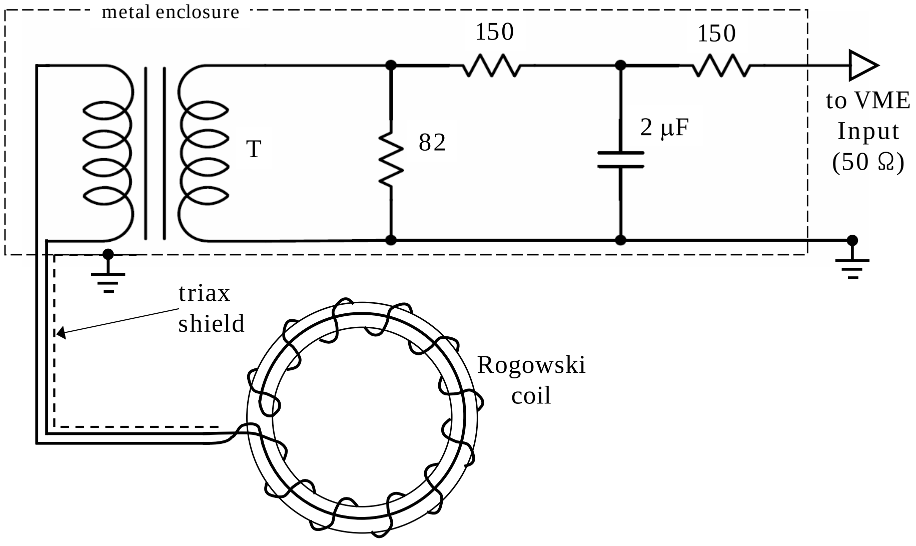

Figure 3.2: Passive integrator circuit for Rogowski coil (designed by P. M. Bellan). The effective resistance of the circuit is $R_{\text{eff}} = 150||(150 + 50) \approx 86\ \Omega$, giving the RC time constant of $86 \cdot 2 \times 10^{-6}$ sec = 170 μsec. The Rogowski coil is made of 72 turns of a semi-rigid coax cable (Micro-coax UT 85) with break in shield. The major diameter of the coil is 11.5″, the minor diameter is 0.375″, and the space between turns is 0.5″. The coil is isolated from the VME digitizer by a transformer. A triaxial cable connects the Rogowski coil to the integrator circuit. The outermost shield of the triaxial cable and the metal enclosure as a whole acts like a Faraday cage blocking electrical noises produced by the plasma gun.

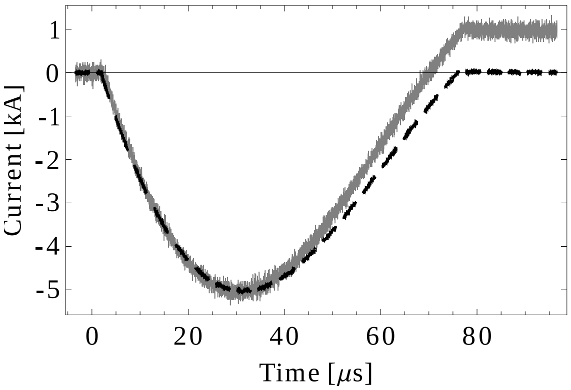

Figure 3.3: Rogowski coil calibration. The Rogowski coil was wrapped around a wire carrying a current pulse produced by discharging a capacitor. The wire was also passed through a current monitor (Ion Physics CM-01-L; 1 V/kA, saturation $\int I dt$ = 2 A·sec). Dashed line is the reference current measured by the current monitor. Solid gray line is the calibrated Rogowski coil signal. The calibrated signal correctly reproduces the reference signal for the first 40 μsec, but it drifts a little bit from the reference afterward.

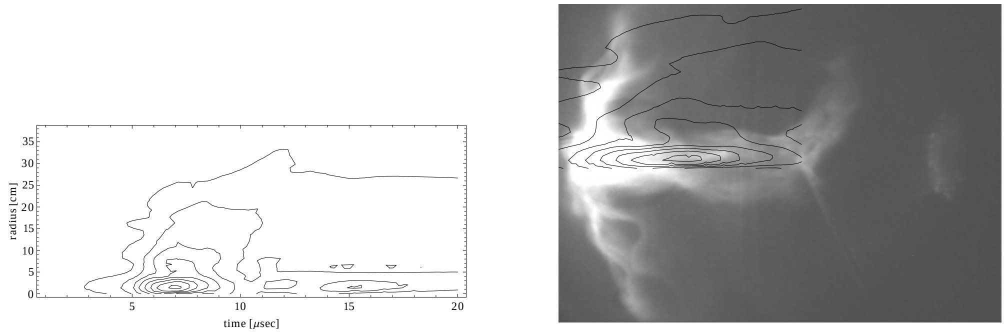

(a) Magnetic field structure

(b) Plasma overlaid with its magnetic field structure

Figure 3.4: Magnetic field structure measured by the magnetic probe array (shot# 7353; H_2 plasma). Contours of magnetic field energy density ($B^2/2\mu_0$) are shown.

3.5 Timing of diagnostics

A separate timing system similar to the main timing system (ref. section 2.4) has been developed in order to synchronize or trigger diagnostics with respect to the gas breakdown. The diagnostic timing system comprises an external trigger source, an 8-channel delay generator, and a pulse doubler. The external trigger source for generating a pulse at the instant of breakdown is necessary since the main timing system cannot provide such a pulse due to the breakdown jitter (ref. section 3.2). The delay generator is triggered by the external trigger and subsequently produces eight independent pulses with adjustable delay and pulse length. To prevent electrical shocks and ground loops, each delay generator pulse (except the OMA gate pulse; see figure 2.5) is fed into the pulse doubler instead of going directly to a diagnostic device through an electrical cable. Each optical pulse from the pulse doubler goes to a designated diagnostic device via an optical cable. The optical pulse is converted back to an electrical pulse by a small home-built battery-operated optoelectric transducer (OET; built by D. Felt) before entering the diagnostic device.

Two types of external trigger method have been developed and are described here.

(1) The abrupt change in V_{gun} trace as indicated in figure 3.1a corresponds to the instant of breakdown. A voltage comparator circuit was built to detect the abrupt voltage change and generate a subsequent trigger signal. The trigger

lags behind the breakdown by ~0.1 μsec due to the finite rise time of the voltage. However, a better method to detect breakdown had been sought since the voltage threshold of the comparator had to be re-adjusted for different settings of the gun voltage and the noise in the voltage signal near breakdown made false triggers occasionally.

(2) An optical method to detect the breakdown was motivated by the fact that the breakdown is always accompanied by substantial optical radiation from the resultant plasma, especially from inside the gas orifices. The emission light from one of the eight inner gas orifices is collected by a collimator lens focused on that orifice and fed into an optical fiber. The optical signal is converted to an electrical signal by an OET to trigger the delay generator. This optical scheme provides a reliable detection of breakdown free from the problems in the previous method with about the same trigger lag of ~0.15 μsec.

Although both of the methods are able to detect the breakdown within 0.15 μsec, the actual trigger pulses arriving at diagnostic devices are further lagged as much as 0.3 μsec due to the internal delays of the delay generator, the pulse doubler, OETs, and optical/electrical cables. The total trigger lag is 0.45 ± 0.05 μsec.

This trigger lag is taken into account when comparing the diagnostic data triggered by the diagnostic timing system (fast digital cameras, spectrometer, etc) with the VME-digitized signals ($V_{\text{gun}}, I_{\text{gun}}$, magnetic data, etc) which are not triggered by the diagnostic timing system. An example configuration of diagnostic timings (together with main timings) is illustrated in figure 2.5.

3.6 Fast digital cameras

The gun-produced plasma is rapidly evolving and highly radiative. Images of the plasma are taken by a multiframe high-speed intensified-CCD camera (DRS Hadland, Imacon 200; 10 bpp dynamic range, 1200 × 980 pixels, 6.7 μm square pixel). The Imacon camera can take up to 16 frames per shot. The exposure and delay of each frame can be configured in 5 nsec precision, a sufficient time resolution for capturing the μsec-scale plasma evolution. In a normal configuration, 16 frames are taken at an equally spaced time interval. Each frame can also be multiply exposed to capture multiple plasma images in the frame, for example to see the evolution of the plasma in finer time scale without reducing the total time span.

A system of dual single-frame CCD cameras (Princeton Instruments, ICCD-576-G/RB-E; 16 bpp dynamic range, 576×384 pixels, 22.5 μm square pixel) is sometimes used for sharper images (because of the better dynamic range). The exposure and delay of the Princeton ICCD cameras can be configured to a 10 nsec precision.

Optical filters can be put on the camera lenses to measure the plasma radiation within a specific optical bandpass. Filtered plasma images are used to identify particle species in plasmas made of multiple gas species.

3.7 Spectroscopic system

Shifts and broadenings of spectral lines emitted by plasma reflect the physical condition of the plasma such as density, temperature, and flow velocity. A low-resolution spectroscopic system (consisted of an optical fiber, a 0.22 m spectrometer, and an ICCD detector) was used to infer plasma conditions from spectral line profiles in a previous attempt by C. Yang [20]. Broadenings of H_α and H_β lines as large as 1.3 nm were observed and attributed to the Stark effect and the thermal Doppler effect. The Stark broadening is a density effect caused by local electric fields due to ions and electrons in the plasma and is summarized in chapter 5. The H_α line width was used to estimate the temperature assuming it is strictly Doppler broadened and the H_β line width subtracted by the H_α line width was used to estimate the density. This procedure would give a reasonable density in case of a large broadening much greater than the 0.2 nm instrumental broadening of the spectrometer since the Stark effect is about 5 times stronger for the H_β line than the H_α line. A peak density of the order 10^{22} m^{-3} was reported in the study.

The large broadening of the H_β line was routinely observed in later experiments by the present author using the same spectroscopic system. However, the spectral resolution of the spectrometer was not sufficient enough to estimate density less than 10^{21} m^{-3} nor to see any Doppler shift for flow velocity measurement. It was also difficult to estimate densities of non-hydrogen plasmas since Stark broadenings of non-hydrogenic lines are at least an order of magnitude smaller than hydrogen lines.

A multichannel high-resolution spectroscopic system has been constructed in order to improve the spectral resolution. The ability to measure spectra at multiple locations of the plasma with definite lines of sight has also been implemented into the new spectroscopic system since the plasma is inhomogeneous and its detail structure is not reproducible. The spectroscopic system, illustrated in figure 3.5, comprises a camera lens, a 12-channel fiber array, entrance optics, a high resolution spectrometer, and an intensified CCD detector. The camera lens forms an image of plasma on the plane of the fiber array input. The plasma emission is intercepted by the fiber array at 12 different locations and fed into the spectrometer. The emission spectra analyzed by the spectrometer are then recorded by the ICCD detector. The ICCD detector is triggered and gated by the diagnostic timing system as indicated by “OMA Ext.” and “OMA Gate” respectively in figure 2.5.

The specifications of the spectroscopic system are summarized below:

(1) The wavelength range is 200–500 nm, where the lower end is limited by the camera lens and the upper end by the spectrometer.

(2) The spectral resolution is calculated from the spectrometer and ICCD parameters according to

$$R(\lambda) = \frac{\Delta x}{2L}\left(\sqrt{\left(\frac{2d\cos\alpha_0}{m}\right)^2 - \lambda^2} + \lambda\tan\alpha_0\right), \tag{3.2}$$

where $R(\lambda)$ is the pixel resolution (wavelength per pixel), Δx is the ICCD pixel size, L is the focal length of the spectrometer, α_0 is half the angle between the incident and the diffracted light on the grating, d is the groove spacing of the grating, m is the diffraction order, and λ is the selected wavelength.

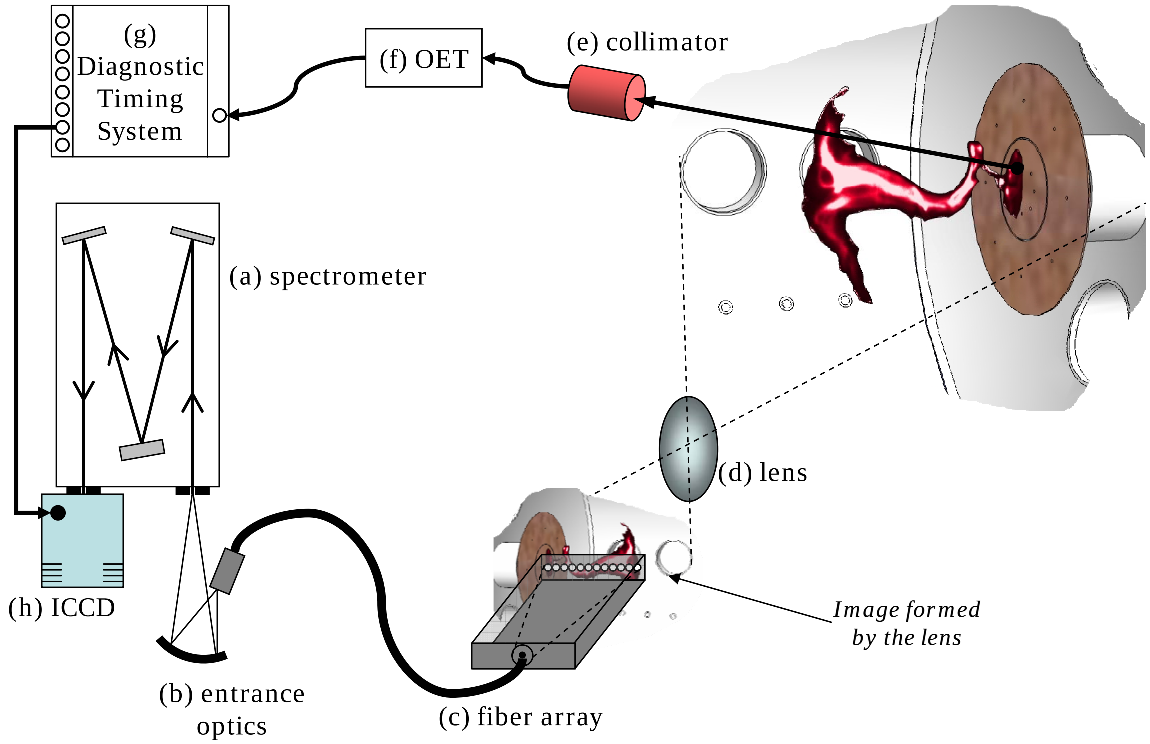

Figure 3.5: Schematic drawing of the spectroscopic system. The system consists of (a) Czerny-Turner spectrometer (JY Horiba 1000M: 1 meter focal length, f/8 aperture, 3600 grooves/mm grating), (b) F/# matching entrance optics (c) 12-channel linear fiber assembly (RoMack custom design; UV/VIS grade, 0.22 NA, 100 μm core size, 10 meters long) (d) camera lens (e) collimator (Fiberguide MACRO collimator; 22.2 mm aperture, 0.22 NA), (f) optoelectric transducer (OET), (g) diagnostic timing system, and (h) intensified CCD detector (Andor ICCD DH520-25F-03; 16 bpp dynamic range, 800 × 256 active pixels, 26 μm square pixel).

The derivation of equation (3.2) is given in appendix C. The accuracy of this calculation has been verified over a wide range of reference wavelengths using spectrum tubes (Hg, D_2, O_2, and Ar).

(3) The temporal resolution, i.e., minimum gate width of the ICCD detector with reasonable signal-to-noise ratio, is about 0.3 μsec. The temporal resolution is mainly limited by optical throughput, which is maximized by matching f-numbers between optical components.

(4) The spatial resolution is determined by the fiber diameter and the magnification of the imaging optics. Each fiber in the fiber array intercepts a line of sight volume of diameter ~3–5 mm. The interspace between the lines of sight is approximately 10 times the line of sight diameter, which is ~30–50 mm, when the focal length of the camera lens (d) in figure 3.5 is 50 mm. The spatial resolution is also affected by the temporal resolution because the plasma jets move very fast. For example, if the ICCD gate width is 1 μsec and the jet velocity is 30 km/sec, the detector signal is integrated over the jet travel distance of 30 mm.

(5) Twelve spectra corresponding to twelve different locations of the plasma are simultaneously recorded per shot. The 256 rows of the ICCD are divided into 12 tracks. The plasma emission light delivered by each fiber is spread onto the corresponding track of the ICCD by the spectrometer.

The knowledge of spectral resolution is required to measure spectral line widths and shifts. The spectral resolution, bandpass (pixel resolution × number of pixels), and the Doppler shift corresponding to one pixel shift are calculated for the entire wavelength range using equation 3.2 and are shown in figures 3.6.

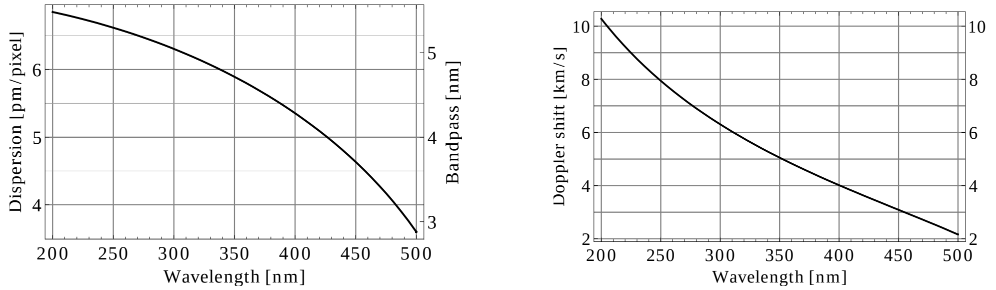

(a) Pixel resolution

(b) Doppler shift per pixel

Figure 3.6: (a) Pixel resolution and bandpass of the spectroscopic system and (b) Doppler shift corresponding to one pixel shift, as a function of the selected wavelength λ.

3.7.1 Entrance optics

The cone angle over which an optical component can accept or emit light is specified by either f-number (F/#) or numerical aperture (NA) defined as

$$\mathrm{F}/\# = f/D, \tag{3.3}$$

$$\mathrm{NA} = n\sin(\theta), \tag{3.4}$$

where f is the focal length, D is the aperture diameter, n is the index of refraction, and θ is half the cone angle. The optical throughput, i.e., the fraction of light which will pass through, from an optical component with a half-cone angle θ_1 ($\mathrm{F}/\#_1$) to another optical component with a smaller half-cone angle θ_2 (a larger $\mathrm{F}/\#_2$) is given by

$$\text{throughput} = \left(\frac{\sin(\theta_2/2)}{\sin(\theta_1/2)}\right)^2 \approx \left(\frac{\mathrm{F}/\#_1}{\mathrm{F}/\#_2}\right)^2, \tag{3.5}$$

since the solid angle of a cone is $4\pi\sin^2(\theta/2)$. The approximation of the throughput by the square of the f-number ratio is accurate for small cone angles and is preferred for its convenience.

A typical multimode fiber has NA = 0.22 or F/# = F/2.3, corresponding to $\sin^{-1}(0.22) \approx 13$ degrees of half-cone angle. The spectrometer's f-number is F/8, corresponding to $\tan^{-1}(1/8/2) \approx 3.6$ degrees of half-cone angle. Because of this discrepancy in f-numbers, the spectrometer can accept only a tiny fraction $((2.3/8)^2 \approx$

8%) of the input light from the fiber array unless an appropriate f-number matching optics is employed. This is like trying to connect pipes with different diameters without a coupler.

A commercial f-number matcher (Oriel 77529) was used initially to increase the f-number of the fiber (or decrease the cone angle of the fiber) by a factor of 2 so that the optical throughput will increase by a factor of 4 (from 8% to 30%). However, it was abandoned immediately since the small mirror inside the f-number matcher was found to block a significant fraction of light. Instead, an elaborate entrance optics to the spectrometer has been constructed in order to maximize the optical throughput.

The entrance optics consists of a spherical mirror (diameter = $3''$, focal length = $3''$, protective aluminum coating), a y-z precision translation stage, and a linear (z) stage (y refers to the direction from the fiber to the mirror and z refers to the vertical direction). The fiber array mounted on the y-z stage and the mirror are raised up together to the level of the spectrometer's entrance slit by the linear stage. The position of the fiber array is further adjusted on a μm precision by the y-z stage so that the fiber output is focused onto the spectrometer's entrance slit by the mirror. This arrangement increases the fiber's f-number by a factor of 3, achieving a high optical throughput = $(3 \times 2.3/8)^2 \approx 75\%$. A mirror was favored over a lens configuration for better UV transmission. A UV-grade fused silica lens has a good UV transmittance but its index of refraction changes as a function of wavelength, making it difficult to focus the fiber output over a wide wavelength range. Mirrors do not suffer from this problem.

3.7.2 Fiber array

The 12-channel linear fiber array has been constructed to observe plasma emissions at 12 different spatial locations simultaneously. The individual fibers are 100 μm core diameter, UV/VIS grade fused silica fibers. The fibers are aligned in a single evenly spaced row, the interspace being 1 mm at the input end of the array and 150 μm at the output end.

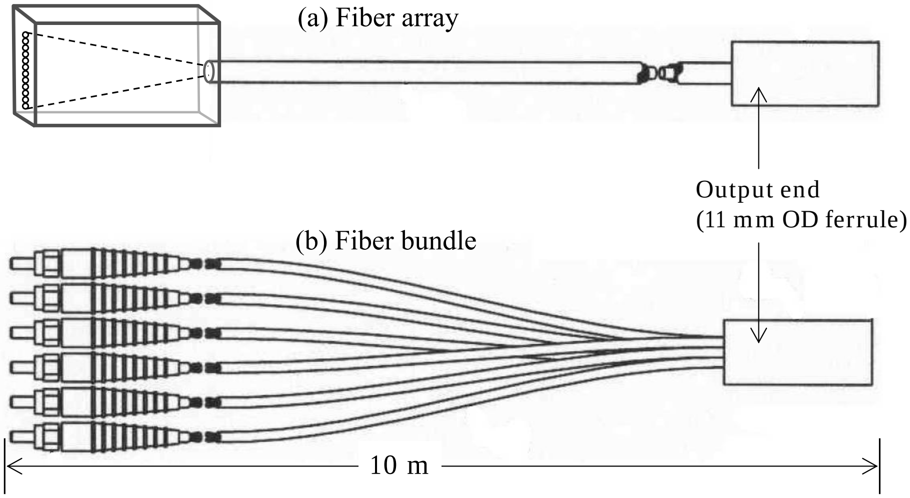

Figure 3.7: (a) Fiber array and (b) fiber bundle

The interspace between fibers at the input end was decided by the distance the plasma jet would travel on the image plane of the camera lens during a typical exposure time (∼1 μsec). The optimal interspace was found to be 1 mm by considering the following typical case: for 50 mm focal length and 1000 mm object distance (distance from the lens to the plasma), 1 mm on the image plane corresponds to ∼20 mm on the object plane, a distance that a plasma jet of 20 km/s velocity would traverse during 1 μsec. The interspace between fibers at the output end was decided for the best coupling to the spectrometer. Since the image of the fiber array is magnified by a factor of 3 due to the entrance optics, the 12 fiber images span a vertical distance $3 \times (11 \times 150)\ \mu\text{m} = 4.95$ mm at the spectrometer's exit plane. This vertical span fits all the 12 fiber images in the 6.7 mm height of the ICCD's active area.

In some experiments, a multitrack fiber bundle has been used instead of the linear fiber array. The multitrack fiber bundle consists of 9 independent fibers (200 μm core). The fibers are aligned only at the output end and are freely moving at the input end as shown in figure 3.7b. Several fibers are connected to collimators at the input end and are used to observe the plasma with multiple view angles as illustrated in figure 3.8b.

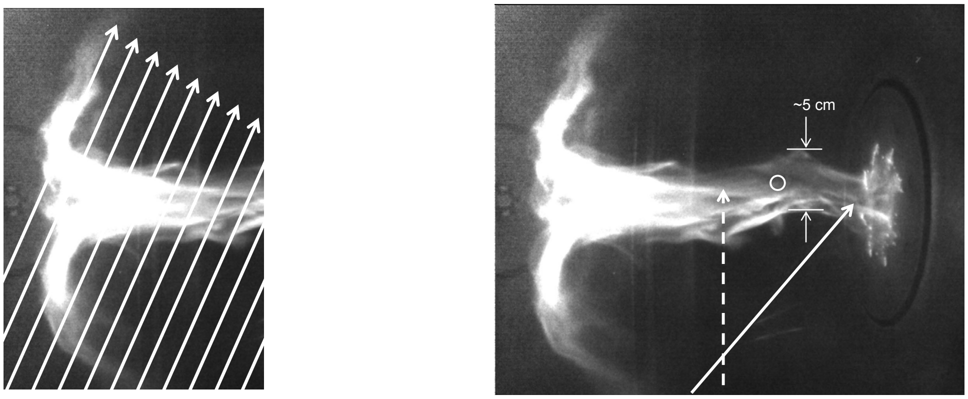

(a) Fiber

(b) Fiber bundle

Figure 3.8: (a) Lines of sight of the fiber array. The twelve lines of sight are approximately equally spaced. (b) Lines of sight of the multitrack fiber bundle. In this example, the dashed line is perpendicular to the axis of the plasma and the solid line is off-axis toward the electrode. The circle represents the size of the lines of sight (∼10 mm in diameter).

3.7.3 Visualizing lines of sight

The lines of sight of the spectroscopic system can be visualized by sending a HeNe laser beam backward through the fibers and observing the red spots this laser beam makes on the electrodes. A holographic light shaping diffuser is used to vertically elongate and distribute the single laser beam into all the fibers. Lines of sight are illustrated in figure 3.8a for the fiber array and figure 3.8b for the fiber bundle.

Chapter 4

Observations

4.1 Evolution of plasma structures

Following the gas breakdown sequence described in section 2.4, the plasma expands into vacuum undergoing several structural changes as shown in the Imacon camera image (figure 4.1). The evolution of the plasma has four distinctive stages: (I) formation and collimation of spider legs, (II) coalescing of spider legs into a central plasma jet, (III) expansion and collimation of plasma jet, and (IV) instability of plasma jet and spheromak formation. It is interesting to note that, in contrast with the substantial structural changes of the plasma, the current and voltage traces are almost featureless as shown in figure 4.2.

The first two frames of the camera image show the plasma-filled arch-shaped flux tubes formed in a structure reminiscent of spider legs. The spider legs are initially flared but become collimated within a very fast time scale less than 0.5 μsec. The spider legs stretch out by the hoop force due to the gun current flowing through them. The flux tube collimation process has been studied in detail by You, Yun, and Bellan [21].

In the second stage (frames 3–6 in the camera image), the collimated spider legs become diffusive and start moving toward the center as the gun current ramps up. The spider legs attract each other since each carries an electric current in the same direction. They eventually coalesce into a single axially expanding plasma jet.

In the third stage (frames 7–10), the central plasma jet becomes collimated and expands into the vacuum. The jet velocity is Alfvénic (∼30 km/sec). The plasma jet is very bright compared to the spider legs suggesting a jet density much greater than the spider leg density. Large density amplification has been observed in the plasma jet and will be discussed in section 4.3.

In the last stage (frames 11–16), the lengthened plasma jet may keep expanding or undergo MHD instability depending on the ratio $\lambda_{\text{gun}} = \mu_0 I_{\text{gun}}/\psi_{\text{gun}}$, where I_{gun} is the gun current and ψ_{gun} is the initial bias poloidal magnetic flux. Hsu and Bellan [9] showed that low λ_{gun} values result in a straight plasma jet, intermediate values lead to kinking of the jet axis (kink instability), and high values lead to a detachment of the plasma from the electrodes. The kinking has been identified as a precursor to spheromak formation.

The present thesis work is focused on the study of the plasma evolution at the first and the third stages.

4.2 Magnetic flux tube collimation – spider legs

4.2.1 Main observations

The spider leg magnetic flux tubes are initially very faint and flared, i.e., the tube diameter increases toward the outer electrode. However, the spider legs become collimated and brighter as more particles are ingested from the gas orifices as shown in figure 4.3.

S. You [21] visualized the plasma flow in the spider legs using the high-speed high-resolution Princeton camera. Since hydrogen spider legs are less collimated than spider legs of heavier gas species, N_2 and Ne were used in the study. He observed that the plasma particles are ingested mainly from the inner gas orifice and the direction of the flow is from the inner orifice toward the outer orifice. The flow velocity is of the order of ∼100 km/sec, measured by tracing a bright front propagating along the flux tube axis in the camera images.

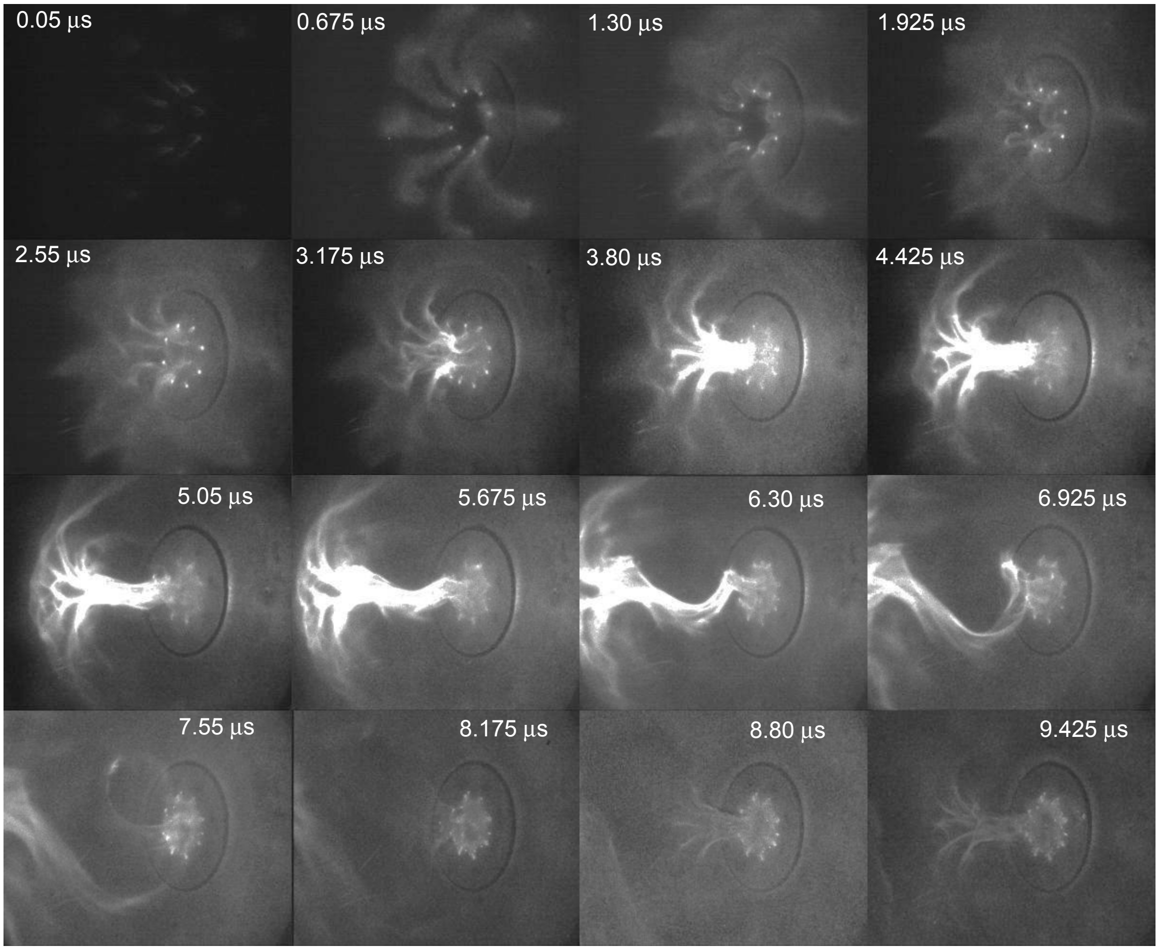

Figure 4.1: Evolving plasma structure (shot# 7217, hydrogen plasma). The frame sequence is from left to right and top to bottom. The delay of the first frame is 0.05 μsec with respect to breakdown and the inter-frame delay is 0.625 μsec. In the last few frames, notice the presence of ghosting from previous frames.

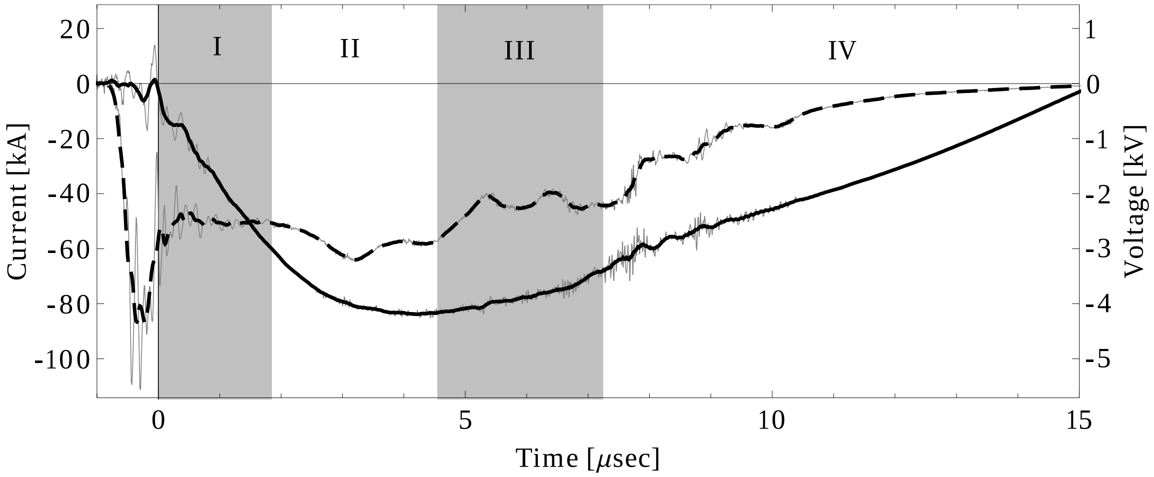

Figure 4.2: Gun current trace (solid curve) and voltage trace (dashed curve). Data correspond to the same plasma discharge (shot# 7217) as in figure 4.1. Times are with respect to breakdown. Roman numerals indicate the evolution stages.

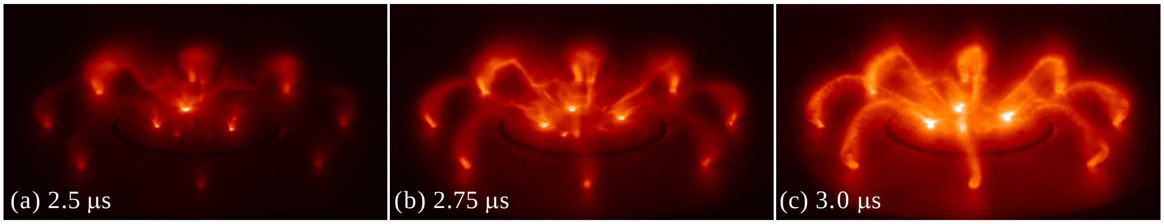

Figure 4.3: Collimation of spider legs (image courtesy of S. You). Images are taken from identical plasma discharges (shot# (a) 4345, (b) 4346, and (c) 4343). Nitrogen is injected from the inner (cathode) orifices and neon from the outer (anode) orifices. Times correspond to the delay of the 10 nsec camera exposure with respect to the main bank discharge.

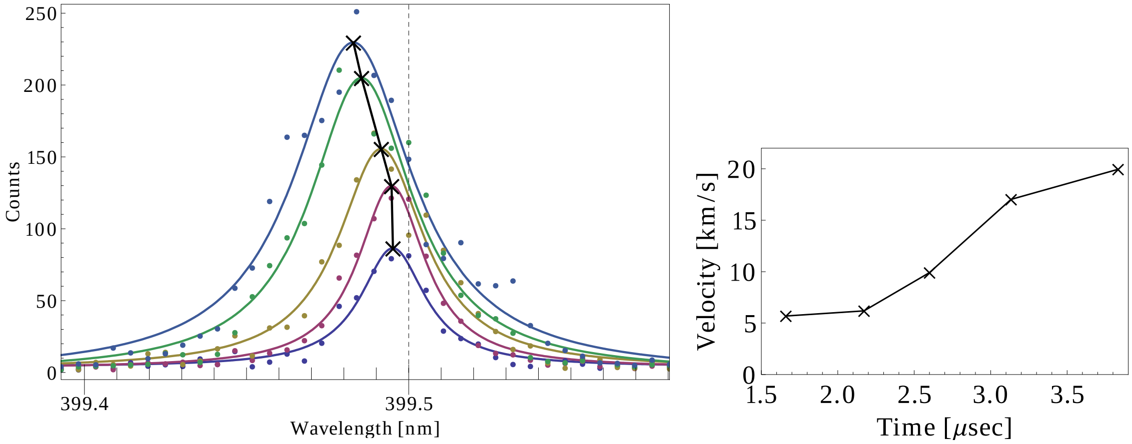

(a) Doppler shifts

(b) Doppler velocity

Figure 4.4: (a) N_{II} spectra showing blue Doppler shifts (nitrogen discharge; shot range 6811–6830; spectrometer ICCD exposure = 1 μsec). Dashed line indicates the rest frame wavelength 399.5 nm. Solid lines are Lorentzian curve fits. The exposure delays of the spectra, starting from the bottom to the top spectrum, are 1.7, 2.2, 2.6, 3.1, and 3.8 μsec, respectively, with respect to breakdown. The peaks of the spectra are connected to show the trend of increasing blue shifts. The line of sight intercepted one of the spider legs near its inner foot point perpendicular to the electrode. (b) Line of sight velocities estimated from the Doppler shift measurements.

4.2.2 Doppler shift measurements

To verify that the propagation of the bright front is indeed a plasma flow and not an ionization front, the Doppler shifts of emission spectra from a single spider leg were measured by the present author [21] using the spectroscopic system with the multitrack fiber bundle (section 3.7.2). The measured spectra showed blue shifts corresponding to ∼20 km/sec line of sight velocities as shown in figures 4.4a and 4.4b. The blue Doppler shifts confirm that the propagation of the bright front is indeed the flow of plasma ions.

4.2.3 Flow velocity profile along the spider leg

Flow velocities $U(z)$ along the spider leg axis can be expressed in terms of the plasma density $n(z)$ assuming that the length of the spider leg (L) remains constant during measurement and the flow stagnates at the outer orifice ($U(L) = 0$). These assumptions seem reasonable based on the camera images (figure 4.3). Integrating the continuity equation yields

$$\begin{aligned}\int_z^L \left[\frac{\partial}{\partial z}\left(n(z')U(z')\right) + \frac{\partial n(z')}{\partial t}\right] dz' = 0,\\ n(L)U(L) - n(z)U(z) + \frac{\partial}{\partial t}\int_z^L n(z')dz' = 0,\\ U(z) = \frac{1}{n(z)}\frac{\partial}{\partial t}\int_z^L n(z')dz' \qquad (\because U(L) = 0 \text{ by assumption}),\end{aligned} \tag{4.1}$$

where z is the axial distance from the inner orifice.

Since line radiation in plasma results primarily from collisional excitations due to electron impact, the radiation intensity I will be proportional to the electron density (n_e) times the emitter density (n_{emitter}). Assuming that the emitter density is some constant fraction of the ion density (n_i) and invoking charge neutrality ($n_i = n_e$) yield

$$I \propto n_e n_{\mathrm{emitter}} \propto n_e n_i \propto n_e^2. \tag{4.2}$$

Thus, the flow velocity $U(z)$ can be estimated using the image brightness $I(z)$ as

$$U(z) = \frac{1}{\sqrt{I(z)}}\frac{\partial}{\partial t}\int_z^L \sqrt{I(z')}dz'. \tag{4.3}$$

The estimated velocities are shown in figure 4.5b and are consistent with the propagation velocity of the bright front.

4.2.4 Discussion

The direction of the flow is counter-intuitive since one would normally think that ions would move toward the cathode (inner electrode) not away from it. However, this intuitive notion is incorrect because the the static electric field vanishes inside the plasma. According to the MHD pumping model (section 1.4), the plasma (ion) flow in a magnetic flux tube is driven by the MHD force (equation (1.31)),

$$mn\frac{dU}{dt} = \frac{\mu_0 I^2}{2\pi^2 a^3}\frac{\partial a}{\partial z}, \tag{4.4}$$

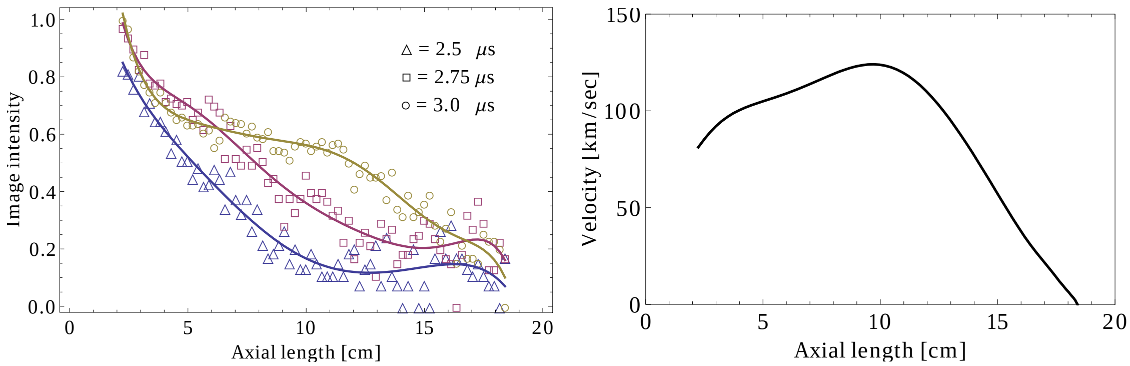

(a) Brightness

(b) Flow velocity

Figure 4.5: (a) Brightness along the spider leg that is shown in figures 4.3a–c (data courtesy of S. You). Triangle, square, and circle correspond to the timings 2.5, 2.75, and 3.0 μsec, respectively. Data points at $z < 2$ cm are excluded due to a relatively large measurement error. (b) Flow velocity profile at 2.75 μsec obtained from equation (4.3).

where m is the ion mass, a is the local flux tube radius, and $\partial a/\partial z$ is the flaring of the flux tube. For the spider legs, $\partial a/\partial z > 0$ and so an axial flow from the inner cathode orifice to the outer anode orifice will be driven by this MHD force. The spider legs become collimated due to the flow stagnation at the anode orifice as explained by the MHD pumping model in section 1.4.

S. You estimated a spider leg density $n \sim 2 \times 10^{21}$ m^{-3} using $a \sim 4$ mm, $\partial a/\partial z \sim 0.02$, and $dU/dt \sim 10^{11}$ m/sec^2 measured from the camera images and assuming that a single leg carries one-eighth of the total gun current 120 kA (that is, $I = 120/8 = 15$ kA). Since the formation and collimation of the spider legs take place within 0.5 μsec, the pumping speed of the MHD force through a single gas orifice is

$$\left(\frac{dN_1}{dt}\right)_{\mathrm{MHD}} \sim \frac{\Delta n \cdot V}{\Delta t} \sim \frac{2 \times 10^{21} \times 10^{-5}}{0.5} = 4 \times 10^{16} \text{ particles}/\mu\text{sec}, \tag{4.5}$$

where $V \sim 10^{-5}$ m^3 is the volume of a single spider leg. This MHD pumping speed is much faster than the measured particle flux rate for a single gas line by gas puffing, $dN_1/dt \sim 2 \times 10^{15}$ μsec^{-1} (equation (2.4)). Thus, the ionized particles are dominantly ingested by the MHD force.

The Alfvén velocity U_A associated with the azimuthal magnetic field due to the spider leg current I is

$$U_A = \sqrt{\frac{B_\phi^2}{\mu_0 n m}} \sim 100 \quad \text{km/sec}, \tag{4.6}$$

where $B_\phi \sim \mu_0 I/2\pi a \sim 1$ Tesla and m is the mass of the nitrogen atom. Thus, the measured jet velocity (∼100 km/sec) is Alfvénic as expected by the model and is driven by the MHD pumping force. In the hydrogen spider legs, the flow velocity ($\gtrsim$ 100 km/sec) is faster due to the smaller ion mass and the density ($\lesssim 10^{21}$ m^{-3}) is lower due to less collimation.

4.3 Large density amplification in the plasma jets

4.3.1 Large Stark broadening of hydrogen spectral lines

After the spider legs coalesce into a central plasma jet, the jet expands axially with its foot point attached to the inner electrode (cathode) until the jet undergoes instabilities at a later time. Jet velocities of ∼20–50 km/sec were measured by following the forefront of the jet in the camera images. To rule out the possibility that these camera images would result from propagation of either a plasma wave or an ionization front rather than an actual flow, Doppler shifts of spectral lines emitted from the plasma jet were measured [22] using the spectroscopic system with the multitrack fiber bundle. The observed Doppler shifts (figure 4.6) confirmed the flow velocity deduced from the camera images.

However, some spectral lines showed unexpectedly large broadening which greatly exceeds the instrumental broadening and the thermal Doppler effect for a credible ion temperature [22] (see the discussion of section 6.1.2). For instance, some measured H_β line profiles showed a full width at half maximum (FWHM) $\gtrsim$ 1 nm, which would correspond to a Doppler ion temperature $\gtrsim$ 1000 eV. Such large broadenings suggest a strong Stark effect as discussed in section 6.1.2. The characteristic central dip observed in some H_β line profiles as shown in figure 4.7 is also an indisputable evidence for a strong Stark effect (ref. chapter 5 and [23]).

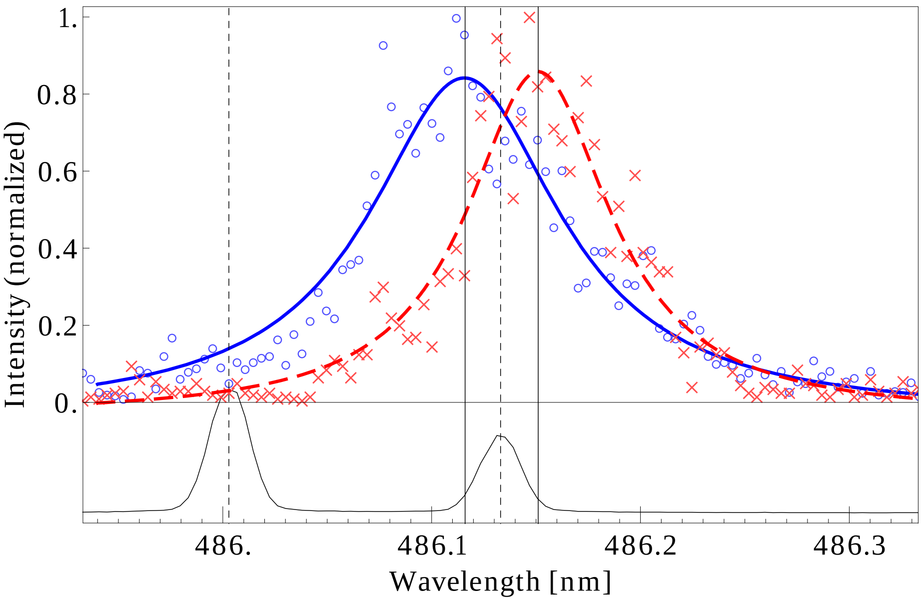

Figure 4.6: Doppler shifts of H_β lines (spectrometer ICCD exposure = 1 μsec). Line of sight was arranged such that the plasma jet moved toward the optical probe in one case (solid blue curve; shot# oma11.12) and away from it in the other case (dashed red curve; shot# oma11.43). The peak of the line profile is determined by Lorentzian curve fitting. As expected, a blue shift is observed in the first case and a red shift in the latter case. The shifts are ∼0.017 nm corresponding to ∼11 km/sec line of sight velocity. Rest-frame H_β (486.133 nm) and D_β (486.0029 nm) lines from a deuterium lamp are shown at the bottom.

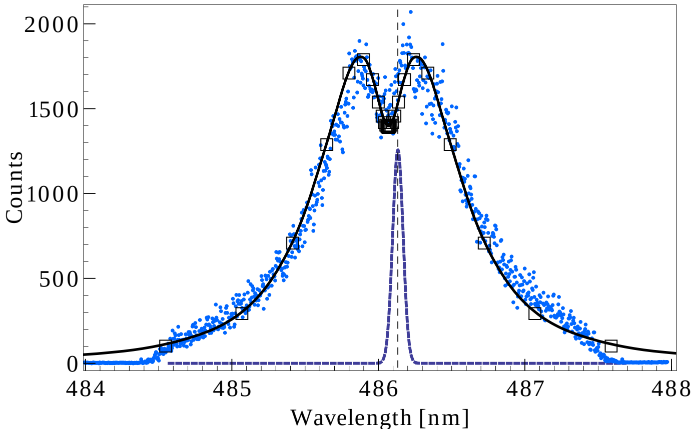

Figure 4.7: H_β profile showing the characteristic central dip (shot# oma11.28; spectrometer ICCD exposure = 1 μsec). The square points are the theoretical Stark profile for $n_e = 1.3 \times 10^{22}$ m^{-3} and $T = 2$ eV according to Stehlé [24]. A Doppler profile (dashed line) for $T_i = 5$ eV at the H_β rest-frame wavelength (486.133 nm) is also shown for comparison with the much broader Stark profile. The estimated Stark FWHM according to equation (6.2) is ∼1.1 nm, corresponding to $n_e \sim 1.2 \times 10^{22}$ m^{-3}. Note that the data points near the profile tail ends are flat since they are outside the bandpass of the spectroscopic system.

4.3.2 Density measurements

Electron densities were measured from the Stark broadened spectral lines by the method described in section 6.2. The time dependence of the electron density of a hydrogen plasma jet is plotted in figure 4.8. Peak density of the order 10^{22} m^{-3} is observed when the spider legs merge completely. The density is $\sim 10^{20}$ m^{-3} when the plasma starts to form the central jet and increases by a factor of 100 when the jet fully forms. Merging of the spider legs does not decrease the total volume of the plasma and thus cannot account for this large density amplification. On the other hand, the observed density amplification is consistent with the magnetic flux tube becoming filled with plasma by the ingestion/collimation process described in the MHD pumping model.

Similar density amplification is observed in non-hydrogen plasmas. For nitrogen plasma jets, Stark broadened N_{II} spectral lines are used for density estimation and a typical emission spectrum is shown in figure 4.9. Nitrogen plasma jets show even greater peak density of $\sim 1 \times 10^{23}$ m^{-3} (see figure 4.10).

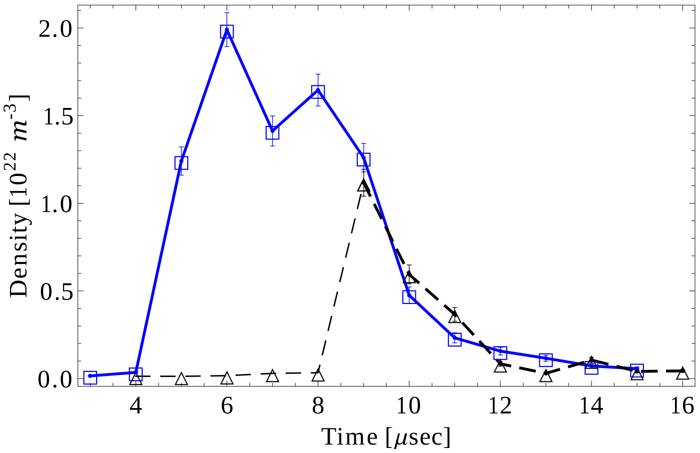

Figure 4.8: Electron density of a hydrogen plasma jet vs. time (shot range: oma11.16–69). Density is estimated from the H_β line profiles. Squares correspond to the solid (oblique) line of sight and triangles to the dashed (perpendicular) line of sight in figure 3.8b. For the perpendicular line of sight, the density is zero initially and appears suddenly at $t = 9$ μsec as expected because the jet takes time to reach the line of sight volume. This is consistent with the measured jet velocity (~30 km/sec).

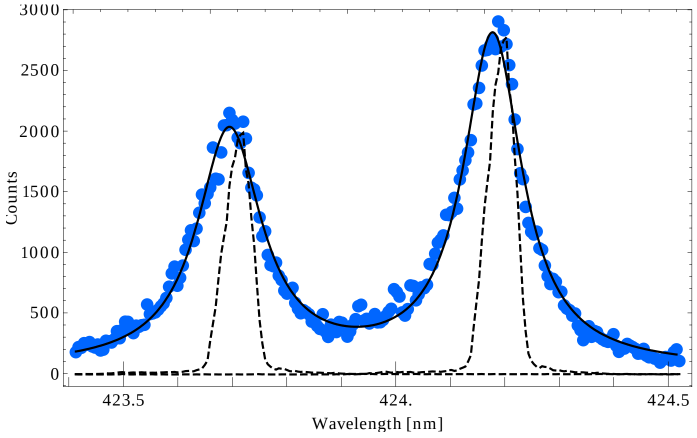

Figure 4.9: Stark broadened N_{II} spectral lines from a nitrogen plasma jet (shot# 7245; spectrometer ICCD exposure = 0.1 μsec). The rest-frame wavelengths of the two spectral lines are 423.705 nm and 424.178 nm, respectively. Instrumental function (dashed line) is shown at the two rest-frame wavelengths for width comparison. Solid line is a Lorentzian curve fit to the spectrum. Estimated density is $\sim 8 \times 10^{22}$ m^{-3}.

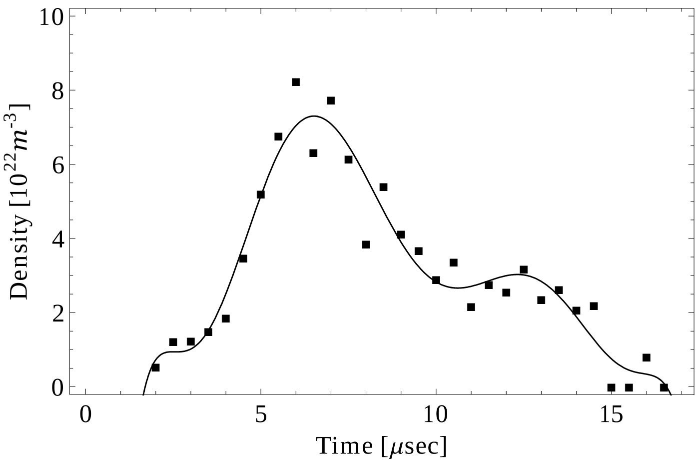

Figure 4.10: Electron density of a straight column nitrogen plasma jet vs. time (shot range: 6736.01–30). Density is estimated from the N_{II} 424.178 nm line profiles as illustrated in figure 4.9. Solid curve is a polynomial fit to the data.

4.3.3 Density and velocity profile along the jet axis

Density profiles along the axis of a straight nitrogen plasma jet were measured at several different timings using the spectroscopic system with the fiber array. The axial density profile has a sharp peak initially but becomes uniform as the jet expands axially as can be seen in figure 4.11a.

Velocity profiles were measured from the Doppler shifts of the same spectra used in the density measurement and are shown in figure 4.11b. The velocity peak is always ahead of the density peak by 3–5 cm in space and by ∼1 μsec in time. Negative velocity gradient (i.e., slowing down of the flow) is clearly seen near the jet front.

A detailed comparison with the camera images (figure 4.13) shows that the bright blob in the jet coincides with the region between the density peak and the velocity peak. The blob propagates along the jet axis with an Alfvénic velocity of ∼40 km/sec. The blob is faster than the expanding outskirts of the jet and catches up with it later as seen in the last frame of figure 4.13. This observation is consistent with the negative velocity gradient near the jet front.

For the detailed analysis in the next section, three density profiles are selected from figure 4.11a and shown overlaid in figure 4.12a. The corresponding velocity profiles are shown overlaid in figure 4.12b.

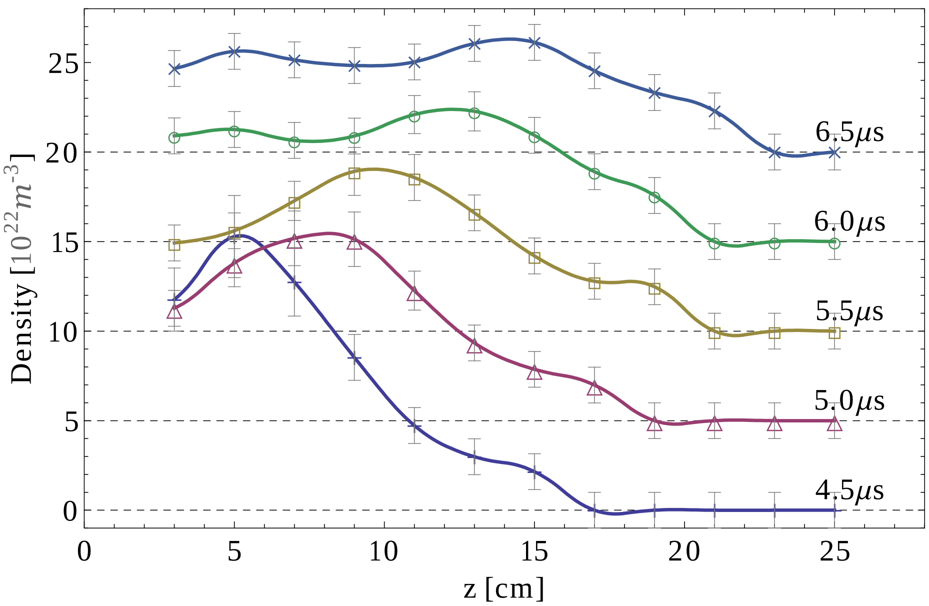

(a) Density gradient

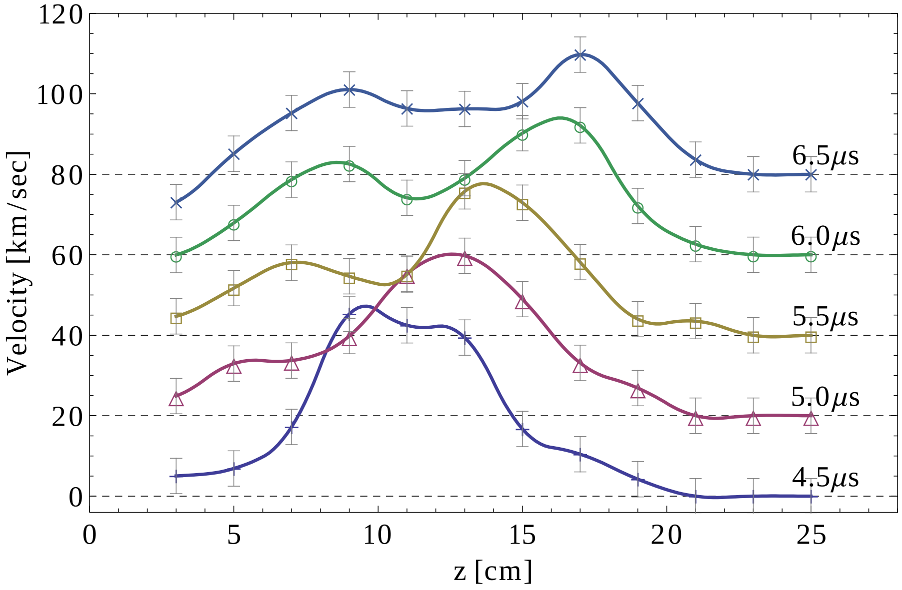

(b) Velocity gradient

Figure 4.11: (a) Density and (b) velocity along the axis of a straight column nitrogen plasma jet (shot range: 8209–8227). Densities were estimated from Stark broadened N_{II} 404.131 nm lines. Velocities were estimated from the Doppler shifts of the same N_{II} lines. The line of sight angle (∼60°) and the blue Stark shifts [25] (∼0.8 pm per 10^{22} m^{-3}) are taken into account in the velocity measurement. Solid curves are polynomial fits to the data and dashed horizontal lines indicate zero lines. Each data point is an average of three measurements. Measurement errors are the larger of $\pm 1 \times 10^{22}$ m^{-3} or ±15% for the density and ±5 km/sec for the velocity. Spectrometer ICCD exposure was 0.5 μsec.

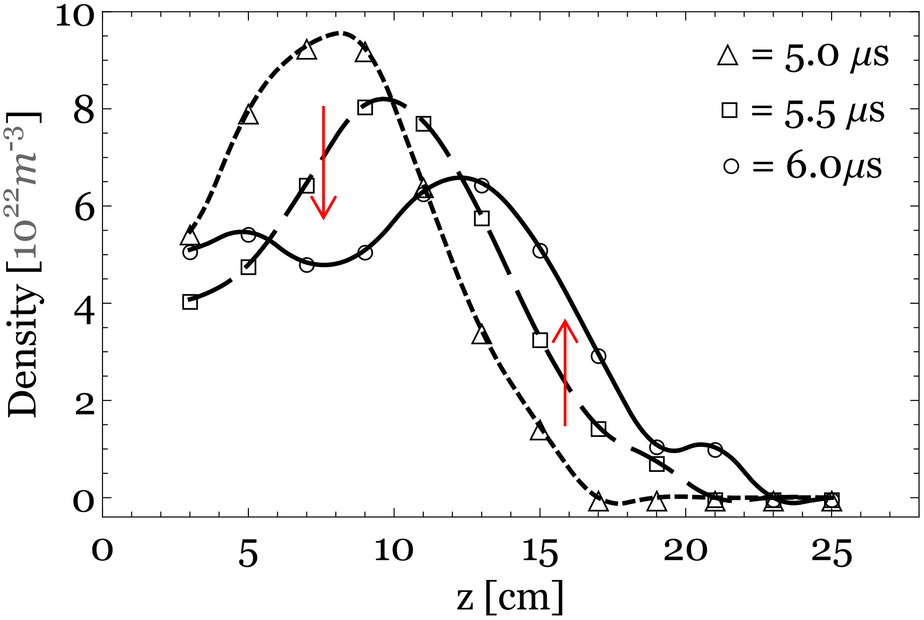

(a) Density gradient

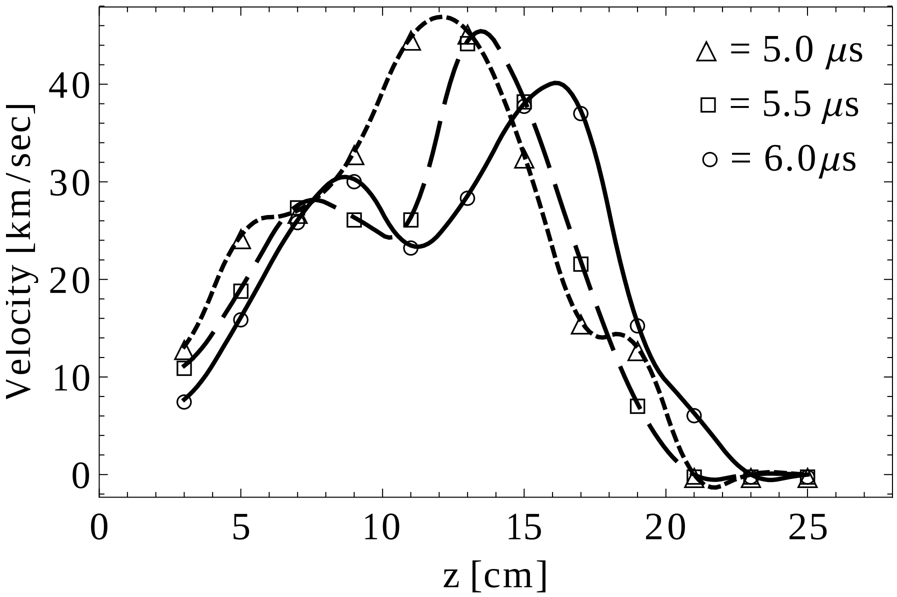

(b) Velocity gradient

Figure 4.12: Detailed view of the density and velocity profiles. The density increases near the jet front and becomes uniform in the main body of the jet as indicated by arrows.

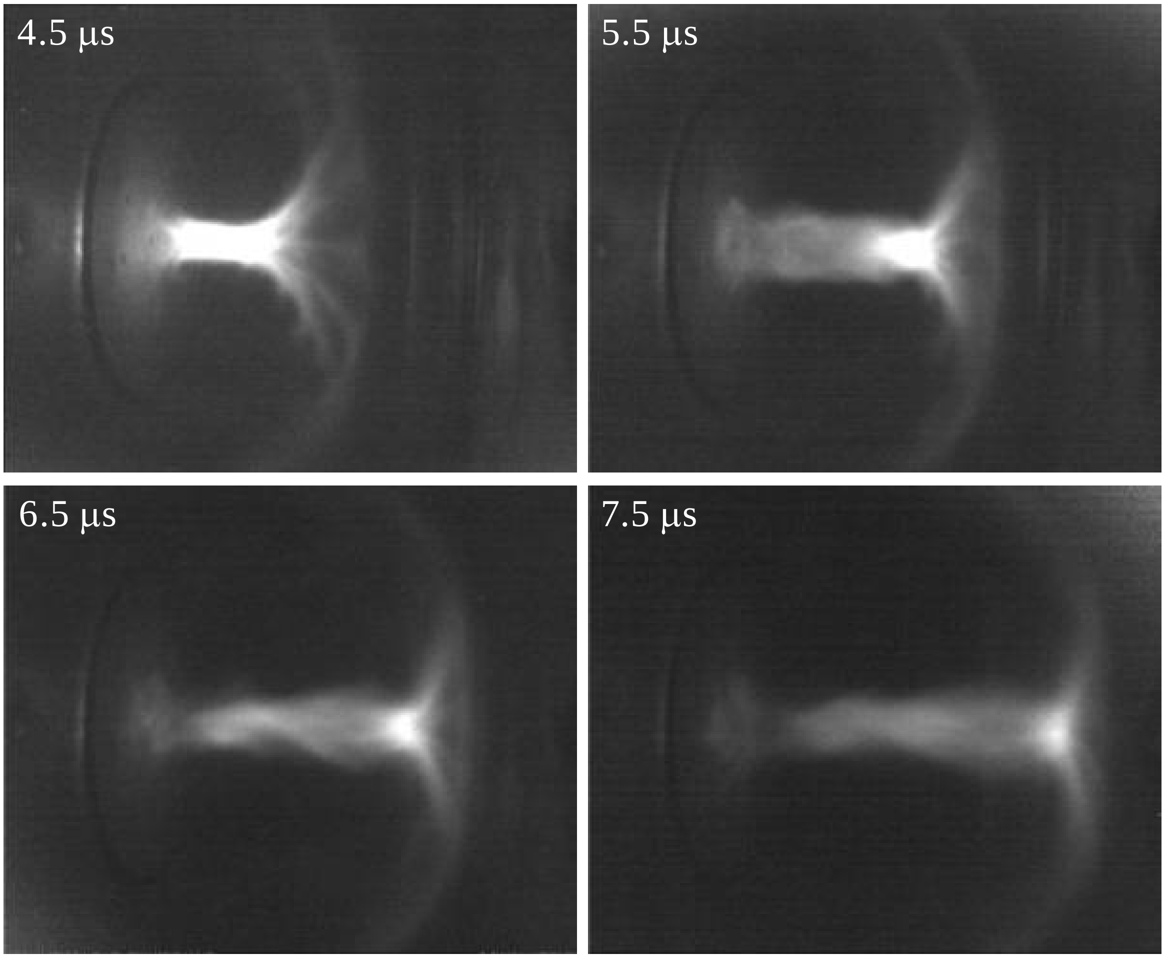

Figure 4.13: Nitrogen plasma jet (shot# 8209). The bright blob propagates with an Alfvénic velocity of ∼40 km/sec catching up the expanding outskirts of the jet.

4.4 Discussion

4.4.1 MHD pumping

The Stark broadening density measurements show that the plasma jets become very dense on a microsecond time scale. This result is supported by an independent density measurement from a laser interferometer [26]. The density of the pre-breakdown neutral gas, as measured by a fast ion gauge, is only 10^{17} m^{-3} [21]. The measured peak density of the nitrogen plasma jet is of the order 10^{23} m^{-3} at the same location 6 μsec later, so the particle density has increased by a factor of 10^6. This steep density rise cannot be explained by a pinch effect associated with the gun current flowing in the jet flux tube. The merging of the spider legs cannot account for the peak density of the jet, either, since the spider leg density ($\sim 10^{21}$ m^{-3}) is 100 times less than the jet density and the total volume of the spider legs is smaller than the volume of the central jet. Plasma particles must be pumped into the flux tubes from the source gas orifices.

According to the MHD pumping model (ref. section 1.4), the driving force of the plasma jet dynamics is the axial gradient of the azimuthal magnetic energy associated with the axial current (see equation (1.30)),

$$\rho \frac{dU_z}{dt} \approx -\frac{\partial}{\partial z}\left[\frac{B_{\phi,a}^2}{\mu_0}\right], \tag{4.7}$$

where $B_{\phi,a} = \mu_0 I_0 / 2\pi a$ is the azimuthal magnetic field at the flux tube radius a. The effective potential $B_{\phi,a}^2/\mu_0$ has negative slope everywhere because $B_{\phi,a}$ decreases along the axis due to the flared geometry of the jet flux tube. Thus, the plasma will fall down the slope and gain kinetic energy as it moves. The order of magnitude of the kinetic energy gain will be

$$\rho U_z^2 \sim -\Delta\left(\frac{B_{\phi,a}^2}{\mu_0}\right) \approx \left(\frac{B_{\phi,a}^2}{\mu_0}\right)_{z=0}. \tag{4.8}$$

Using $\rho = m_i n_e$ yields $n_e \sim \left(B_{\phi,a}^2/\mu_0\right)_{z=0} / m_i U_z^2$, where m_i is the ion mass. For nitrogen plasma jets, the observed $U_z \sim 40$ km/sec and $B_{\phi,a} \sim 1.0$ T give an electron density n_e of the order 10^{22} m^{-3}, which is consistent with the Stark broadening density measurement.

4.4.2 MHD collimation

However, the collimation of the axially expanding jet cannot be explained by this consistency check alone. Since the collimation is associated with slowing down of flow and accumulation of particles according to the MHD pumping model, the observed features of the density and velocity profiles in figure 4.12 are now examined using the continuity equation:

$$\frac{\partial \rho}{\partial t} = -\nabla \cdot (\rho \boldsymbol{U}) = -U_z \frac{\partial \rho}{\partial z} - \rho \frac{\partial U_z}{\partial z} - \nabla_\perp \cdot (\rho \boldsymbol{U}_\perp), \tag{4.9}$$

where $U_z \partial\rho/\partial z$ represents the density change due to the axial convection, negative $\rho \partial U_z/\partial z$ corresponds to an axial compression, and negative $\nabla_\perp \cdot (\rho \boldsymbol{U}_\perp)$ corresponds to a radial pinching. Since the diameter of the jet remains approximately constant during the axial expansion, the radial pinching effect can be ignored for the moment, yielding

$$\frac{\partial \rho}{\partial t} \approx -U_z \frac{\partial \rho}{\partial z} - \rho \frac{\partial U_z}{\partial z}. \tag{4.10}$$

Suppose there is no flow gradient, i.e., $\partial U_z/\partial z = 0$. Then, $\partial\rho/\partial t \approx -U_z \partial\rho/\partial z$, which can be integrated to give $\rho(z, t) = \rho(z - U_z t)$. Thus, the axial density profile would just translate without any deformation if there is no flow gradient. Our plasma jets show a large negative flow gradient ($\partial U_z/\partial z \ll 0$) at the jet front and so the density increases in that region because

$$\frac{\partial \rho}{\partial t} \approx -\rho \frac{\partial U_z}{\partial z} \gg 0 \qquad \text{(at the jet front).} \tag{4.11}$$

The observed density increase at the jet front is indicated by an arrow in figure 4.12a. The observation that the density peak always appears ~1 μsec after the velocity peak also conforms with the continuity equation because (1) at the location of the velocity peak, $\partial U_z/\partial z = 0$ and $\partial\rho/\partial z < 0$ (see figure 4.12), giving

$$\frac{\partial\rho}{\partial t} \approx -U_z\frac{\partial\rho}{\partial z} > 0 \qquad \text{(near the velocity peak)}, \tag{4.12}$$

and (2) on the other hand, at the density peak, $\partial\rho/\partial z = 0$ and $\partial U_z/\partial z > 0$, giving

$$\frac{\partial\rho}{\partial t} \approx -\rho\frac{\partial U_z}{\partial z} < 0 \qquad \text{(near the density peak)}. \tag{4.13}$$

The collimation of the axially expanding jet can be summarized as follows according to the MHD pumping model. The axial component of the $\boldsymbol{J}\times\boldsymbol{B}$ force accelerates the jet into the flared magnetic flux tube produced by the bias coil. The flow velocity slows down near the jet front where the flux tube radius is large. The slowing down of the flow results in accumulation of mass ($\partial\rho/\partial t > 0$) as well as the azimuthal magnetic flux carried by the mass flow. As the magnetic flux accumulates, the magnetic field intensity increases and so does the pinch force. The amplified pinch force subsequently squeezes the flared jet front ($\nabla_\perp\cdot\boldsymbol{U}_\perp < 0$). This squeezing action at the jet front continues while the jet expands axially into the flared flux tube, resulting in an elongated collimated jet. The density becomes uniform in the main body of the jet as it becomes collimated. This collimation scenario is sketched in figure 4.14. Essentially the same scenario accounts for the collimation of the spider legs [21], except that the collimation will be more efficient in the spider leg flux tubes because of the flow stagnation at the anode gas orifices (figure 4.15).

The cause of the flow deceleration has not yet been investigated but could be the tension of the curved bias magnetic field lines or buildup of neutral particles swept by the jet at the flow front.

4.4.3 Total particle flux by the MHD pumping

The total particle flux ingested into the jet is approximately

$$\left(\frac{dN_\mathrm{T}}{dt}\right)_\mathrm{MHD} = \pi a^2 n_e U_z \sim 10^{18}\ \text{particles}/\mu\text{sec}, \tag{4.14}$$

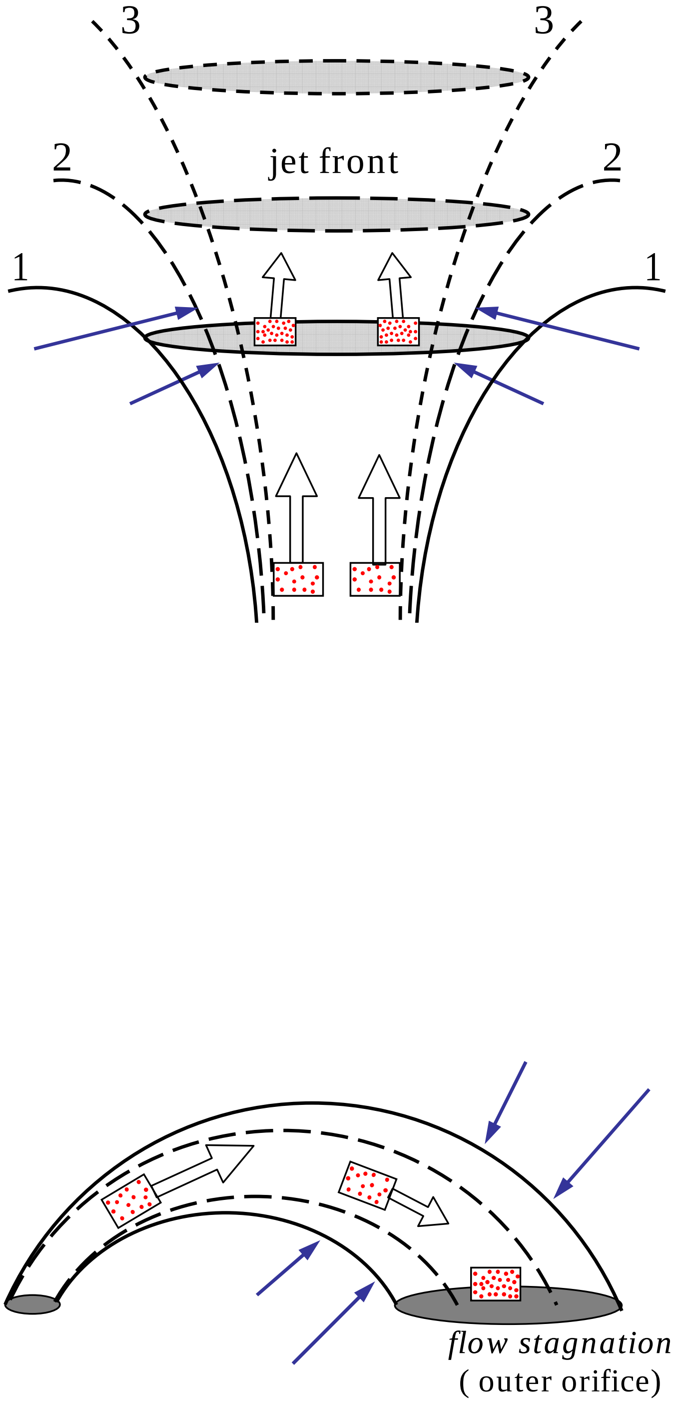

Figure 4.15: Collimation of the spider leg. Plasma flow stagnates at the outer anode orifice. Since the foot points of the spider leg are fixed, its axial length remains approximately constant during collimation. The initial flux surface is indicated by solid curves and the later flux surface by dashed curves.

using $a \sim 3$ cm, $n_e \sim 10^{22}$ m^{-3}, and $U_z \sim 30$ km/sec. Again, this MHD pumping speed is much faster than the gas puffing, $dN_{\mathrm{T}}/dt \approx 10^{16}$ μsec^{-1} (cf. equation (2.3)). Integrating over the plasma duration of $\sim$10 μsec (which is limited by the capacitance of the main gun bank), the total number of particles ingested by the MHD pumping is $N_{\mathrm{T,\,MHD}} \sim 10^{19}$. This amounts to about 20% of the total number of puffed particles (cf. equation (2.2)).

4.4.4 Application – tokamak fueling

Recent work by Voronin et al. [27] suggests that our coplanar plasma gun producing high density plasma jets by the MHD pumping mechanism might be capable of fuelling a magnetized plasma of fusion interest. In the Voronin et al. experiment, high kinetic energy plasma jets were produced by a double-stage Marshall gun, which first ionizes a hydrogen gas released from titanium grains and then accelerates the resulting hydrogen plasma. These plasma jets were successfully injected into the Globus-M spherical tokamak and had parameters comparable to our experiment (Globus-M: $n_e \sim 10^{22}$ m^{-3}, total number of accelerated particles $N_{tot} \sim 1$–5×10^{19}, $U_z \sim 50$–100 km/sec, and our experiment: $n_e \sim 10^{22-23}$ m^{-3}, $N_{tot} \sim 10^{19}$, $U_z \sim 30$ km/sec). This suggests that our plasma jets may be suitable for tokamak fuelling. Higher velocity for deep penetration [1, chap. 16] can be achieved by increasing the gun current and the minimal contact with electrodes in our plasma gun ensures purity of the plasma jets.

Chapter 5

Stark broadening

The Stark effect is the splitting and shifting of a spectral line in the presence of an electric field. The Stark effect differs significantly among spectral lines and can be divided into two categories according to its dependence on the applied electric field, namely, the linear Stark effect and the quadratic Stark effect. The Stark effect is linear for hydrogenic lines and quadratic for non-hydrogenic lines in general. The linear Stark effect is usually much stronger than the quadratic Stark effect.

In a plasma environment, a radiating atom or ion (emitter) is under the influence of the local electric fields produced by the surrounding ions and electrons within the Debye sphere of the emitter. The collective Stark effect due to these local electric fields results in broadening of spectral lines, i.e., Stark broadening. The emitter experiences two very different electric fields, the quasi-static electric field due to slow moving ions and the transient electric field due to fast moving electrons. The quasi-static electric field splits a degenerate atomic level of the emitter into distinct individual components called Stark components. The Stark components are then broadened by the transient electric field due to electron impacts. If the atomic level is not degenerate, the level undergoes only the electron impact broadening. The resulting line profile will be the sum of all possible transitions from the Stark components of an upper level to the Stark components of a lower level. The profile width serves as the first-order description for the Stark broadened line profile although the profile can have other features such as shifts and asymmetries. The profile width has a strong dependence on charged particle density and so the Stark broadening provides a convenient and inexpensive method for determining plasma density [23].

Stark broadening has been studied most extensively for hydrogen lines both in theory and experiment because the linear Stark effect is much stronger than the quadratic Stark effect and the hydrogen atom is the simplest quantum-mechanical system. Hydrogen Balmer lines have been the most popular choice for plasma density diagnosis because of well-established theoretical and experimental studies on the Stark broadening of Balmer lines. In particular, the H_β line is the best density indicator because its Stark width is nearly independent of plasma temperature. When H_β Stark broadening is small compared to other broadening effects such as Doppler broadening and Zeeman splitting, higher-n Balmer lines can be used since the Stark broadening is generally larger for higher principal quantum number n. For example, merging of high-n Balmer lines (i.e., Inglis-Teller limit) has been utilized to determine the density in edge regions ($n_e \sim 10^{20-21}$ m^{-3}, $B \sim$ several Teslas) of tokamak devices [28] [29] [24]. The present experiment lies in the opposite situation, namely where H_β Stark broadening is large compared to Zeeman and Doppler effects.

The following sections summarize Stark broadening from basic principles. More thorough theoretical account of Stark broadening can be found in reviews by Margenau and Lewis [30], Lisitsa [31], and Luque, Calzada, and Sáez [32].

5.1 Quadratic Stark effect

Consider an atom having a single electron or a single valence electron in its outermost shell subject to a uniform electric field F in the positive z-direction. The Hamiltonian of the system is the sum of the unperturbed Hamiltonian $H_0 = p^2/2m_e + V(r)$ and the perturbing Hamiltonian $H_1 = eFZ$:

$$H = H_0 + H_1 = \frac{p^2}{2m_e} + V(r) + eFZ, \tag{5.1}$$

where p, m_e, and e are the momentum, mass, and charge of the electron, and $V(r)$ is a central potential.

The effect of the perturbing electric field on the energy levels can be evaluated using the perturbation theory. According to the perturbation theory [33, chap. 16], the change in the energy level E_k is given by (up to the second order in H_1)

$$\Delta E_k \simeq \langle k|H_1|k\rangle + \sum_{k'\neq k} \frac{|\langle k|H_1|k'\rangle|^2}{E_k - E_{k'}}, \tag{5.2}$$

where $|k\rangle$'s and E_k's are the eigenstates and the corresponding energy levels of the unperturbed Hamiltonian H_0. The eigenstate $|k\rangle$ and the energy level E_k are commonly represented as $|n, l, m\rangle$ and E_{nlm} by the triple quantum number (n, l, m), i.e., principal quantum number n, azimuthal quantum number l, and magnetic quantum number m. It is assumed that the unperturbed energy levels are completely known and non-degenerate (i.e., $E_k \neq E_{k'}$ unless $k = k'$) so that the perturbation theory can be applied without difficulty.

Equation (5.2) is rewritten by replacing $|k\rangle$ with $|n, l, m\rangle$,

$$\Delta E_{nlm} \simeq eF\langle n, l, m|Z|n, l, m\rangle + e^2F^2 \sum_{(n',l',m')\neq(n,l,m)} \frac{|\langle n, l, m|Z|n', l', m'\rangle|^2}{E_{nlm} - E_{n'l'm'}}. \tag{5.3}$$

This expression can be simplified by applying two selection rules derived in appendix E, i.e., $\langle n, l, m|Z|n', l', m'\rangle \neq 0$ only if (1) $m' = m$ and (2) $l = l' = 0$ or $l' = l \pm 1$. The first order term $eF\langle n, l, m|Z|n, l, m\rangle$ vanishes unless $l = 0$ by the second selection rule. However, $\langle n, 0, 0|Z|n, 0, 0\rangle = 0$ since $|n, 0, 0\rangle$ is spherically symmetric. Thus, the first order term always vanishes leaving only the second order terms and hence ΔE_{nlm} is quadratic in the applied electric field F.

$$\Delta E_{nlm} \simeq e^2F^2 \sum_{n'} \sum_{l'=l\pm1} \frac{|\langle n, l, m|Z|n', l', m\rangle|^2}{E_{nlm} - E_{n'l'm}} \equiv -\frac{1}{2}\alpha_{nlm}F^2, \tag{5.4}$$

where α_{nlm} is the polarizability of the eigenstate $|nlm\rangle$. For example, the polarizability of the ground state ($n = 1$) of the hydrogen atom (this is the only hydrogen state that the perturbation theory can handle for now since the $n > 1$ hydrogen states are degenerate) is

$$\alpha_{100} = -2e^2 \sum_{n'>1} \frac{|\langle 1,0,0|Z|n',1,0\rangle|^2}{E_{100} - E_{n'00}} = 18\pi\epsilon_0 a_0^3, \tag{5.5}$$

where a_0 is the Bohr radius.

In general, non-hydrogenic energy levels are non-degenerate and so they experience the quadratic Stark effect. Strictly speaking, most energy levels of the Hamiltonian H_0 are degenerate with respect to m (eigenstates of the same n, l but different m have the same energy) due to the spherical symmetry of the potential $V(r)$. However, this degeneracy becomes inconsequential in the application of the perturbation theory because the states with the same l will be excluded by the second selection rule. In contrast, the $n > 1$ energy levels of the hydrogen atom are intrinsically degenerate, i.e., degenerate with respect to l (eigenstates of the same n but different l, m have the same energy) due to the pure Coulomb potential $V(r) \propto 1/r$. The $n > 1$ hydrogen energy levels experience a different Stark effect due to this special degeneracy, which is considered separately in the following section. Non-hydrogenic atoms have an effective potential differing from the pure Coulomb potential ($\propto 1/r$) due to the presence of the inner electrons shielding the nucleus.

5.2 Linear Stark effect

Consider an N_n-fold degenerate energy level E_n

$$H_0|n,g\rangle = E_n|n,g\rangle \qquad (g = 1, \ldots, N_n),$$

where the eigenstates $|n,g\rangle$ are specified by a pair of quantum numbers (n,g) instead of the triple (n,l,m) for notational simplicity. The perturbation equation (5.3) cannot be applied to the degenerate eigenstate $|n,g\rangle$ because the second order terms involving the eigenstates $|n,g'\rangle$ $(g' \neq g)$ are ill-defined as the denominator $E_{ng} - E_{ng'} = E_n - E_n = 0$. This difficulty can be avoided by choosing a new orthonormal linear combination of the original degenerate eigenstates (i.e., a new basis spanning the degenerate space of the energy level E_n) to be simultaneous eigenstates of the perturbation H_1, which is always possible:

$$|n,g\rangle = \sum_{g_0'=1}^{N_n} \langle n,g_0'|n,g\rangle\,|n,g_0\rangle \qquad \text{and} \tag{5.6}$$

$$H_1|n,g\rangle = (eFZ)|n,g\rangle = eF\lambda_{ng}|n,g\rangle, \tag{5.7}$$

where $|n,g\rangle$'s are the new basis vectors, $|n,g_0\rangle$'s are the original basis vectors, and λ_{ng}'s are eigenvalues of the operator Z. Then, all the singular terms in equation (5.3) vanish since $\langle n,g'|H_1|n,g\rangle = eF\lambda_{ng}\langle n,g'|n,g\rangle = 0$ $(g' \neq g)$, yielding

$$\begin{aligned}\Delta E_{ng} &\simeq \langle n,g|H_1|n,g\rangle + \sum_{(n',g')\neq(n,g)} \frac{|\langle n,g|H_1|n',g'\rangle|^2}{E_{ng}-E_{n'g'}} \\ &= eF\lambda_{ng} + \sum_{n'\neq n,g'} \frac{|\langle n,g|H_1|n',g'\rangle|^2}{E_n-E_{n'g'}} \\ &\approx e\lambda_{ng}F. \end{aligned} \tag{5.8}$$

Thus, for a degenerate state, ΔE_{ng} is linear in the applied electric field F.

As an example, consider the $n=2$ hydrogen states, i.e., the 2s state $|2,0,0\rangle$ and the three 2p states $|2,1,0\rangle, |2,1,1\rangle$, and $|2,1,-1\rangle$. The operator Z can represented in a matrix form using these eigenstate vectors in order to find the eigenvalues λ_{2g}'s:

$$\mathbf{Z} = \begin{pmatrix} 0 & \langle 2,0,0|Z|2,1,0\rangle & 0 & 0 \\ \langle 2,0,0|Z|2,1,0\rangle & 0 & 0 & 0 \\ 0 & 0 & 0 & 0 \\ 0 & 0 & 0 & 0 \end{pmatrix} = \begin{pmatrix} 0 & 3a_0 & 0 & 0 \\ 3a_0 & 0 & 0 & 0 \\ 0 & 0 & 0 & 0 \\ 0 & 0 & 0 & 0 \end{pmatrix}, \tag{5.9}$$

where the selection rules (ref. appendix E) are utilized to evaluate the matrix element $\mathbf{Z}_{ij} = \langle 2,g_i|Z|2,g_j\rangle$. The four eigenvalues corresponding to this matrix are $3a_0, -3a_0, 0$, and 0. Thus, the four-fold degenerate energy level E_2 splits into three levels by the applied electric field F.

$$\Delta E_2 = 0, \pm 3a_0 eF. \tag{5.10}$$

The linear Stark effect is much stronger than the quadratic Stark effect in general. For instance, compare the linear Stark effect of the hydrogen $n = 2$ state (ΔE_2) calculated above to the quadratic Stark effect of the hydrogen $n = 1$ state (ΔE_1) discussed in the previous section.

$$\left|\frac{\Delta E_2}{\Delta E_1}\right| = \frac{3a_0 eF}{\alpha_{100} F^2/2} = \frac{3a_0 eF}{9\pi\epsilon_0 a_0^3 F^2} = \frac{e/(3\pi\epsilon_0 a_0^2)}{F} \gg 1,$$

because $e/(3\pi\epsilon_0 a_0^2) \approx$ (electric field strength at the Bohr radius from a charge e) $\approx 5 \times 10^{11}$ V/m would be much larger than the applied electric field F in most cases. The hydrogen spectral lines show a very large Stark effect compared to any other non-hydrogenic spectral lines because of the strong linear Stark effect.

5.3 Line broadening by charged particles

Imagine a charged particle with charge q moves past a radiating atom (emitter). The charged particle exerts a time-varying Coulombic electric field $F(r(t)) \sim q/r^2(t)$ on the emitter, where $r(t)$, the distance from the charged particle to the emitter, depends on the initial location and velocity of the charged particle. Such an electric field is commonly called as a microfield in the Stark theory literature. The microfield perturbs the energy states of the emitter via the Stark effect:

$$\Delta\omega(t) = C_a F^k(r(t)), \tag{5.11}$$

where the Stark effect is represented by the frequency shift $\Delta\omega$ instead of the energy level shift $\Delta E = \hbar\Delta\omega$, C_a is the Stark effect constant of an energy state a, and $k = 1$ for the linear Stark effect and $k = 2$ for the quadratic Stark effect.

The critical impact parameter for this Coulombic collision to induce a total loss of coherence of the energy state is called the Weisskopf radius, ρ_W. The Weisskopf radius is roughly proportional to the Stark effect constant C_a and inversely proportional to the velocity v of the charged particle.

$$\rho_W \sim \frac{C_a}{v}. \tag{5.12}$$

A collision with the impact parameter much smaller than ρ_W will not cause a significant Stark effect. The Weisskopf radius defines the effective cross section of the Stark effect, also known as the optical cross section,

$$\sigma_W = \pi\rho_W^2 \sim \pi\frac{C_a^2}{v^2}. \tag{5.13}$$

The Weisskopf radius also determines the effective duration of the critical collision called as Weisskopf collision time

$$\tau_W = \frac{\rho_w}{v} \sim \frac{C_a}{v^2}. \tag{5.14}$$

For t_W much longer than the mean lifetime of an excited state, the microfield is effectively static during the collision. On the other hand, for t_W much shorter than the mean lifetime of the excited state, the microfield can be considered as an instantaneous perturbation. The former assumption (quasi-static approximation) is usually valid for ion collisions and the latter (impact approximation) for electron collisions since the electron thermal velocity is much faster than the ion thermal velocity.

The Weisskopf radius ρ_W defines another important parameter, the effective number of particles interacting simultaneously with the emitter.

$$g \equiv n\rho_W^3, \tag{5.15}$$

where n is the particle density. For example, if $g \ll 1$, only the nearest particle interacts with the emitter, but, on the other hand, if $g \gg 1$, a large number of particles simultaneously affect the emitter.

The ensemble average of the Coulombic collisions of the emitter with charged particles results in broadening of the energy levels, a collective Stark effect called as

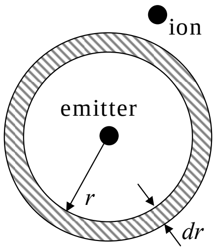

Figure 5.1: Nearest neighbor approximation of the ionic electric field.

Stark broadening. The average microfield $F(r(t))$ depends on the velocity and density distributions of the charged particles and so does the Stark broadening.

5.3.1 Quasi-static approximation – ion microfield

The microfield produced by an ion can be assumed to be static since the collision of the ion with the emitter is a slow process (due to the slow ion thermal velocity) compared to the atomic line transitions (lifetime $\tau_0 \sim 10$ nsec for strong lines), i.e., $\tau_W \gg \tau_0$. It is also assumed that the collisions are binary meaning that the emitter is under the influence of only one ion at a time. This assumption will be valid if $g = n_i \rho_W^3 \lesssim 1$, where n_i is the ion number density. It follows from these two assumptions that the profile of the frequency shift $\Delta\omega$ will depend on the distribution of the individual static ion microfield $F(r(t)) = F(r) \sim Ze/r^2$, where Z is the charge number of the ion.

Consider only the nearest ion to get an approximate microfield distribution. Let $p(r)dr$ be the probability that the nearest neighbor is in the shell $(r, r + dr)$, $f_i(r)dr$ be the probability to find an ion in the shell, and $P^*(r)$ be the probability that no ion is inside the radius r. Note that $f_i(r) = n_i 4\pi r^2 dr$. Then,

$$\left.\begin{aligned} p(r)dr &= P^*(r) \times f_i(r)dr \\ P^*(r) &= 1 - \textstyle\int_0^r p(r)dr \end{aligned}\right\} \quad \Longrightarrow \quad \frac{p(r)}{f_i(r)} = \left(1 - \int_0^r p(r)dr\right). \tag{5.16}$$

Differentiate and then integrate the above equation to solve for $p(r)$

$$\frac{d}{dr}\left(\frac{p(r)}{f_i(r)}\right) = -p(r) = -\frac{p(r)}{f_i(r)} \times f_i(r) \implies \log\frac{p(r)}{f_i(r)} = -\int f_i(r)dr$$
$$\implies p(r) = f_i(r)\exp(-\int f_i(r)dr) = n_i 4\pi r^2 \exp(-n_i 4\pi r^3/3). \tag{5.17}$$

The ions in the shell $(r, r+dr)$ will induce Stark shifts in the range $(\Delta\omega, \Delta\omega+d\omega)$ according to equation (5.11), $\Delta\omega = C_a F^k(r)$. It is convenient to normalize the radius by the inter-particle distance $r_0 = (3/4\pi n_i)^{1/3}$ and the Stark frequency shift by $\Delta\omega_0 = C_a F^k(r = r_0)$:

$$\beta \equiv \frac{\Delta\omega}{\Delta\omega_0} = \left(\frac{F(r)}{F(r_0)}\right)^k = (r/r_0)^{-2k} \quad (\because F \sim \frac{1}{r^2}), \tag{5.18}$$
$$d\beta = -2k\left(\frac{r}{r_0}\right)^{-2k-1}\frac{dr}{r_0} = -2k\beta\frac{dr}{r}. \tag{5.19}$$

Equations (5.17)–(5.19) yield the profile $I(\beta)$ of the Stark frequency shift,

$$I(\beta) = p(r)\left|\frac{dr}{d\beta}\right| = \frac{n_i 4\pi r^3}{2k\beta}\exp(-n_i 4\pi r^3/3) = 3\frac{(r/r_0)^3}{2k\beta}\exp(-(r/r_0)^3)$$
$$= \frac{3}{2k}\beta^{-(1+3/2k)}\exp(-\beta^{-3/2k}). \tag{5.20}$$

A more involved treatment taking into account all ions, not just the nearest one, leads to a profile known as Holtsmark function [34].

$$I(\beta) = \frac{2}{\pi}\beta\int_0^\infty x\,\sin(\beta x)\exp(-x^{3/2k})\,dx \tag{5.21}$$

The real profile of the Stark frequency shift by ions will be in-between the Holtsmark function and the nearest neighbor profile (see figure 5.2) because of the Debye screening. The separation of the two peaks occurring at $\beta \sim \pm 1.5$ may serve as the width

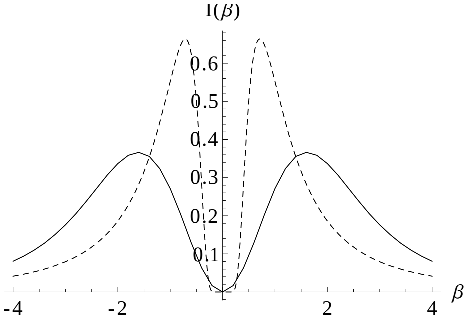

Figure 5.2: The Holtsmark profile (solid line) and the nearest neighbor profile (dashed line) for the linear Stark effect ($k = 1$).

of the profile. Thus, the width of the un-scaled profile $I(\Delta\omega)$ is

$$\begin{aligned} \text{width of } I(\Delta\omega) \sim 3\Delta\omega_0 \sim 3C_a F^k(r_0) \propto C_a r_0^{-2k} &= C_a(3/4\pi n_i)^{-2k/3} \\ \propto C_a n_i^{2k/3} \propto C_a n_e^{2k/3}, \end{aligned} \tag{5.22}$$

where $n_e = Zn_i$ is the electron density of the plasma.

5.3.2 Impact approximation – electron microfield

In contrast to ions, fast moving electrons perturb the emitter only momentarily, i.e., the duration of electron impact is much shorter than the lifetime of the excited states of the emitter. In this limit, the Stark effect depends only on the frequency of the electron impact, whose inverse, the average interval between impacts, shall not be confused with the impact duration. The impact frequency ν_c is related to the Stark effect cross section σ_W (equation (5.13)) as

$$\nu_c = n_e \sigma_W v_e, \tag{5.23}$$

where n_e and v_e are the electron number density and velocity, respectively.

An excited state of the emitter can be viewed as a quantum oscillator with its frequency ω_0 related to its energy E as $E = \hbar\omega_0$. The excited state makes a transition into a lower energy state with a natural lifetime τ_0. The ensemble average of the excited state can be represented by a wavefunction $\psi(t)$ as

$$\psi(t) \sim e^{i\omega_0 t} e^{-t/\tau_0}, \tag{5.24}$$

where the exponential decay term appears because the transition is a random process (Poisson process) with the characteristic frequency $\nu_0 = 1/\tau_0$. As a result of this natural decay, a band of frequencies will be observed instead of a single frequency ω_0 in the frequency space of $\psi(t)$:

$$\tilde{\psi}(\omega) \sim \int_0^\infty e^{i\omega_0 t} e^{-t/\tau_0} e^{-i\omega t}\, dt = \frac{1}{i(\omega_0 - \omega) - \nu_0}, \tag{5.25}$$

where $\tilde{\psi}(\omega)$ is the Fourier transform of $\psi(t)$. Hence, the amplitude of the frequency component ω is

$$I(\omega) = \left|\tilde{\psi}(\omega)\right|^2 \sim \frac{1}{(\omega - \omega_0)^2 + \nu_0^2}. \tag{5.26}$$

This frequency dispersion is called as natural broadening and its shape is known as Lorentzian profile. The full width at half maximum (FWHM) of the profile is $2\nu_0$. The natural broadening ($2\nu_0 \sim 10^8$ Hz for strong atomic lines) is negligible compared to the optical frequency $\sim 10^{15}$ Hz.

The electron impact perturbs the excited state and causes the state to decay into a lower energy state, effectively shortening the lifetime of the excited state. Thus, the frequency spectrum of the state will further spread beyond the natural broadening, since the electron impact is essentially the same statistical event (Poisson process) as the natural decay. The impact frequency ν_c is typically greater than the natural decay frequency ν_0. Thus, the intensity profile of the frequency shift $\Delta\omega = \omega - \omega_0$ will be primarily broadened by the electron impact:

$$I(\Delta\omega) \sim \frac{1}{\Delta\omega^2 + \nu_c^2}. \tag{5.27}$$

The profile width of $I(\Delta\omega)$ scales as

$$\text{width of } I(\Delta\omega) = 2\nu_c \sim 2n_e\sigma_W v_e \sim n_e(C_a/v_e)^2 v_e = C_a^2 n_e/v_e. \tag{5.28}$$

5.4 Density diagnosis using the Stark broadened profiles

The ultimate profile of the frequency shift of an energy level, $I(\Delta\omega)$, is the convolution of the quasi-static and the electron impact broadenings. The transition from a broadened upper level to a broadened lower level results in a broadened spectral line. In a real plasma, the line profile is further modified by secondary effects such as Debye screening [35] and ion motion [36] [37] [24]. Theories that take into account these secondary effects have predicted Stark broadening of hydrogen Balmer lines in good agreement (within 1%–10%) with experiments.

For hydrogen lines, the quasi-static microfield splits degenerate energy levels via the strong linear Stark effect. The line profile is dominantly broadened as a result of this splitting, and so the profile width scales with $n_e^{2/3}$ according to equation (5.22) with $k = 1$. It is customary to express the profile width by a parameter $\alpha_{1/2}$, the so called reduced *half*-width that scales the line shape [23]:

$$w_S = 2.5 \times 10^{-14}\, \alpha_{1/2}\, n_e^{2/3}, \tag{5.29}$$

where w_S is the Stark FWHM in nm and n_e is the electron density in m^{-3}. The half-width $\alpha_{1/2}$ has been tabulated for many hydrogen lines based on both theoretical calculations and experimental data for the temperature range 0.5–4 eV and density range 10^{20}–10^{24} m^{-3} [35] [36] [24].

For lines of non-hydrogenic atoms, the electron impact broadening via the quadratic Stark effect is the dominant broadening mechanism [23]. Thus, to a first approximation, the line profile is Lorentzian and linearly proportional to the electron density according to equations (5.27) and (5.28):

$$w_S \approx w_m n_e, \tag{5.30}$$

where w_m is the proportionality parameter. For an extensive collection of N II lines, this property has been substantiated by the experimental work of Mar et al. [38]. Measurements of Stark broadening of non-hydrogenic spectral lines have been tabulated for well-defined and independently measured plasma conditions [25].

Chapter 6

Analysis of spectral line profiles

6.1 Density estimation from spectral line profiles

The profile of a Stark broadened line is a complicated function of plasma density and temperature as described in chapter 5. However, for electron density measurement, the detail of the Stark broadened profile is not necessarily required. Instead, the full width at half maximum (FWHM) of the profile is used because the electron density is a simple function of the Stark FWHM for many spectral lines. Even though this simple approximation is applicable for most spectral lines, extraction of the pure Stark effect from a line profile is generally not straightforward. To clarify difficulties in reliable density estimation from Stark broadened line profiles, issues pertinent to our plasma source are discussed [23].

6.1.1 Uncertainty in Stark parameter

The reduced half-width $\alpha_{1/2}$ for hydrogen lines (equation (5.29)) has a weak dependence on density and on temperature. In addition, it differs slightly between calculations. The half-width $\alpha_{1/2}$ of the H_β line (approximately 0.085) is plotted as a function of temperature (density) for several representative densities (temperatures) in figure 6.1a(b) according to the Gigosos-Cardeñoso (GC) theory [36] and according to the Kepple-Griem (KG) theory [35], showing a slight discrepancy between the two theories. The uncertainty in $\alpha_{1/2}$ introduces an error $< 20\%$ in density estimation for

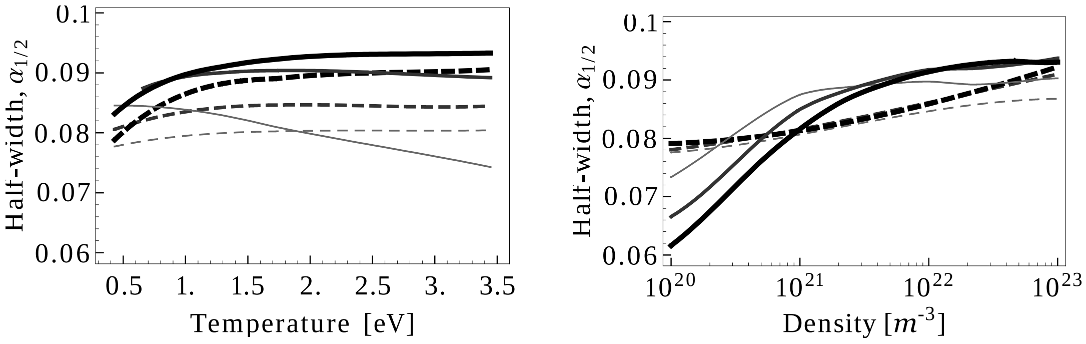

(a) $\alpha_{1/2}$ vs. temperature

(b) $\alpha_{1/2}$ vs. density

Figure 6.1: Reduced half-width $\alpha_{1/2}$ of theoretical H_β Stark profiles according to the GC theory (solid lines) and according to the KG theory (dashed lines). (a) $\alpha_{1/2}$ versus temperature for densities $5 \times 10^{20}, 5 \times 10^{21}, 5 \times 10^{22}$ m^{-3}. Lines are drawn thicker for increasing density. (b) $\alpha_{1/2}$ versus density for temperatures 1, 2, and 3 eV. Lines are drawn thicker for increasing temperature.

the hydrogen plasma jets.

Non-hydrogenic spectral lines are used to measure the density of non-hydrogen (nitrogen, argon, etc) plasma jets. The uncertainties are about 15%–30% for the Stark width parameters w_m (see equation (5.30)) of the spectral lines used in the present study. For instance, the Stark width parameter for N II 424.178 nm is $w_m = 152.6\,\mathrm{pm}/10^{23}\,\mathrm{m}^{-3}$ within 23% error [25].

6.1.2 Competing broadening effects

Besides Stark broadening, a spectral line can be broadened by other effects such as Doppler effect, instrumental broadening, and Zeeman splitting.

The Doppler broadening is due to the thermal motion of emitters and the profile is a Gaussian function with FWHM w_D,

$$w_D = 7.7 \times 10^{-5} \lambda \sqrt{T_i/M}, \tag{6.1}$$

where λ is the wavelength of the spectral line, T_i is the emitter temperature ($\simeq$ the ion temperature) in eV, and M is the emitter mass in amu. The ion temperature T_i appears to be less than 10 eV in the plasma jets. Therefore, 20 pm $\leq w_D \leq$ 100 pm for hydrogen lines and 6 pm $\leq w_D \leq$ 30 pm for nitrogen lines in the wavelength range 300–500 nm.

The presumption of low $T_i < 10$ eV is supported by an impurity line measurement (C III 229.687 nm) showing broadening $\leq$ 10 pm corresponding to $T_i \leq 4$ eV (see the inset profile in figure 6.3). It had been assumed that $T_i \sim T_e$ in the previous work [9, 21], where T_e was either measured by a triple Langmuir probe (5–15 eV) or inferred from spectral line ratios (1–5 eV). For nitrogen plasma jets, the assumption is supported by a good agreement between the measured line ratios and the calculated line ratios using the Saha-Boltzmann equation, suggesting that the plasma jets are at local thermodynamic equilibrium and so $T_i \sim T_e \lesssim 10$ eV. Significant ion heating ($T_i \gg T_e$) via magnetic reconnection has been observed in some other gun-produced spheromak plasmas [1, chap. 13]. However, magnetic reconnection is not a dominant mechanism in the plasma jets under consideration here as the magnetic topology is not undergoing changes. There is mainly a stretching of field lines, but not reconnection (except for the minimal reconnection associated with merging of spider legs).

The instrumental function describes the spreading of a monochromatic light source recorded by an spectroscopic system. The instrumental function is mainly determined by the fiber core size, the slit width, and the entrance optics in the present spectroscopic system (section 3.7). The instrumental function is measured by recording a known spectral line emitted from a spectrum tube within or close to the spectral range of interest. The measured instrumental broadening is ∼7 ICCD pixels at FWHM, which corresponds to ∼30 pm according to the pixel resolution equation (3.2). The Zeeman splitting of the energy levels [33, chap. 17] is $\Delta E \sim \mu_B B$, where $\mu_B = e\hbar/2m_e$ is the Bohr magneton. In terms of wavelength, the Zeeman effect is given by $\Delta\lambda_{[\mathrm{pm}]} \sim 10^{-4}\lambda^2_{[\mathrm{nm}]}B_{[\mathrm{Tesla}]} < 8$ pm for $B = 0.3$ Tesla, and so the Zeeman effect is negligible. Spectral lines can also split via the Doppler effect if there exist relative bulk flow motions within the line of sight volume. However, such a splitting will be minimal because it is less than 50 pm even for unlikely 30 km/sec relative flow motions.

If a line width is measured greater than 200 pm, it can simply be taken as the

Stark width because the other effects cannot account for a line width > 100 pm, and so the Stark effect must be the dominant broadening effect in such a case. For H_β line, the Stark broadening becomes dominant for $n_e \gtrsim 10^{21}$ m^{-3} according to equation (5.29). If the measured line width is comparable to the instrumental broadening or the expected Doppler broadening, the Stark width can be estimated using one of the deconvolution procedures described in the next sections 6.2, 6.3, and 6.4.

6.1.3 Plasma inhomogeneity

The plasma jets in our experiments have internal structures (see figure. 3.8b) and so may have a density gradient along the line of sight. A significant distortion may occur at the center of a line profile as illustrated in figure 6.2a because the lower density region concentrates its emission energy in a narrow band while the higher density region spreads the emission energy over a broad band.

In particular, special care must be applied to the interpretation of the characteristic central dip of the H_β line. The density gradient effect becomes more appreciable in the central dip region as the narrow H_β emission from a low density region can stand out in that region. The H_β central dip can appear in high density plasma, where the ion field discussed in chapter 5 is strong enough to make the line splitting (via the linear Stark effect) larger than the electron impact broadening. The other even-numbered hydrogen Balmer lines can also have a central dip [29].

A narrow peak overlaid over a broad envelope similar to figure 6.2a was indeed observed in some measured H_β line profiles as shown figure 6.2b. Note that the theoretical fit according to Stehlé and Hutcheon [24] lacks such a narrow peak because the theory assumes a homogeneous plasma density. The electron density may be underestimated if the peak value is used to measure the profile FWHM. For non-hydrogenic lines and hydrogen lines with no central dip, the FWHM is obtained by fitting the profile to a Lorentzian shape, since this fitting process puts more weight on the side bands than on the center and so avoids errors associated with a density gradient along the line of sight. For hydrogen lines showing the central dip, the

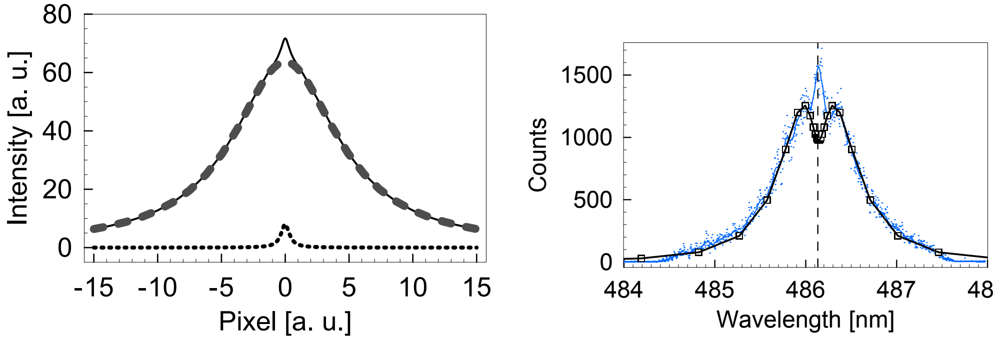

(a) (b)

Figure 6.2: (a) Sum of a wide and a narrow Lorentzian profile. Dashed line is the wide profile with total intensity = 1000 and FWHM = 10, dotted line is the narrow profile with total intensity = 20 and FWHM = 0.5, and solid line is the sum of the two profiles. (b) Measured H_β line profile showing the characteristic central dip distorted by a peak from a low density contribution (data# oma11.61, perpendicular line of sight). Measured data points are represented by dots with a fitting curve (thin solid line). Bold solid line connecting the square points is a theoretical fit according to Stehlé [24] with $n_e = 1.05 \times 10^{22}$ m^{-3} and $T_i = T_e = 2$ eV. Vertical dashed line indicates the H_β rest-frame wavelength 486.133 nm.

FWHM is not well-defined but the same Lorentizan fitting process may be used to define the FWHM. The electron density obtained via equation (5.29) using such FWHM is about the same with the electron density estimated by manually finding the best theoretical fit to the line profile (see sections 6.2 and 6.4).

6.1.4 Self-absorption, continuum background, and blending with nearby spectral lines

Self-absorption in an optically thick plasma can lead to an overestimation of electron density. Overlaps between the internal structure of the plasma jet and the objects in the background are observed in camera images when the camera is operated within its dynamic range, i.e., not saturated (see figure 3.8b). This suggests that our plasma is optically thin and so self-absorption will be insignificant.

Blackbody radiation, the background noise of the ICCD detector, Balmer continuum, etc. contribute to the background level of spectral data. Spectral profiles are corrected by subtracting the measured background level taken from spectral regions

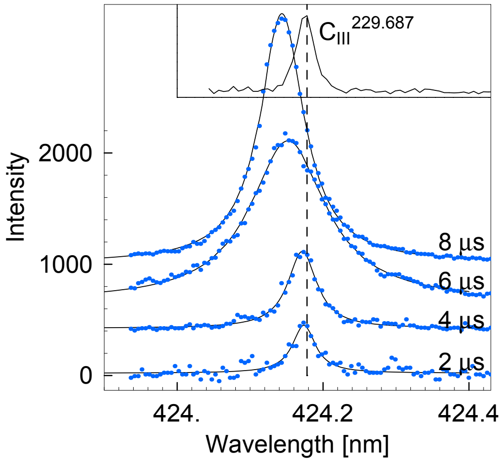

Figure 6.3: Observed line profiles (N_{II}, 424.178 nm) from a nitrogen plasma jet at $t =$ 2, 4, 6, and 8 μs after breakdown (shot#: 6736–3, 7, 11, and 15, respectively). Solid lines are Lorentzian fits. The estimated densities are 0.1, 1.7, 7.8, and 4.0×10^{22} m^{-3}, respectively. A measured impurity line profile (C_{III}, 229.687 nm) is inset at the top for width comparison. Its Doppler width ($w_D = \sqrt{w_T^2 - w_I^2}$) is ~0.007 nm, corresponding to $T_i = 2$ eV. Vertical dashed line indicates rest-frame wavelength.

close to the spectral line of interest but separated by several times its width. Additionally, every spectral line used in the experiment is isolated from other lines by at least its line width to avoid mixing.

6.2 Deconvolution of Stark broadening –simple formula

The Stark broadening and hence the electron density can be extracted from measured line profiles using a simple and computationally inexpensive procedure. The total FWHM (w_T) of a spectral line profile is measured by fitting the data to a Lorentzian profile. The Stark FWHM (w_S) is then obtained by subtracting the Doppler effect (w_D) and the instrumental function (w_I) from the total width w_T according to the conventional method [39]

$$w_S = \sqrt{w_T^2 - w_D^2 - w_I^2} \qquad \text{if} \quad w_T/\sqrt{w_D^2 + w_I^2} > 1.04. \tag{6.2}$$

This formula assumes that the instrumental function is Gaussian, the Stark broadening is Lorentzian, and so the total broadening is a Voigt profile [40], i.e., the convolution of a Gaussian profile and a Lorentzian profile. The electron density is then calculated using equation (5.29) for hydrogen lines and equation (5.30) for non-hydrogenic lines. The reliability of this simple method is substantiated by comparing the density obtained by this method with the density obtained by the theoretical fitting according to Stehlé [24] (see figure 4.7). The error in the density estimation using H_β profiles is less than 15% for $n_e \geq 10^{22}$ m^{-3} taking into account the issues discussed in the previous section. The error gets larger for lower density (25% for $n_e \sim 10^{21}$ m^{-3} and 50% for $n_e \sim 10^{20}$ m^{-3}).

6.3 Maximum entropy deconvolution

The simple formula (6.2) becomes inaccurate as the ratio $w_T/\sqrt{w_D^2 + w_I^2}$ approaches unity. However, if the instrumental effect can be removed, the ratio w_T/w_D will become significantly greater than unity since $w_D \lesssim w_I$ in our experiment, and so the simple formula will become applicable once again. The instrumental function w_I of the spectroscopic system can be removed computationally since the instrumental function is invariant and can be measured before taking spectrum. A deconvolution method based on the maximum entropy principle [41] has been implemented to remove the instrumental function and thereby achieve an effective resolution higher than the nominal spectroscopic resolution. The deconvolution method has been applied to some spectral lines for the Stark density measurement in case of $w_T \approx \sqrt{w_D^2 + w_I^2}$. The deconvolution method has also been used to separate overlapping Doppler shift components of a same spectral line and thereby resolve velocity components of plasma jets in the solar prominence simulation experiment [42, Fig. 5].

6.3.1 Undoing the instrumental broadening –an inverse problem

Removing the instrumental effect corresponds to the following ill-posed inverse problem.

$$g_i = \sum_{k=1}^{N} H_{ik} f_k \qquad (i = 1, \ldots, M), \tag{6.3}$$

where g_i is the measured signal at the i^{th} pixel, f_k is the true signal to be recovered, and H_{ik} is the instrumental function which blurs the true signal $\boldsymbol{f} = (f_1, \ldots, f_N)^t$. Since the instrumental function preserves the total intensity, the matrix H is normalized as

$$\sum_{i=1}^{M} H_{ik} = 1.$$

Hence,

$$\sum_{i=1}^{M} g_i = \sum_{i=1}^{M} \sum_{k=1}^{N} H_{ik} f_k = \sum_{k=1}^{N} \left(\sum_{i=1}^{M} H_{ik} \right) f_k = \sum_{k=1}^{N} f_k.$$

It is also convenient to normalize f so that

$$\sum_{k=1}^{N} f_k = \sum_{i=1}^{M} g_i = 1. \tag{6.4}$$

The inverse problem (6.3) is ill-posed since the matrix H is not invertible or, even if it is, the inverting process is numerically unstable. This comes at no surprise because the instrumental function smooths out fluctuations of the original signal $\boldsymbol{f}$ and so the inverse process (deconvolution) will amplify the noise in the measured signal $\boldsymbol{g}$. To examine the noise-amplifying property of the inverse process, suppose the matrix H is a square matrix ($M = N$) whose maximum and minimum eigenvalues are λ_M and λ_1, respectively, and consider a true signal $\boldsymbol{f}$ in the direction of the eigenvector of λ_M. Then, the measured signal will be

$$\boldsymbol{g} = H\boldsymbol{f} = \lambda_M \boldsymbol{f}.$$

Now imagine that the measurement introduced a small error $\Delta\boldsymbol{g}$ in the direction of the eigenvector of λ_1. The corresponding error $\Delta\boldsymbol{f}$ will appear in the true signal recovered by the inverse process as

$$\Delta\boldsymbol{g} = H\Delta\boldsymbol{f} = \lambda_1\Delta\boldsymbol{f}.$$

Thus, the relative error

$$\frac{\|\Delta\boldsymbol{f}\|}{\|\boldsymbol{f}\|} = \left|\frac{\lambda_M}{\lambda_1}\right| \frac{\|\Delta\boldsymbol{g}\|}{\|\boldsymbol{g}\|},$$

which implies that a small error in the measured signal can appear amplified by the factor of $|\lambda_M/\lambda_1|$ in the recovered signal $\boldsymbol{f}$. This factor is called the condition number of the matrix H and is a measure of the instability of the inverse process [43, sec. 5.3].

6.3.2 Constrained inverse problem

In earlier work [44], a deconvolution algorithm to solve the inverse problem (6.3) has been implemented based on the maximum entropy principle [41] and a steepest descent method devised by Bellan [45] for finding the minimum of a function. The maximum entropy principle modifies the original problem by imposing the condition that the entropy $S(f)$ defined as

$$S(f) = -\sum_{k=1}^{N} f_k \log(f_k) \tag{6.5}$$

be maximized. Suppose that f_k corresponds to the number of photons hit on the pixel k. Then, the entropy $S(f)$ is a measure for the total number of ways that the photons redistribute themselves among the n pixels but preserving the configuration $\{f_k\}$. Thus, the configuration $\{f_k\}$ which maximizes the entropy $S(f)$ under the $M+1$ constraints (6.3) and (6.4) is the least committal solution among all the possible solutions satisfying the constraints.

The maximum entropy solution f can be found using the method of Lagrange multipliers. Consider the Lagrangian

$$L(f;\lambda) = -\sum_{k=1}^{N} f_k \log(f_k) - \lambda_0 \left(\sum_{k=1}^{N} f_k - 1\right) - \sum_{i=1}^{M} \left(\lambda_i \sum_{k=1}^{N} H_{ik} f_k - g_i\right). \tag{6.6}$$

Maximization of the Lagrangian $L(f;\lambda)$ with respect to each f_k gives the solution f as a function of the Lagrange multipliers λ's:

$$f_k(\lambda) = \exp\left(-\sum_{i=1}^{M} \lambda_i H_{ik}\right) / Q(\lambda), \tag{6.7}$$

$$Q(\lambda) = \sum_{k=1}^{N} \exp\left(-\sum_{i=1}^{M} \lambda_i H_{ik}\right), \tag{6.8}$$

where the partition function $Q(\lambda)$ comes about from the normalization condition of f (equation (6.4)). The final step is to find the set of the Lagrange multipliers λ's which satisfy the system of equations (6.3):

$$g_i - \sum_{k=1}^{N} H_{ik} f_k(\lambda) = 0 \qquad (i = 1, \ldots, M). \tag{6.9}$$

Finding the roots of the above equations is equivalent to minimizing the potential function defined as

$$Z(\lambda) = \log Q(\lambda) + \sum_{i=1}^{M} \lambda_i g_i \tag{6.10}$$

because $\partial Z/\partial \lambda_i = g_i - \sum_{k=1}^{N} H_{ik} f_k(\lambda)$.

In case of $M = N$ (i.e., the matrix H_{ik} is a square matrix), it can be shown that the potential function $Z(\lambda)$ is strictly concave [46] (see appendix F for the proof), and thus, the minimization process will always lead to the single global minimum. The gradient of $Z(\lambda)$ becomes progressively weaker as one approaches the global minimum since $Z(\lambda)$ is a smooth function of λ. A steepest descent algorithm utilizing this strict concavity was devised by Bellan [45] to find the minimum. The strategy is to take iterative steps in variable size along the direction of the gradient. A large step $\varepsilon \nabla Z$ is taken initially from a starting point $\boldsymbol{\lambda}_0$ and then the potential at the new point

$\boldsymbol{\lambda}' = \boldsymbol{\lambda}_0 - \varepsilon \nabla Z$ is compared with the starting value $Z_0 = Z(\boldsymbol{\lambda}_0)$. The parameter ε is a small positive number which determines the step size. If $Z(\boldsymbol{\lambda}') > Z_0$, the step size ε is decreased and Z is re-evaluated until it becomes smaller than Z_0. If $Z(\boldsymbol{\lambda}') < Z_0$, another search starts from the new point in the new direction $\nabla Z(\boldsymbol{\lambda}')$. To avoid taking too small steps, a step size ε slightly greater than the last step size is taken at the start of each search. This steepest descent algorithm is illustrated in figure 6.4. The variance Ω at each step is defined as

$$\Omega = \frac{1}{N} \sum_i \left(g_i - \sum_k H_{ik} f_k \right)^2 = \frac{1}{N} \sum_i \left| \frac{\partial Z}{\partial \lambda_i} \right|^2 = \frac{1}{N} \left\| \nabla Z \right\|^2 \tag{6.11}$$

and is a measure of goodness of the signal recovery. The iteration stops if Ω becomes smaller than an expected variance Ω_0 or the total number of steps taken exceeds a given maximum number of steps. The parameter Ω has a practical importance [47]. $\Omega \gg \Omega_0$ indicates the recovered signal (f) is a poor fit to the measurement (g). On the other hand, $\Omega \ll \Omega_0$ indicates the recovered signal is an over fit and contains structures arising from the measurement error. The variance of a measured background spectrum $g_{0i} = c + e_i$, where c is the constant background level and e_i is the noise, may be taken as the expected variance Ω_0.

$$\Omega_0 = \frac{1}{N} \sum_{i=1}^{N} e_i^2. \tag{6.12}$$

6.3.3 Numerical test

The maximum entropy deconvolution scheme was applied to a set of synthetic spectra with noise broadened by a given instrumental function to test its reliability. It was seen that the deconvolution scheme is robust against measurement noise. Figure 6.5a shows that the deconvolution completely recovers the double peaks in the original spectrum from the noisy data broadened by the instrumental function. In practice, the instrumental function is measured by taking a reference spectrum and so contains measurement errors. The deconvolution scheme was also tested against uncertainty

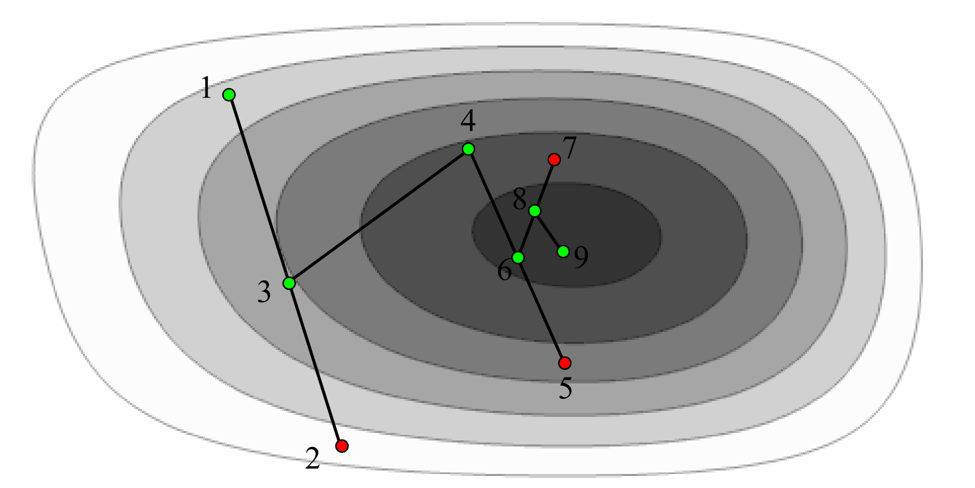

Figure 6.4: Example of the steepest decent iterations. Green dot indicates a successful step toward the minimum and red dot indicates too large a step size. The given example is a somewhat worst-case scenario where the initial step size is too large.

in the instrumental function. No noticeable change in the recovered spectrum was observed until the signal-to-noise ratio of the instrumental function was degraded below $\sim$20 (figure 6.5b). The signal-to-noise ratio of the measured instrument function for our spectroscopic system is very high ($\gtrsim 100$) and so the corresponding deconvolution error would be small.

The two-dimensional version of the maximum entropy deconvolution scheme has also been implemented to enhance the Imacon camera images (figure 6.6). In the thesis work of Romero-Talamás [48], a similar deconvolution scheme based on the work of Wilczek and Drapatz [49] was used to enhance the resolution of the blurred SSPX plasma images.

6.4 Theoretical fitting of Stark profile

The profiles of hydrogen lines emitted from hydrogen plasma of large density ($n_e \gtrsim 10^{22}$ m^{-3}) are significantly different from the Lorentzian function. The H_β line profile characterized by the central dip as shown in figure 4.7 is a good example. For such line profiles, it is not straightforward to define the profile width. The width may be defined as the FWHM of the Lorentzian function best fitting the profile or the FWHM

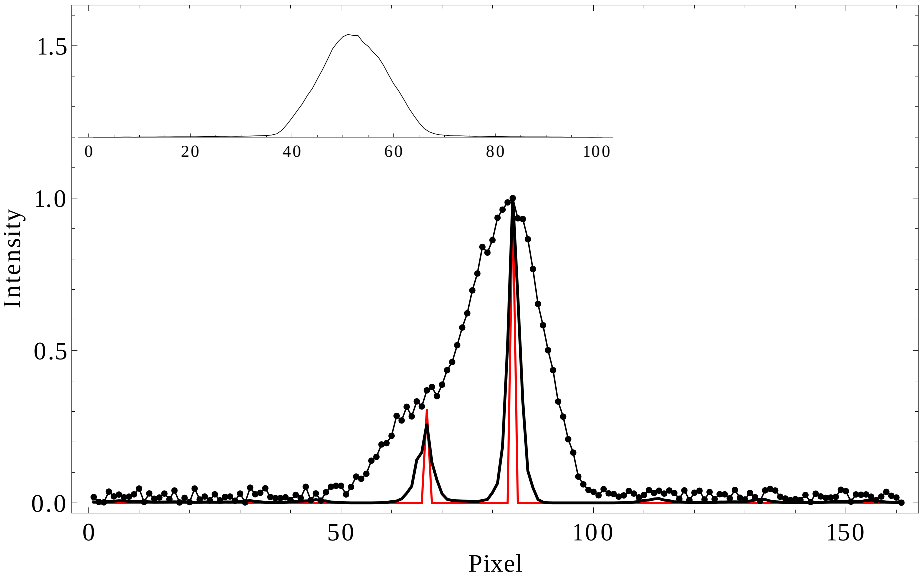

(a) Maximum entropy deconvolution of a synthetic spectrum

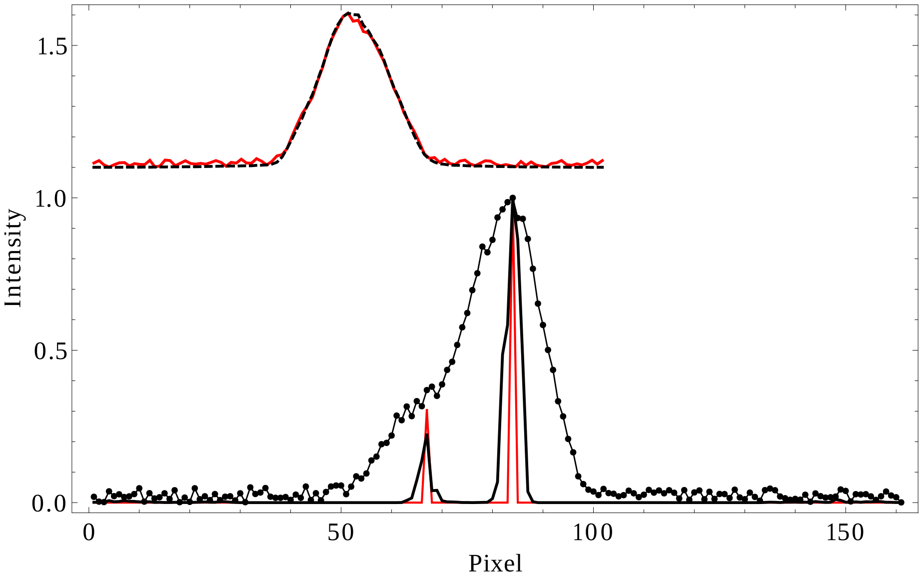

(b) with degraded instrumental function

Figure 6.5: (a) Maximum entropy deconvolution of a synthetic spectrum. The original synthetic spectrum (red line) contains two peaks that are merged together in the measured spectrum (connected dots) by the instrumental broadening. Random noise has been added to the measured spectrum so that the signal-to-noise ratio is 20 at the peak. Thick solid line represents the recovered spectrum by the maximum entropy deconvolution. (b) Maximum entropy deconvolution with degraded instrumental function (red solid line). The original instrument function (dashed line) is overlaid with the degraded one. The signal-to-noise ratio of the degraded instrumental function is 20 at the peak. No noticeable change except small details in the peaks is seen in the recovered spectrum.

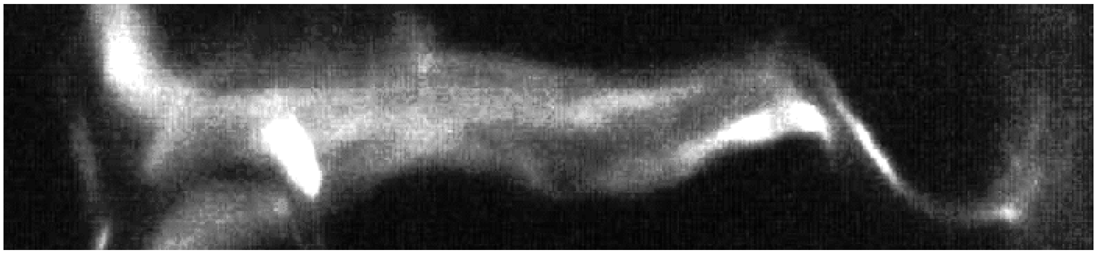

(a) Original Imacon image

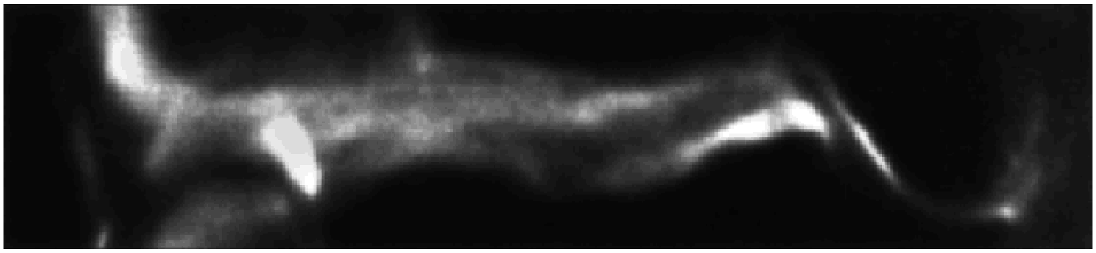

(b) Reconstructed image

Figure 6.6: Example of the image reconstruction by the maximum entropy deconvolution method.

of the raw profile. However, the validity of applying such definitions of profile width to equation (5.29) for density estimation needs to be checked.

Instead of introducing an arbitrary definition of profile width, the density of hydrogen plasma can be estimated by finding the best theoretical fit to observed line profiles. Stehlé and Hutcheon [24] calculated Stark broadened hydrogen line profiles for a pure hydrogen plasma and tabulated the result according to line species, density, and temperature. The Stark broadening tabulation spans a density range between 10^{16} and 10^{25} m^{-3} (20 densities) and a temperature range between 2500 and 1.3×10^6 K (10 temperatures). Local thermodynamic equilibrium is assumed in the calculation and so $T_i = T_e$.

The best theoretical fit to an observed line profile can be found as follows. A rough density estimate is made using the FWHM of the raw profile in equation (5.29). The plasma temperature is chosen between 1 and 10 eV (section 6.1.2). The choice of temperature is not critical for H_β line profiles because the Stark broadening of the H_β line is nearly independent of temperature (chapter 5). The computed line profile corresponding to the trial density and temperature is retrieved by a computer code supplied in the distribution of the Stark broadening tabulation. The computer code returns interpolated data if necessary. The retrieved profile is then convolved with the instrumental function to simulate the same intrumental broadening present in the observed line profile. The trial density is varied until the computed profile fits well to the observed profile. The temperature may be further adjusted to obtained a better fit.

The resulting best-fit density is compared to the density estimated by the simple method described in section 6.2, where the total width is taken from a Lorentzian fit to the observed profile. The difference between the two estimates of density is less than 10%, ensuring the validity of the simple density estimation method.

Chapter 7

Summary and conclusion

The Caltech spheromak plasma gun generates highly collimated rapidly evolving plasma structures. The planar configuration of the gun electrodes has permitted direct observation of the entire plasma dynamics and four distinct evolution stages have been identified in previous work by others. The four evolution stages are (1) eight well-collimated arched flux tubes reminiscent of spider legs form across the gun electrodes, (2) the spider leg flux tubes coalesce into a single central plasma jet, (3) the plasma jet expands axially and becomes collimated, and (4) the elongated plasma jet may undergo MHD instabilities. The present work has reported new experimental observations of the first and the third stages showing that the observed collimation is a result of the MHD pumping of plasma particles into flux tubes.

In chapter 3, the construction of a high-resolution spectroscopic system is described. The spectroscopic system has 12 channels with flexible lines of sight and can measure emission spectra radiated from multiple locations of the plasma simultaneously. Jet velocities are measured from Doppler shifts of spectral lines and electron densities are measured from Stark broadened spectral lines. The Stark broadening mechanism is summarized in chapter 5. A simple method to extract densities from Stark broadened lines is described in chapter 6. The method provides reliable plasma density diagnostics for densities $\gtrsim 10^{21}$ m^{-3}.

In chapter 4, the experimental results are presented, showing in detail that the observed densities and velocities are consistent with the MHD pumping model. The measured jet velocities (∼40 km/sec) are the Alfvénic velocity corresponding to the measured density ($\sim 10^{22}$ m^{-3}) and azimuthal magnetic field strength ($\sim$1 T) as predicted by the MHD pumping model. It is demonstrated that the flow slowing down observed at the forefront of the jet leads to the observed mass accumulation and subsequent jet collimation according to the MHD pumping model. In addition, it is clearly shown that the measured density amplification (from $\sim 10^{17}$ up to $\sim 10^{22}$ m^{-3}) is entirely due to the MHD pumping and cannot be accounted by the gas puffing.

We conclude that the MHD pumping and collimation model has provided a consistent explanation for the observed collimation and density amplification of the gun-produced plasmas. Thus, the MHD pumping model provides valuable insight into the ubiquitous collimation of laboratory, solar, and astrophysical plasmas.

Appendix A

Leak analysis

A.1 Equilibrium pressure; pumping, leak, and wall desorption

The change in number of particles in the vacuum chamber with volume V is

$$\Delta N = V\Delta n = -nR_p\Delta t + n_A R_l \Delta t, \tag{A.1}$$

where n is the number density of air inside the chamber, n_A is the number density of the air outside the chamber, R_p is the pumping rate (volume per unit time), and R_l is the effective leak (including wall desorption) rate.

$$V\frac{dn}{dt} = -nR_p + n_A R_l \tag{A.2}$$

$$V\frac{dp}{dt} = -pR_p + p_A R_l \quad \text{(expressed in terms of pressures)} \tag{A.3}$$

$$\Longrightarrow p = (p_0 - p_A R_l/R_p)\exp(-tR_p/V) + p_A R_l/R_p. \tag{A.4}$$

Thus, the pressure (p) inside the chamber exponentially approaches the equilibrium pressure p_e given by

$$p_e = p_A R_l/R_p. \tag{A.5}$$

If there is no pumping,

$$\left(\frac{dp}{dt}\right)_{\text{no pump}} = p_A R_l / V \text{ ; linear pressure rise} \tag{A.6}$$

$$\Longrightarrow R_l = \left(\frac{dp}{dt}\right)_{\text{no pump}} V/P_A \tag{A.7}$$

$$R_p = R_l p_A / p_e = \left(\frac{dp}{dt}\right)_{\text{no pump}} V/P_e. \tag{A.8}$$

Hence, both the effective leak R_l and the pumping speed R_p can be estimated from the linear pressure rise $\left(\frac{dp}{dt}\right)_{\text{no pump}}$ by shutting off pumping for a moment.

A.2 Example

When the gate valve of the cryopump was closed, the chamber pressure increased from 1.4×10^{-7} torr to 9.3×10^{-6} torr in two minutes.

$$\left(\frac{dp}{dt}\right)_{\text{no pump}} = (9.3 \times 10^{-6} - 1.4 \times 10^{-7})/120 = 7.6 \times 10^{-8} \text{ torr/sec.}$$

Since $p_A = 760$ torr, $p_e = 1.4 \times 10^{-7}$ torr, and $V = 2.4$ m^3,

$$R_l = \left(\frac{dp}{dt}\right)_{\text{no pump}} V/P_A = 2.4 \times 10^{-10} \text{ m}^3\text{/sec} = 2.4 \times 10^{-4} \text{ cc/sec,}$$

$$R_p = \left(\frac{dp}{dt}\right)_{\text{no pump}} V/P_e = 1.3 \text{ m}^3\text{/sec} = 1300 \text{ liters/sec.}$$

The cryopump is working more or less with the specified pumping speed ~1000 liters/sec. The effective leak (~10^{-4} cc/sec) is reasonable considering tens of O-rings (~10^{-6} cc/sec per O-ring) installed on the chamber and desorption from the wall.

In the event of a leak much greater than the normal effective leak (~10^{-4} cc/sec), determining the size of leak aperature may help locate the leak.

$$R_l \approx v_{\text{th}} \times D_{\text{leak}}^2, \tag{A.9}$$

where $v_{\text{th}} = 340$ m/sec is the sound speed of air and D_{leak} is the leak aperature diameter. For example, consider the case when the equilibrium chamber pressure is as high as 1.0×10^{-5} due to an unknown leak. The leak rate is

$$R_l = R_p p_e / p_A = 1300 \cdot \left(1.0 \times 10^{-5}/760\right) \text{ liters/sec} \approx 0.017 \text{ cc/sec},$$

and the corresponding leak aperature size is

$$D_{\text{leak}} = \sqrt{1.7 \times 10^{-8}/340} \text{ m} \approx 7 \ \mu\text{m}.$$

Appendix B

Measurement of gas cloud profile

B.1 Fast ionization gauge (FIG)

A home-built fast ionization gauge (FIG) has been constructed by P. M. Bellan to measure the output of the fast gas valves [21]. The FIG measurement detail is reproduced here for completeness by the kind courtesy of S. You and a modified gas cloud model based on his original model is presented.

The FIG is mounted on a right-angle arm as shown in figure 2.2 so that both its axial and radial locations can be adjusted. The FIG is operated in the same way as standard hot-cathode ionization gauges. Thermionic electrons emitted from a heated filament (cathode; negatively biased) are accelerated toward a positively biased electrode (anode). The electrons collide with gas molecules in the background and ionize them. The distance between the cathode and the anode is designed to be smaller than the electron's ionization mean free path to prevent multiple ionizing collisions. The ionized atoms are attracted to a grounded electrode called collector. The total number of ionizing collisions per unit time is

$$\dot{N}_i = n\sigma_{i,g} l \dot{N}_e = (P/kT)\sigma_{i,g} l \dot{N}_e, \tag{B.1}$$

where n is the gas number density, $\sigma_{i,g}$ is the ionization cross-section for gas "g", l is the distance between the cathode and anode, $\dot{N}_e$ is the number of emitted electrons per unit time. In terms of the collector current $I_c = \dot{N}_i e$ and the emission current

$I_e = \dot{N}_e e$,

$$I_c = PS_g I_e \Longrightarrow P = I_c/(S_g I_e) = I_c/(R_g S_{N2} I_e), \tag{B.2}$$

where $S_g = \sigma_{i,g} l/kT$ is called as gauge sensitivity factor [torr^{-1}]. Relative gauge sensitivity factors (R_g) commonly calibrated for nitrogen are available from the public vacuum literature [50]. The FIG's sensitivity factors are obtained by comparing with a standard Bayard-Alpert type gauge. However, the pressure calculated by equation (B.2) has only a relative meaning since the pressure near the gas orifices is presumably of the order of mtorr and S_g becomes nonlinear for pressure > 1 mtorr.

FIG measurements are shown in figure B.1. Figure B.1b shows that the particle flux from the fast gas valve lasts for ~5 msec, much longer than our plasma lifetime of ~20 μsec.

B.2 Gas profile modeling

Consider the gas density profile $f_i(r, z)$ produced by the orifice i ($i = 1, 2, \ldots, 16$ is the index number of each orifice). The radial velocity distribution is presumably Gaussian at the orifice since gas particles will be thermalized in radial direction as they flow along the long gas line. The particle source at the orifice can be considered point-like at distance ($\sqrt{r^2 + z^2}$) much greater than the orifice diameter. In this limit, the Gaussian radial velocity distribution produces a Gaussian radial density profile because

$$\begin{aligned} f_i \Delta r &\propto \int_{r/t}^{(r+\Delta r)/t} \exp(-v^2/v_T^2) dv \\ &\propto \exp(-v^2/v_T^2)\Delta r/t \\ &\propto \exp(-r^2/(tv_T)^2)\Delta r/t \quad (^* v = r/t), \end{aligned} \tag{B.3}$$

where $f_i \Delta r$ is the number of particles in the ring $(r, r + \Delta r)$ at time t and v_T is the radial thermal velocity of the gas.

The density drops quadratically in the axial direction assuming the axial expansion velocity is constant (an exponential drop was assumed in the original model of S. You). Hence, the gas blooms out radially at the speed of sound (v_T) and expands axially at some Mach number, forming a cylindrical cone of gas cloud. The width of the radial profile gives the Mach number since the Mach number (M) is essentially the ratio of the axial velocity (v_z) to the sonic radial velocity (v_T):

$$r_{\mathrm{HM}} = tv_T\sqrt{\log 2} = tv_z(v_T/v_z)\sqrt{\log 2} = \frac{z}{M}\sqrt{\log 2}, \tag{B.4}$$

$$M = \frac{z}{r_{\mathrm{HM}}}\sqrt{\log 2} = \tan\alpha\sqrt{\log 2}, \tag{B.5}$$

where r_{HM} is the radius of half maximum density at a given axial position z and α is half the cone angle measured at half maximum density. The density profile can be written in terms of Mach number M

$$f_i(r,z) = f_{0i}\frac{1}{z^2}\exp\left(-\frac{r^2}{(tv_z/M)^2}\right) = f_{0i}\frac{1}{z^2}\exp\left(-\frac{r^2}{(z/M)^2}\right). \tag{B.6}$$

The total particle density f_T at a point (r,ϕ,z) is the sum of the 16 gas clouds

$$f_T(r,\phi,z) = \sum_{i=1}^{16} f_i(r_i,z), \tag{B.7}$$

where r_i is the radial distance from the orifice i.

The FIG measurements fit well with the gas cloud model calculated by equation (B.7) as shown in figure B.1.

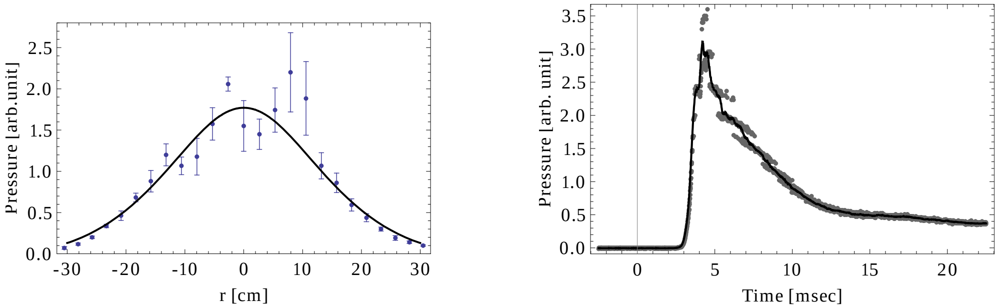

(a) Radial pressure profile

(b) Pressure trace

Figure B.1: Fast ion gauge (FIG) pressure measurement (data courtesy of S. You). Nitrogen was injected by the four fast gas valves. The FIG's axial location was $z = 18$ cm. (a) Radial pressure profile. The data points are taken at 7 msec (after the fast gas valves triggered) and the error bars indicate signal variations in ± 0.5 msec. The solid curve is the calculated profile according to equation (B.7). The shape of the radial profile becomes stationary after about 5 msec and starts to fit with calculated profiles. (b) Pressure trace at $r = 0$ cm. The pressure peaks at about 4 msec. The gas flow speed is $(L + 0.18\text{m})/4\text{msec} = 300$ m/sec $\approx$ the sound speed of nitrogen, where $L \approx 1$ m is the length of gas lines (distance from fast gas valves to orifices).

Appendix C

Linear dispersion of Czerny-Turner spectrometer

A Czerny-Turner spectrometer is shown schematically in figure C.1. Knowledge of the linear dispersion of the spectrometer at the exit plane is desired to calibrate a spectral window for which no reference spectral lamps are available and also to circumvent repetitive use of spectral lamps for each spectral window. The grating equation is

$$d\,(\sin\alpha + \sin\beta) = m\lambda, \tag{C.1}$$

where α is the angle of incidence, β is the angle of diffraction, d is the groove spacing, m is the diffraction order, and λ is the wavelength of light. The sign of an angle is positive (negative) if drawn counterclockwise (clockwise) in figure C.1. Consider the angular dispersion, i.e., variation of λ as a function of β for a fixed α. The angular dispersion at the focusing mirror ($M2$) can be obtained by differentiating equation (C.1) with respect to β:

$$d\cos\beta = m\frac{\partial\lambda}{\partial\beta} \quad\Longrightarrow\quad \frac{\partial\lambda}{\partial\beta} = \frac{d\cos\beta}{m}. \tag{C.2}$$

Thus, the linear dispersion at the exit focal plane is

$$\frac{\partial\lambda}{\partial x} = \frac{1}{L}\frac{\partial\lambda}{\partial\beta} = \frac{d\cos\beta}{Lm}, \tag{C.3}$$

where L is the focal length of the focusing mirror.

A rotation of the grating by an angle θ determines the incidence/diffraction angles and selects a wavelength λ, which will be focused at the center of the exit focal plane. The selected wavelength λ is related to θ according to the grating equation (C.1):

$$\alpha = \alpha_0 + \theta, \tag{C.4}$$

$$\beta = -\alpha_0 + \theta, \tag{C.5}$$

$$\begin{aligned} d\left(\sin(\alpha_0+\theta) + \sin(-\alpha_0+\theta)\right) = 2d\sin\theta\cos\alpha_0 &= m\lambda \\ \implies \quad \sin\theta &= \frac{m\lambda}{2d\cos\alpha_0}. \end{aligned} \tag{C.6}$$

The linear dispersion at the selected wavelength λ can be expressed as a function of λ by inserting equations (C.4)–(C.6) into equation (C.3):

$$\begin{aligned} \frac{\partial\lambda}{\partial x} &= \frac{d}{Lm}\cos\beta = \frac{d}{Lm}\cos(-\alpha_0+\theta) = \frac{d}{Lm}\left(\cos\alpha_0\cos\theta + \sin\alpha_0\sin\theta\right) \\ &= \frac{d}{Lm}\left(\cos\alpha_0\frac{\sqrt{(2d\cos\alpha_0)^2-(m\lambda)^2}}{2d\cos\alpha_0} + \sin\alpha_0\frac{m\lambda}{2d\cos\alpha_0}\right) \\ &= \frac{1}{2L}\left(\sqrt{\left(\frac{2d\cos\alpha_0}{m}\right)^2 - \lambda^2} + \lambda\tan\alpha_0)\right) \end{aligned} \tag{C.7}$$

The pixel resolution $R(\lambda)$ of a CCD detector placed at the exit focal plane is $R(\lambda) = \Delta x\,\partial\lambda/\partial x$, where Δx is the detector pixel size.

The linear dispersion will be nearly constant across the detector plane (i.e., the exit focal plane) if the detector size is small compared to the focal length of the spectrometer since the bandpass of the detector $\sim$ (detector size)$\times(\partial\lambda/\partial x) \propto$ (detector size)$/L$. Consider a wavelength $\lambda' = \lambda + \Delta\lambda$ close to the selected wavelength λ. The wavelength λ' will have a different diffraction angle $\beta' = \beta + \delta$ than β and subsequently be focused at a point off the center of the exit focal plane. Because $\partial\lambda/\partial x \propto \cos\beta$ (equation (C.3)), the relative error $\Delta R/R$ of approximating $(\partial\lambda/\partial x)_{\lambda=\lambda'}$ by expression (C.7) is

$$\frac{\Delta R}{R} = \frac{\cos\beta' - \cos\beta}{\cos\beta} \approx \frac{-\delta\sin\beta}{\cos\beta} = -\delta\tan\beta. \tag{C.8}$$

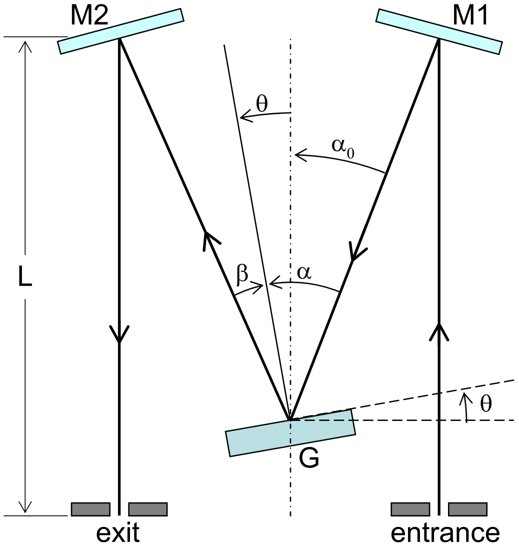

Figure C.1: Czerny-Turner configuration. G is the grating with groove spacing d. $M1$ is the collimating mirror and $M2$ is the focusing mirror with focal length L. α is the angle of incidence, β is the angle of diffraction, α_0 is half the angle between the incident and the diffracted light, and θ is the rotation angle of the grating.

The $\Delta\lambda$ is related to δ as

$$\begin{aligned} &\sin\beta' = \frac{m\lambda'}{d} - \sin\alpha = \sin(\beta+\delta) \approx \sin\beta + \delta\cos\beta \\ \Longrightarrow \quad &\delta \approx \left(\frac{m\lambda'}{d} - \sin\alpha - \sin\beta\right)/\cos\beta = \left(\frac{m\lambda'}{d} - \frac{m\lambda}{d}\right)/\cos\beta = \frac{m\Delta\lambda}{d\cos\beta}. \end{aligned}$$

Thus, the relative error is

$$\frac{\Delta R}{R} = \frac{m\Delta\lambda}{d}\tan\beta/\cos\beta \lesssim \mathcal{O}\left(\frac{\Delta\lambda}{d}\right). \tag{C.9}$$

For the spectroscopic system used in the present thesis work, $\Delta\lambda$ across the detector plane is ~2 nm and $d = 1/3600$ mm ≈ 280 nm. Thus, the relative variation of the linear dispersion across the detector plane is less than 1%.

Appendix D

Large vacuum viewport

Two large custom-made viewports (8″ diameter window welded on a 10” flange) and a commercial viewport (6″ view) installed on the east side of the vacuum chamber have been utilized for taking plasma pictures and spectra. More vacuum viewports with 8″ or greater view were desired for the cameras and the spectroscopic system to gain a better access to the plasma. An economic viewport design has been devised since commercial vacuum viewports are available only up to ∼6” view and a custom-made viewport with larger view size would be expensive prohibiting multiple installations of such viewports. The viewport design (figure D.1 consists of a modified 10″ Conflat flange, a viewport glass (Borofloat$^{\mathrm{TM}}$, 8.5″ diameter, 11 mm thick), an O-ring to form a vacuum seal (Viton, AS568A no. 172), and several clamps to hold the glass in place. The clamps are to give only an initial vacuum seal. Once the chamber starts being pumped out, the pressure difference will build up across the glass window, press the O-ring against the flange, and form a vacuum seal. Several viewports have been constructed according to the design and successfully installed on the chamber.

The window material and thickness of the home-built viewport were chosen to meet the optical transmission and mechanical strength required for the experiment as well as the budget. Borosilicate (Borofloat$^{\mathrm{TM}}$) was chosen as the window material for its excellent optical transmission (50% at 300 nm and 90% at 350–2000 nm) and resistance to thermal shock (due to a very low thermal expansion about one third of ordinary glass). For better UV transmission, the window can be replaced with more expensive fused silica or quartz window (80% at 180 nm and 90% at 300–2000 nm).

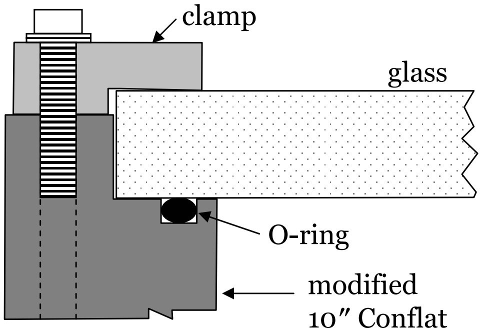

Figure D.1: Coss-sectional view of the large viewport (8″ view diameter). An 8.5″ diameter 11 mm thick borosilicate glass is installed on a modified 10″ Conflat flange. The O-ring forms a vacuum seal as the glass is pressed against the flange by the atmosphere.

The window needs to be thick enough to support the stress created by a large pressure difference across the window. A circular window under a uniform loading (pressure) W experiences the maximum stress σ at the center given by [51, p.175]:

$$\sigma = \frac{3(3+\nu)}{8} W r_0^2/t^2 \approx W r_0^2/t^2, \tag{D.1}$$

where r_0 and t are the radius and thickness of the window, respectively, and $\nu \sim 0.2$ is the Poisson's ratio of borosilicate ($\nu \sim 0.2$–0.4 for most materials). The maximum tensile strength (critical stress) of borosilicate is ∼25 MPa, so the minimum thickness of the window should be

$$\begin{aligned} \sigma &\approx W r_0^2/t^2 < 25 \text{ MPa} \\ \Longrightarrow \quad t &> r_0\sqrt{0.1/25} \approx 6 \text{ mm}, \end{aligned} \tag{D.2}$$

where the atmospheric pressure $W \sim 100$ kPa $= 0.1$ MPa and $r_0 = 4'' \approx 100$ mm. This minimum thickness is consistent with an empirical practice for determining load resistance of glass in buildings (ASTM Standard E 1300-04) [52]. The standard lists the critical load under which the glass of a given size and thickness will fail. For example, the critical loads are 7.2 and 2.2 kPa for annealed monolithic glasses of dimensions 30″ × 40″ × 8 mm and 60″ × 96″ × 10 mm, respectively. Since the critical thickness $t \propto \sqrt{W \times (\text{window area})}$ for a given maximum tensile strength, the minimum thickness for the 8″ borofloat window can be extrapolated as

$$\begin{aligned} t &> t_* \sqrt{\frac{W \times \pi r_0^2}{W_* \times (\text{window area})_*}} \\ &\approx \left\{ \begin{array}{c} 8 \times \sqrt{\frac{100 \times \pi 4^2}{7.2 \cdot (30 \times 40)}} \\ 10 \times \sqrt{\frac{100 \times \pi 4^2}{2.2 \cdot (60 \times 96)}} \end{array} \right. \approx 6 \text{ mm}, \end{aligned} \tag{D.3}$$

where the subscript $*$ denotes the values listed in the ASTM standard. The thickness of the borofloat window is chosen to be 11 mm for a good margin of safety.

Appendix E

Selection rules and commutation relations

E.1 Particle in a perturbed central potential

Consider a particle in a central potential $V(r)$. The Hamiltonian of the system is $H_0 = p^2/2m+V(r)$, where p, m are the momentum and mass of the particle. The eigenstate of the system is characterized by the principal quantum number n, azimuthal quantum number l, and magnetic quantum number m, and is commonly denoted as $|n,l,m\rangle$. The quantum number l and m are related to the angular momentum operators as

$$L_z|n,l,m\rangle = m\hbar|n,l,m\rangle, \tag{E.1}$$

$$L^2|n,l,m\rangle = (L_x^2+L_y^2+L_z^2)|n,l,m\rangle = l(l+1)\hbar^2|n,l,m\rangle. \tag{E.2}$$

The angular momentum operator L_i $(i = x, y, z)$ is defined as

$$\begin{aligned} L_i &= \epsilon_{ijk}R_jP_k \;\; \text{or} \\ \mathbf{L} &= \mathbf{R}\times\mathbf{P}, \end{aligned} \tag{E.3}$$

where $R_j(R_{x,y,z} \equiv X, Y, Z)$ is the position operator and P_j is the momentum operator.

Suppose a perturbing potential $H_1 = Fz$ (F: constant) is introduced to the original system H_0. The eigenstates $|n,l,m\rangle$'s mutually orthogonal in the original system may become coupled with each other by the perturbation, i.e., $\langle n,l,m|(H_0 +$

$H_1)|n', l', m'\rangle = \langle n, l, m|FZ|n', l', m'\rangle$ may become non-zero for $(n, l, m) \neq (n', l', m')$. The existence of a coupling between a pair of eigenstates can be determined by simply comparing the quantum numbers (n, l, m) and (n', l', m') instead of evaluating $\langle n, l, m|Z|n', l', m'\rangle$. Such rules called as selection rules can be found by considering commutation relations between the position operators and the angular momentum operators. The basic commutation relations among **R**, **P**, and **L** operators are

$$
\begin{aligned}
[P_i, R_j] &= -i\hbar\delta_{ij}, && \text{(E.4)}\\
[L_i, R_j] &= [\epsilon_{ikl}R_kP_l, R_j] = \epsilon_{ikl}R_k[P_l, R_j] = -i\hbar\epsilon_{ikl}R_k\delta_{lj} \\
&= i\hbar\epsilon_{ijk}R_k, && \text{(E.5)}\\
[L_i, L_j] &= i\hbar\epsilon_{ijk}L_k, && \text{(E.6)}\\
[L^2, L_i] &= 0, && \text{(E.7)}\\
\mathbf{L}\cdot\mathbf{R} &= L_iR_i = \epsilon_{ijk}R_jP_kR_i = \epsilon_{ijk}R_j([P_k, R_i] + R_iP_k) \\
&= \epsilon_{ijk}R_j(-i\hbar\delta_{ki} + R_iP_k) = \epsilon_{ijk}R_jR_iP_k = 0. && \text{(E.8)}
\end{aligned}
$$

The following selection rules are derived using these commutation relations in the following sections.

$\langle n, l, m|Z|n', l', m'\rangle \neq 0$ only if (1) $m = m'$ and (2) $l = l' = 0$ or $l = l' \pm 1$.

E.2 Selection rule for the quantum number m

The selection rule for the magnetic quantum number m is easily derived from the commutation relation (equation (E.5)), $[L_z, Z] = 0$.

$$\langle n, l, m|[L_z, Z]|n', l', m'\rangle = (m - m')\hbar\langle n, l, m|Z|n', l', m'\rangle = 0. \tag{E.9}$$

Thus, $\langle n, l, m|Z|n', l', m'\rangle = 0$ unless $m' = m$.

E.3 Selection rule for the quantum number l

The selection rule for the angular quantum number l can be found by considering the commutation relation between $\mathbf{R}$ and L^2 operators.

$$[L^2, R_i] = [L_jL_j, R_i] = L_j[L_j, R_i] + [L_j, R_i]L_j = i\hbar\epsilon_{jik}(L_jR_k + R_kL_j) \tag{E.10}$$

$$[L^2, \mathbf{R}] = -i\hbar(\mathbf{L}\times\mathbf{R} - \mathbf{R}\times\mathbf{L}) \qquad \text{(in vector form).} \tag{E.11}$$

Applying L^2 on the commutation relation above leads to

$$\begin{aligned}
[L^2, [L^2, \mathbf{R}]] &= -i\hbar[L^2, \mathbf{L}\times\mathbf{R} - \mathbf{R}\times\mathbf{L}] = -i\hbar(\mathbf{L}\times[L^2,\mathbf{R}] - [L^2,\mathbf{R}]\times\mathbf{L}) \\
&= -\hbar^2\left\{\mathbf{L}\times(\mathbf{L}\times\mathbf{R} - \mathbf{R}\times\mathbf{L}) - (\mathbf{L}\times\mathbf{R} - \mathbf{R}\times\mathbf{L})\times\mathbf{L}\right\} \\
&= -\hbar^2\left\{\mathbf{L}\times(\mathbf{L}\times\mathbf{R}) + (\mathbf{R}\times\mathbf{L})\times\mathbf{L} - \mathbf{L}\times(\mathbf{R}\times\mathbf{L}) - (\mathbf{L}\times\mathbf{R})\times\mathbf{L}\right\} \\
&= -\hbar^2\left\{\mathbf{L}(\mathbf{L}\cdot\mathbf{R}) - (\mathbf{L}\cdot\mathbf{L})\mathbf{R} + (\mathbf{R}\cdot\mathbf{L})\mathbf{L} - \mathbf{R}(\mathbf{L}\cdot\mathbf{L})\right\} \\
&\quad + \hbar^2\left\{\mathbf{L}\times(\mathbf{R}\times\mathbf{L}) + (\mathbf{L}\times\mathbf{R})\times\mathbf{L}\right\} \\
&= \hbar^2\left\{L^2\mathbf{R} + \mathbf{R}L^2 + \mathbf{L}\times(\mathbf{R}\times\mathbf{L}) + (\mathbf{L}\times\mathbf{R})\times\mathbf{L}\right\} \quad \text{(using (E.8)).}
\end{aligned}$$

The last two terms can be combined to give

$$\mathbf{L}\times(\mathbf{R}\times\mathbf{L}) + (\mathbf{L}\times\mathbf{R})\times\mathbf{L} = L^2\mathbf{R} + \mathbf{R}L^2 \tag{E.12}$$

$$\Longrightarrow [L^2, [L^2, \mathbf{R}]] = 2\hbar^2(L^2\mathbf{R} + \mathbf{R}L^2). \tag{E.13}$$

Equation (E.12) is derived as follows:

$$\mathbf{L}\times(\mathbf{R}\times\mathbf{L}) = L_i\mathbf{R}L_i + (\mathbf{L}\cdot\mathbf{R})\mathbf{L} = L_i\mathbf{R}L_i$$

$$(\mathbf{L}\times\mathbf{R})\times\mathbf{L} = L_i\mathbf{R}L_i + \mathbf{L}(\mathbf{R}\cdot\mathbf{L}) = L_i\mathbf{R}L_i$$

$$L_iR_jL_i = L_i([R_j, L_i] + L_iR_j]) = L_i(i\hbar\epsilon_{jik}R_k + L_iR_j) = L^2R_j + i\hbar\epsilon_{jik}L_iR_k$$

$$L_iR_jL_i = ([L_i, R_j] + R_jL_i])L_i = (i\hbar\epsilon_{ijk}R_k + R_jL_i)L_i = R_jL^2 + i\hbar\epsilon_{ijk}R_kL_i$$

$$\Longrightarrow 2L_iR_jL_i = L^2R_j + R_jL^2 + i\hbar(\epsilon_{jik}L_iR_k + \epsilon_{ijk}R_kL_i) = L^2R_j + R_jL^2, \tag{E.14}$$

where the term $(\epsilon_{jik}L_iR_k + \epsilon_{ijk}R_kL_i)$ vanishes because

$$\begin{aligned}
\epsilon_{jik}L_iR_k + \epsilon_{ijk}R_kL_i &= (\mathbf{L}\times\mathbf{R})_j + (\mathbf{R}\times\mathbf{L})_j \\
&= (\mathbf{L}\times\mathbf{R} + \mathbf{R}\times\mathbf{L})_j = ((\mathbf{R}\times\mathbf{P})\times\mathbf{R} + \mathbf{R}\times(\mathbf{R}\times\mathbf{P}))_j \\
&= (R_k\mathbf{P}R_k - \mathbf{R}(\mathbf{P}\cdot\mathbf{R}) + \mathbf{R}(\mathbf{R}\cdot\mathbf{P}) - (\mathbf{R}\cdot\mathbf{R})\mathbf{P})_j \\
&= R_kP_jR_k - R_jP_kR_k + R_jR_kP_k - R_kR_kP_j \\
&= R_k(P_jR_k - R_kP_j) - R_j(P_kR_k - R_kP_k) = R_k[P_j, R_k] - R_j[P_k, R_k] \\
&= -R_ki\hbar\delta_{jk} + R_ji\hbar = -R_ji\hbar + R_ji\hbar = 0.
\end{aligned}$$

The selection rule for l is obtained by applying $[L^2, [L^2, Z]]$ on the eigenstates:

$$\begin{aligned}
\langle n,l,m|[L^2,[L^2,Z]]|n',l',m'\rangle &= (l(l+1) - l'(l'+1))\hbar^2\langle n,l,m|[L^2,Z]|n',l',m'\rangle \\
&= (l(l+1) - l'(l'+1))^2\hbar^4\langle n,l,m|Z|n',l',m'\rangle. \qquad \text{(E.15)}
\end{aligned}$$

On the other hand, equation (E.13) yields an equivalent expression

$$\begin{aligned}
\langle n,l,m|[L^2,[L^2,Z]]|n',l',m'\rangle &= 2\hbar^2\langle n,l,m|L^2Z + ZL^2|n',l',m'\rangle \\
&= 2\hbar^4(l(l+1) + l'(l'+1))\langle n,l,m|Z|n',l',m'\rangle. \qquad \text{(E.16)}
\end{aligned}$$

Subtracting these two equivalent expressions leads to the selection rule for l:

$$\begin{aligned}
&\left\{(l(l+1) - l'(l'+1))^2 - 2(l(l+1) + l'(l'+1))\right\}\langle n,l,m|Z|n',l',m'\rangle = 0 \\
&\qquad (l+l'+2)(l+l')(l-l'+1)(l-l'-1)\langle n,l,m|Z|n',l',m'\rangle = 0. \qquad \text{(E.17)}
\end{aligned}$$

Therefore, $\langle n,l,m|Z|n',l',m'\rangle = 0$ unless $l = l' = 0$ or $l = l' \pm 1$.

Appendix F

Concavity of the maximum entropy potential function Z

The potential function Z defined in section 6.3 is strictly concave. The original proof is given by Alhassid et al. [46] and a succinct version of the proof consistent with the notations in the present manuscript is given here for completeness. Equations (6.7), (6.8), and (6.10) are rewritten in a form convenient for the proof,

$$f_k = w_k/Q, \tag{F.1}$$

$$Q = \sum_k w_k, \tag{F.2}$$

$$Z = \log Q + \sum_k \lambda_k g_k, \tag{F.3}$$

where $w_k = \exp\left(-\sum_{i=1}^{N} \lambda_i H_{ik}\right)$ and H is a square matrix (i.e., $M = N$).

The potential Z is strictly concave if and only if the Hessian matrix $\partial^2 Z/\partial\lambda_i\partial\lambda_j$ is positive definite. Consider the following equations to find an expression for the Hessian matrix:

$$\frac{\partial w_k}{\partial \lambda_i} = -H_{ik} w_k \tag{F.4}$$

$$\frac{\partial Q}{\partial \lambda_i} = -\sum_k H_{ik} w_k \tag{F.5}$$

$$\frac{\partial Z}{\partial \lambda_i} = \frac{1}{Q}\frac{\partial Q}{\partial \lambda_i} + g_i = -\sum_k H_{ik} f_k + g_i \tag{F.6}$$

$$\begin{aligned}\frac{\partial f_k}{\partial \lambda_j} &= \frac{-H_{jk} w_k}{Q} + w_k \frac{\sum_m H_{jm} w_m}{Q^2} = -H_{jk} f_k + f_k \sum_m H_{jm} f_m \\ &= -f_k \left(H_{jk} - \sum_m H_{jm} f_m \right) \end{aligned} \tag{F.7}$$

The Hessian matrix is obtained from the last two equations:

$$\frac{\partial^2 Z}{\partial \lambda_i \partial \lambda_j} = -\sum_k H_{ik} \frac{\partial f_k}{\partial \lambda_j} = \sum_k H_{ik} f_k \left(H_{jk} - \sum_m H_{jm} f_m \right). \tag{F.8}$$

The expression above can be simplified by defining $\hat{g}_j \equiv \sum_m H_{jm} f_m$ and $\hat{H}_{jk} \equiv H_{jk} - \hat{g}_j$:

$$\begin{aligned}\frac{\partial^2 Z}{\partial \lambda_i \partial \lambda_j} &= \sum_k H_{ik} f_k (H_{jk} - \hat{g}_j) \\ &= \sum_k (H_{ik} - \hat{g}_i) f_k (H_{jk} - \hat{g}_j) + \sum_k \hat{g}_i f_k (H_{jk} - \hat{g}_j) \\ &= \sum_k \hat{H}_{ik} f_k \hat{H}_{jk}, \end{aligned} \tag{F.9}$$

where $\sum_k \hat{g}_i f_k (H_{jk} - \hat{g}_j) = \hat{g}_i \left(\hat{g}_j - \sum_k f_k \hat{g}_j\right) = \hat{g}_i (\hat{g}_j - \hat{g}_j) = 0$ is used at the last step. Now, the positive definiteness of the Hessian matrix is easily seen as

$$\sum_{i,j} x_i \frac{\partial^2 Z}{\partial \lambda_i \partial \lambda_j} x_j = \sum_{i,j,k} (x_i \hat{H}_{ik}) f_k (x_j \hat{H}_{jk}) = \sum_k f_k \left[(\boldsymbol{x}^{\mathrm{T}} \hat{H})_k \right]^2 > 0 \tag{F.10}$$

for any vector $\boldsymbol{x} \neq \mathbf{0}$.

Bibliography

[1] P. M. Bellan. *Spheromaks*. Imperial College Press, 2000.

[2] H. Bruhns. Recent compact toroid research. *Plasma Phys. Control. Fusion*, 28:1389–1400, 1986.

[3] P. M. Bellan and J. F. Hansen. Laboratory simulations of solar prominence eruptions. *Phys. Plasmas*, 5(5):1991–2000, 1998.

[4] T. R. Jarboe. Review of spheromak research. *Plasma Phys. Control. Fusion*, 36:945–990, 1994.

[5] T. R. Jarboe. The spheromak confinement device. *Phys. Plasmas*, 12:058103, 2005.

[6] H. Alfvén, L. Lindberg, and P. Mitlid. Experiments with plasma rings. *J. Nucl. Energy, Part C*, 1:116–120, 1960.

[7] S. C. Hsu. Studies of magnetic helicity injection and dynamo fluctuations in a spheromak formed by a comparably sized planar coaxial gun. Proposal for the Fusion Energy Postdoctoral Research Program, 2000.

[8] S. C. Hsu and P. M. Bellan. A laboratory plasma experiment for studying magnetic dynamics of accretion disks and jets. *Mon. Not. Royal Astron. Soc.*, 334(2):257–261, 2002.

[9] S. C. Hsu and P. M. Bellan. Experimental identification of the kink instability as a poloidal flux amplification mechanism for coaxial gun spheromak formation. *Phys. Rev. Lett.*, 90(21):215002, 2003.

[10] P. M. Bellan. *Fundamentals of Plasma Physics.* Cambridge University Press, 2006.

[11] J. F. Hansen. *Laboratory simulations of solar prominences.* PhD thesis, California Institute of Technology, 2001.

[12] W. H. T. Vlemmings, P. J. Diamond, and H. Imai. A magnetically collimated jet from an evolved star. *Nature*, 440:58–60, 2006.

[13] P. M. Bellan. Why current-carrying magnetic flux tubes gobble up plasma and become thin as a result. *Phys. Plasmas*, 10(5):1999–2008, 2003.

[14] L. B. Loeb and J. M. Meek. *The Mechanism of the Electric Spark.* Stanford University Press, 1941.

[15] N. Bowler and Y. Huang. Electrical conductivity measurement of metal plates using broadband eddy-current and four-point methods. *Meas. Sci. Technol.*, 16(11):2913–2200, 2005.

[16] P. Clausing. The flow of highly rarefied gases through tubes of arbitrary length. *J. Vac. Sci. Technol.*, 8(5):636–646, 1971.

[17] P. M. Bellan. A simple system for locating ground loops. *Rev. Sci. Instrum.*, 78:065104, 2007.

[18] C. A. Romero-Talamás, P. M. Bellan, and S. C. Hsu. Multielement magnetic probe using commercial chip inductors. *Rev. Sci. Instrum.*, 75(8):2664–2667, 2004.

[19] J. Yee and P. M. Bellan. Taylor relaxation and λ decay of unbounded, freely expanding spheromaks. *Phys. Plasmas*, 7(9):3625–3640, 2000.

[20] C. Yang. Observations of spheromaks using an optical multichannel analyzer. Caltech Summer Undergraduate Research Fellowship, unpublished, 2000.

[21] S. You, G. S. Yun, and P. M. Bellan. Dynamic and stagnating plasma flow leading to magnetic-flux-tube collimation. *Phys. Rev. Lett.*, 95(4):045002, 2005.

[22] G. S. Yun, S. You, and P. M. Bellan. Large density amplification measured on jets ejected from a magnetized plasma gun. *Nuclear Fusion*, 47:181–188, 2007.

[23] W. L. Wiese. Line broadening. In R. H. Huddlestone and S. L. Leonard, editors, *Plasma Diagnostic Techniques*. Academic Press, 1965.

[24] C. Stehlé and R. Hutcheon. Extensive tabulations of Stark broadened hydrogen line profiles. *Astron. Astrophys. Suppl. Ser.*, 140:93–97, 1999.

[25] N. Konjević, A. Lesage, J. R. Fuhr, and W. L. Wiese. Experimental Stark widths and shifts for spectral lines of neutral and ionized atoms. *J. Phys. Chem. Ref. Data*, 31(3):819–927, 2002.

[26] D. Kumar and P. M. Bellan. Heterodyne interferometer with unequal path lengths. *Rev. Sci. Instrum.*, 77(8):083503, 2006.

[27] A. V. Voronin, V. K. Gusev, Yu. V. Petrov, N. V. Sakharov, K. B. Abramova, E.M. Sklyarova, and S. Yu. Tolstyakov. High kinetic energy plasma jet generation and its injection into the Globus-M spherical tokamak. *Nucl. Fusion*, 45(9):1039–1045, 2005.

[28] Y. Marandet, P. Genesio, M. Koubiti, L. Godbert-Mouret, B. Felts, R. Stamm, H. Capes, and R. Guirlet. Characterization of tokamak edge plasmas using spectroscopic line profiles. *Nucl. Fusion*, 44:118–122, 2004.

[29] B. L. Welch, H. R. Griem, J. Terry, C. Kurz, B. LaBombard, B. Lipschultz, E. Marmar, and G. McCracken. Density measurements in the edge, divertor and X-point regions of Alcator C-Mod from Balmer series emission. *Phys. Plasmas*, 2(11):4246–4251, 1995.

[30] H. Margenau and M. Lewis. Structure of spectral lines from plasmas. *Rev. Mod. Phys.*, 31(3):569–615, 1959.

[31] V. S. Lisitsa. Stark broadening of hydrogen lines in plasmas. *Sov. Phys. Usp.*, 20(7):603–630, 1977.

[32] J. M. Luque, M. D. Calzada, and M. Sáez. Experimental research into the influence of ion dynamics when measuring the electron density from the Stark broadening of the H_α, and H_β lines. *J. Phys. B: At. Mol. Opt. Phys.*, 36:1573–1584, 2003.

[33] S. Gasiorowicz. *Quantum Physics.* John Wiley & Sons, 2nd edition, 1996.

[34] S. Chandrasekhar. Stochastic problems in physics and astronomy. *Rev. Mod. Phys.*, 15(1):1–89, 1943.

[35] P. Kepple and H. R. Griem. Improved Stark profile calculations for the hydrogen lines H_α, H_β, H_γ, and H_δ. *Phys. Rev.*, 173(1):317–325, 1968.

[36] M. A. Gigosos and V. Cardeñoso. New plasma diagnosis tables of hydrogen Stark broadening including ion dynamics. *J. Phys. B: At. Mol. Opt. Phys.*, 29:4795–4838, 1996.

[37] C. Stehlé. Stark broadening of hydrogen Lyman and Balmer in the conditions of stellar envelopes. *Astron. Astrophys. Suppl. Ser.*, 104:509–527, 1994.

[38] S. Mar, J. A. Aparicio, M. I. de la Rosa, J. A. del Val, M. A. Gigosos, V. R. González, and C. Pérez. Measurement of Stark broadening and shift of visible N II lines. *J. Phys. B: At. Mol. Opt. Phys.*, 33:1169–1184, 2000.

[39] M. Mimura and K. Sato. Convolution-fitting method for Doppler-broadening plasma ion temperature measurement. *Jpn. J. Appl. Phys.*, 34:1668–1672, 1995.

[40] Y. Liu, J. Lin, G. Huang, Y. Guo, and C. Duan. Simple empirical analytical approximation to the Voigt profile. *J. Opt. Soc. Am. B*, 18(5):666–672, 2001.

[41] N. Agmon, Y. Alhassid, and R. D. Levine. An algorithm for finding the distribution of maximal entropy. *J. Comp. Phys.*, 30:250–258, 1979.

[42] S. K. P. Tripathi, P. M. Bellan, and G. S. Yun. Observation of kinetic plasma jets in a coronal-loop simulation experiment. *Phys. Rev. Lett.*, 98:135002, 2007.

[43] C. W. Groetsch. *Inverse Problems.* Mathematical Association of America, 1999.

[44] G. S. Yun. Analysis on stability, reliability and efficiency of maximum entropy deconvolution. Caltech Graduate Science Symposium, 2003.

[45] P. M. Bellan. private communication, 2003.

[46] Y. Alhassid, N. Agmon, and R. D. Levine. An upper bound for the entropy and its applications to the maximal entropy problem. *Chem. Phys. Lett*, 53:22–26, 1978.

[47] S. F. Gull and G. J. Daniell. Image reconstruction from incomplete and noisy data. *Nature*, 272(20):686–690, 1978.

[48] C. A. Romero-Talamás. *Investigations of spheromak plasma dynamics: high-speed imaging at the Sustained Spheromak Physics Experiment and magnetic diagnostics at the CalTech spheromak experiment.* PhD thesis, California Institute of Technology, 2005.

[49] R. Wilczek and S. Drapatz. A high accuracy algorithm for maximum entropy image restoration in the case of small data sets. *Astron. Astrophys.*, 142:9–12, 1985.

[50] R. Holanda. Sensitivity of hot-cathode ionization vacuum gages in several gases. Technical Report E-6759; NASA-TN-D-6815, NASA, 1972.

[51] D. W. A. Rees. *Mechanics of Solids and Structures.* Imperial College Press, 2000.

[52] J. E. Minor and H. S. Norville. Design of window glass for lateral pressures. *J. Archit. Eng.*, 12(3):116–121, 2006.